

# Conceptual design and simulation of robot-assisted manipulator for stereotactic neurosurgery in the MRI-guided process

by

Bocheng Xu

A Thesis submitted to the Faculty of Graduate Studies of

The University of Manitoba

in partial fulfilment of the requirements of the degree of

MASTER OF SCIENCE

Department of Mechanical Engineering

Faculty of Graduate Studies

University of Manitoba

Winnipeg, Manitoba

December 2020

Copyright © 2020 by Bocheng Xu

# Abstract

With the development of robotic technologies, robot-assisted systems have become one of the major directions for clinical surgical interventions. Stereotactic neurosurgery, which is one of subfields of surgery, is widely used in the neurological brain surgery because of its minimally invasive and precise positioning. A traditional procedure of the stereotactic neurosurgery mainly relies on preoperative images from the magnetic resonance imaging (MRI) scanner. However, during the neurosurgery, the brain tissue deformation and shift disrupt the spatial relation between the patient and preoperative image volumes, which causes localization errors. For solving the problem, a robotic-assisted manipulator in the MRI-guided process can be applied to minimize the issue of “tissue shift” during the neurosurgery. In this research, an MRI-guided neurosurgical robot is proposed based on the MRI technology to improve the efficiency and accuracy of the neurosurgery. Highlights of the research are as follows.

(1) Based on customer's requirements, a conceptual MRI guided robot-assisted manipulator is proposed for stereotactic neurosurgical precision positioning. Technical specifications such as motors, materials, dimensions, and degrees of freedom are determined based on benchmarking products.

(2) Kinematics modeling of the proposed MRI-guided robotic manipulator is established. Its trajectory in space is planned according to actual neurosurgical clinical procedures. MATLAB simulation verifies the accuracy of kinematic models and feasibility of trajectory planning.

(3) A simulation model is built to decide the workspace of the proposed MRI-guided robotic manipulator. The strong magnetic fields are set up in Maxwell. Stresses on the manipulator in the magnetic field and effects on the strength of the static magnetic field are analyzed. The results show that the proposed manipulator can meet the surgical requirements and is safe in the MRI environment because of its low impact on the strong magnetic field.

# Acknowledgments

I would first like to express my gratitude to my supervisor Dr. Qingjin Peng for his mentoring, guidance and support throughout the years of my Master study. Dr. Peng has been an incredible supervisor and is knowledgeable in all aspects of mechanical engineering field. Dr. Peng has provided me much academic guidance, professional assistance and experience.

I would also like to thank Dr. Gong Zhang, Dr. John Saunders, Dr. Haoqing Zhu and Dr. Gordon Klimenko for introducing me to the field of MRI and surgical robots. I wish to thank Dr. Ma Yu, director of Neurosurgery, Second Affiliated Hospital of Tsinghua University, China, for sharing valuable experience in neurosurgery. Under their guidance, I was able to engage in the research of the MRI-guided stereotactic neurosurgical robot.

I wish to acknowledge that this research has been supported by Cubresa Inc., SCHERI Inc., Matics and University of Manitoba. I appreciate it very much to Manjari Murthy and her colleagues from Cubresa Inc. for their support and help. I would also like to thank my colleagues in the Virtual Manufacturing Lab who helped me for my research: Rui Li, Yanlin Shi, Marwan Baloch, Hamid Fazeli, Rajiv Kumar Vashisht, Jing Guo, and Xiangwei Mou.

Finally, I am deeply thankful to my family and my wife, for their love, understanding, encouragement and support. I could never have come this far without their support. This work would not have been possible without the help and support of my family, advisor, colleagues and friends. I would like to expressly thank everyone who has helped me over the past years of my Master study.

# Contents

Abstract.....	I
Acknowledgments.....	II
Contents .....	III
List of Tables.....	VI
List of Figures .....	VII
Chapter 1 .....	1
1.1 Research background and motivation .....	1
1.2 Research objectives .....	6
1.3 Thesis contents and structure .....	6
Chapter 2.....	9
2.1. Surgical robots.....	9
2.2. Robotic techniques for the stereotactic neurosurgery .....	9
2.2.1. Conventional stereotactic neurosurgery.....	10
2.2.2. Robot-assisted systems for neurosurgery.....	11
2.3. MRI-Guided Neurosurgery .....	14
2.3.1. MRI scanner.....	15
2.3.2. MRI Terminology .....	16
2.3.3. MRI compatible materials.....	17
2.3.4. MRI compatible actuators and sensors .....	17
2.4. MRI-guided robotic systems for neurosurgery.....	19
2.5. Conceptual design methods in product development.....	20
2.5.1. Quality function deployment (QFD).....	20
2.5.2. House of quality (HoQ) .....	21
2.5.3. Integrating QFD and Benchmarking methods .....	23
2.6. Summary .....	24
Chapter 3.....	25
3.1. Introduction .....	25
3.2. Identifying of Customer Needs and Technical Metrics .....	25

3.2.1. Customer requirements .....	25
3.2.2. Technical metrics .....	27
3.3. Concept generation of the MRI-guided robot .....	28
3.3.1. Relationship matrix of CRs and TMs .....	28
3.3.2. Benchmarking competitors and design target of TMs .....	31
3.3.3. Scheme of the robot structure .....	34
3.3.4. Selections of actuators and materials .....	37
3.3.5. Result and comparison .....	40
3.4. Summary .....	41
Chapter 4 .....	42
4.1. Introduction .....	42
4.2. Robotic kinematics .....	42
4.2.1. Description of position .....	42
4.2.2. Description of pose .....	43
4.2.3. Denavit–Hartenberg (D–H) parameters .....	45
4.3. Detailed kinematic modeling of the MRI-guided robot .....	46
4.3.1. Forward kinematic modeling .....	48
4.3.2. Inverse kinematic modeling .....	50
4.3.3. Kinematics verification and results .....	53
4.4. Trajectory planning of MRI-guided robot .....	55
4.4.1. Trajectory planning for the stereotactic neurosurgery .....	56
4.4.2. Trajectory planning in the joint space .....	59
4.4.3. Trajectory planning in the task space .....	61
4.4.4. Simulation and results .....	62
4.5. Summary .....	65
Chapter 5 .....	66
5.1. Introduction .....	66
5.2. Workspace compatibility for the MRI-guided robot .....	67
5.2.1. MRI-guided robot workspace analysis .....	67

5.2.2. Workspace simulation and results.....	68
5.3. MRI compatibility .....	70
5.3.1. MRI compatibility analysis under the MRI environment .....	70
5.3.2. MRI compatibility simulation and results.....	74
5.4. Summary .....	82
Chapter 6.....	83
6.1. Research summary .....	83
6.2. Research contributions .....	84
6.3. Future work .....	85
References.....	86

# List of Tables

Table 2-1 Terminology for medical devices in the MR environment according to ASTM Classification.....	17
Table 2-2 Summary of the state-of-the-art MRI-guided robotic systems for neurosurgery .....	19
Table 2-3 Literature of QFD in the medical robot design.....	21
Table 3-1 Customer needs and importance rates of MRI-guided robot.....	26
Table 3-2 Technical Metics .....	27
Table 3-3 Relations between CRs and TMs.....	30
Table 3-4 Specifications of three robot manipulator benchmarks .....	32
Table 3-5 Rates of the three benchmarks .....	33
Table 3-6 Comparison of different driving schemes.....	37
Table 3-7 Comparison with benchmarking robots.....	40
Table 4-1 D-H Parameter of MRI-guided robot .....	48
Table 4-2 Constant values of D-H parameters .....	48
Table 4-3 Inverse solutions for robotic manipulator.....	55
Table 4-4 Comparison of planning based on different spatial trajectories .....	58
Table 4-5 Constraints for six parameters .....	60
Table 5-1 DH parameters of the MRI-guided robot.....	68
Table 5-2 List of chemical compositions for 304 stainless steel .....	75
Table 5-3 Physical properties of three different types of materials .....	75
Table 5-4 MR compatibility evaluation for the MRI-guided robot .....	82

# List of Figures

Figure 1–1 Conventional stereotactic neurosurgical workflow .....	2
Figure 1–2 Brain shift/deformation when the skull is opened [4] .....	3
Figure 1–3 Magnetic resonance imaging (MRI)- guided and robot-assisted stereotactic neurosurgery .....	5
Figure 1–4 Thesis outline.....	8
Figure 2–1 Traditional stereotactic frames: (a) Leksell® Frame; (b) STarFix Frame [11] .....	11
Figure 2–2 Three robotic systems proposed in [18]; (a) Robots will be operated automatically based on pre-determined/specified actions by surgeons; (b) Surgeons control and manipulate robots remotely and in real-time; (c) robotic end-effectors are manually controlled by surgeons. ....	12
Figure 2–3 Commercially available robotic systems for stereotactic neurosurgery; (a) da Vinci (Intuitive Surgical, CA, Sunnyvale); (b) NeuroMate (Integrated Surgical Systems, Inc., Davis, CA, USA); (c) PathFinder (Prosurge, Inc., Cupertino, CA, USA); (d) Rosa (Medtech, Castelnau Le Lez, France) .....	14
Figure 2–4 MRI scanner components and working principle [24] .....	15
Figure 2–5 Structure of HoQ .....	22
Figure 3–1 Relationships matrix of CRs and TMs .....	28
Figure 3–2 Three robotic manipulators.....	31
Figure 3–3 HoQ of the MRI-guided robot manipulator.....	34
Figure 3–4 Proposed MRI-guided robot manipulator.....	35
Figure 3–5 The placement of the robot manipulator in neurosurgical operations .....	36
Figure 3–6 Dimensions of the robot manipulator .....	36
Figure 3–7 Transmission mechanism: Encoder, motor, harmonic reducer.....	38
Figure 3–8 Connection Method with Shinsei Motor Flowchart .....	39
Figure 3–9 Concept of the MRI-guided robot .....	40
Figure 4–1 Spatial point coordinates .....	43
Figure 4–2 Coordinate vector transformations of poses .....	44



Figure 4–3 Denavit–Hartenberg kinematic parameters .....	45
Figure 4–4 3D model and dimensions of proposed MRI-guided robot manipulator.....	47
Figure 4–5 MRI-guided robotic manipulator coordinate system for each joint .....	47
Figure 4–6 3D model of the robot manipulator based on MATLAB.....	53
Figure 4–7 Workflow of the stereotactic neurosurgery for trajectory planning.....	56
Figure 4–8 Surgical path planning using 3D image software [69] .....	57
Figure 4–9 Defining the free area and restricted area.....	59
Figure 4–10 Trajectory path of the robot manipulator.....	63
Figure 4–11 Trajectory simulation of displacement, velocity, and acceleration of each joint in joint space .....	63
Figure 4–12 Trajectory simulation of displacement, velocity, and acceleration of each joint in task space .....	64
Figure 4–13 Results of trajectory simulation for end effector in task space.....	64
Figure 5–1 3D model of the MRI-guided robot placement during operations .....	67
Figure 5–2 Workspace simulation of the 6-DOF MRI-guided robot; (a) 3D reachable workspace; (b) XY plane reachable workspace; (c) YZ plane reachable workspace; (d) XZ plane reachable workspace .....	70
Figure 5–3 MR images in three orthogonal planes (sagittal, coronal, and axial) in a 1.5 Tesla scanner without the metal implant (first column) and with the metal implant (second column) for spin-echo [73].....	72
Figure 5–4 Magnetic field distribution in the MRI environment .....	74
Figure 5–5 Brief structure of the MRI-guided robot .....	75
Figure 5–6 Magnetic field boundary in software.....	76
Figure 5–7 Magnetic field force calculation.....	76
Figure 5–8 The magnetic force from Maxwell to Static Structural analysis .....	77
Figure 5–9 Mesh of MRI robot in ANSYS Workbench.....	78
Figure 5–10 MR image artifacts evaluation in 1.5T MRI environment .....	79
Figure 5–11 MR image artifacts evaluation in 3.0T MRI environment .....	79
Figure 5–12 Strain of the MRI-guided robot in 1.5T magnetic force.....	80

Figure 5–13 Stress of the MRI-guided robot in 1.5T magnetic force.....	80
Figure 5–14 Strain of the MRI-guided robot in 3.0T magnetic force.....	81
Figure 5–15 Stress of the MRI-guided robot in 3.0T magnetic force.....	81

# List of abbreviations

3D	3 Dimension
AD	Axiomatic Design
AHP	Analytic Hierarchy Process
ASTM	American Society for Testing and Materials
CRs	Customer requirements
CT	Computed tomography
DBS	Deep Brain Stimulation
D–H	Denavit–Hartenberg
DOF	Degree of Freedom
FDA	Food and Drug Administration
HFD	Head Fixed Device
HOQ	House of Quality
IGIs	Image-guided Interventions
MRI	Magnetic Resonance Imaging
OR	Operating Room
PEEK	Polyetheretherketone
POM	Polyoxymethylene
QFD	Quality Function Deployment
RF	Radiofrequency
SS	Stainless Steel
TMs	Technical Metrics
TRIZ	Teoriya Resheniya Izobreatatelskikh Zadatch
VOC	Voice of Customer

# Chapter 1. Introduction

## 1.1 Research background and motivation

Stereotactic neurosurgery is a technique for the precise minimally invasive localization of inaccessible targets within the human cerebrum using a three-dimensional (3D) coordinate system to guide the insertion of surgical tools, such as cannula, electrode or probe, into patients' brain [1]. Currently, this clinical procedure has been widely applied in various clinical procedures, such as brain tissue biopsy, drug injection, brain tumor ablation, and Deep Brain Stimulation (DBS) [2]. The conventional process of the stereotactic neurosurgery comprises three main phases: 1) preoperative imaging and surgical planning based on medical imaging techniques, such as X-Ray, Computed tomography (CT), and Magnetic Resonance Imaging (MRI); 2) the intraoperative intervention via a stereotactic frame, which involves in the 3D coordinate alignment between the image and stereotactic frame using the manual insertion of surgical tools (needles/catheters); and 3) the postoperative evaluation through image-based scans [3]. The specific workflow in the conventional stereotactic neurosurgery is shown in Figure 1-1.

**Conventional Stereotactic Neurosurgery (5-6 hours)**

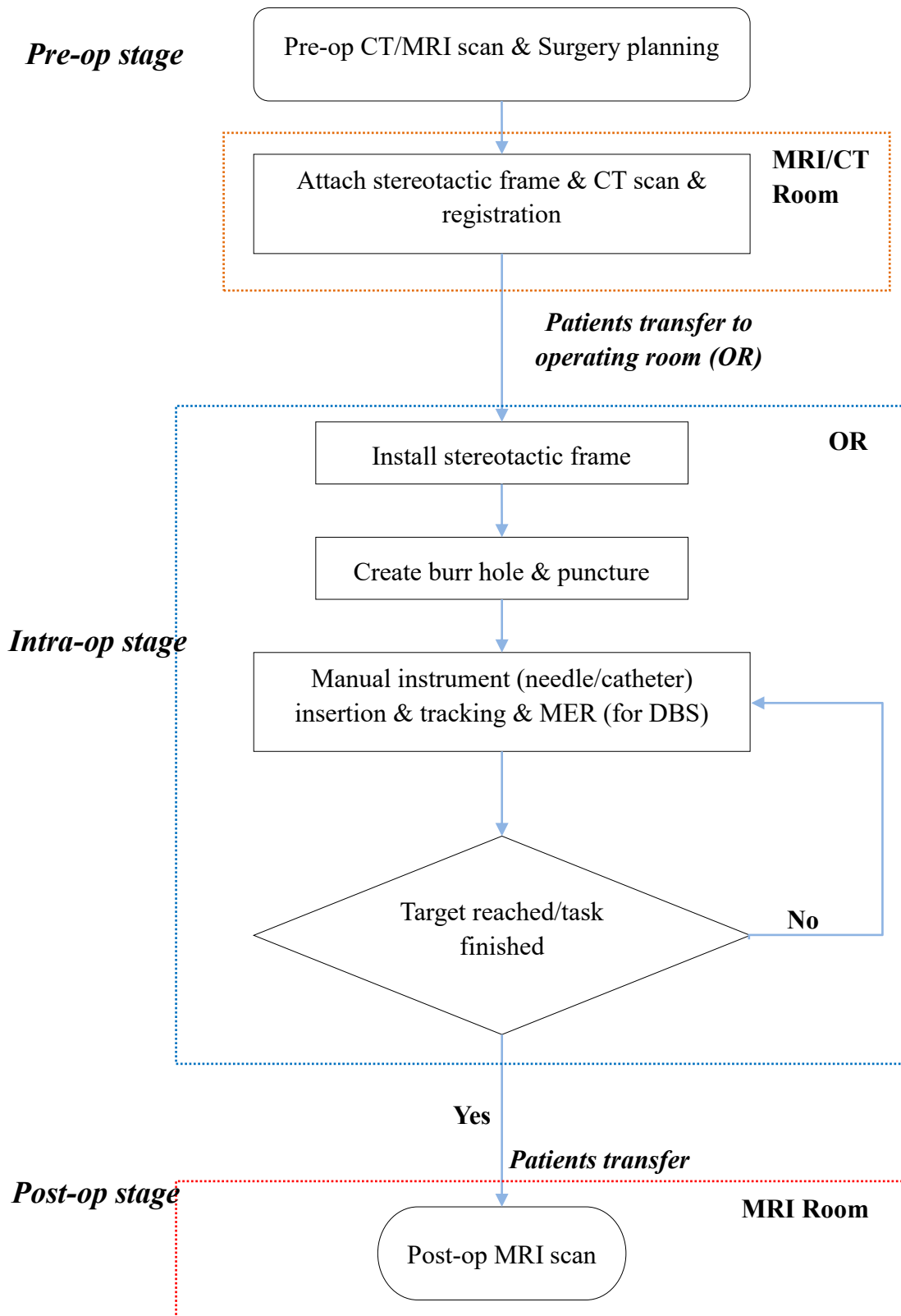


*Figure 1–1 Conventional stereotactic neurosurgical workflow*

However, with increasing demands for the precision and minimal invasiveness in neurosurgery, the above clinical procedure is challenging and often results in non-optimal outcomes. First of all, it is time-consuming (typically 5 to 6 hours with hundreds of steps), which may lead to the tool placement inaccuracy that is related to errors in one or more steps in the procedure. Secondly, patients have to suffer from drilling many holes for fixing stereotactic equipment on their heads. This is extremely painful, especially for awake patients (e.g. Stereo electro encephalography (SEEG) procedure) or children. More importantly, surgical planning that only relies on preoperative images is inaccurate, which is due to the fact that once the dura is opened, the brain shift/deformation (Figure 1-2) unavoidably results in changes of both critical brain structures and lesion target positions.



*Figure 1–2 Brain shift/deformation when the skull is opened [4]*

To address the current neurosurgical challenges, advanced technologies in the real-time visualization of the medical imaging and robot-assisted precision manipulation need to be integrated to achieve the brain shift compensation and streamline workflow. Robot plays a significant role in a lot of fields, such as manufacturing, agriculture, transportation, medicine, etc. Nowadays, with development of robot technologies, surgical robots have been widely used in various clinical procedures, especially in neurosurgery. A lot of surgical robot systems have been developed. Clinical tests have shown promising clinical outcomes compared to traditional surgical procedures, such as reducing the surgery time, improving operation dexterity, as well as increasing the surgical precision [5]. Magnetic resonance imaging (MRI) is a versatile imaging modality as an indispensable tool in the modern diagnostic medicine, it is being developed for diagnostic and therapeutic image-guided interventions (IGIs) due to its

advantages: 1) MRI technology can generate better images than other imaging techniques because of its high soft tissue contrast; 2) MRI can directly acquire tomographic images without the need for software reconstruction; 3) Multi-sequence imaging and various imaging types provide richer image information to clarify lesions; 4) MRI has no ionizing radiation damages to the human body, which is rather beneficial for both the patient and surgeon [6]. Therefore, integrating the real-time MRI-guided technology with surgical robotics for interventions of stereotactic neurosurgery not only can improve the positioning accuracy, reduce the operation time and patient's suffering, but also provide the brain tissue deformation compensation capability by fusing with intraoperative images. Figure 1-3 shows a workflow by applying the MRI-guided robot-assisted system into stereotactic neurosurgery interventions. Comparing with the traditional neurosurgical workflow, the clinical procedure is significantly simplified as well as reducing the operating time.

***MRI-guided Robot-assisted Stereotactic Neurosurgery (2.5-3 hours)***

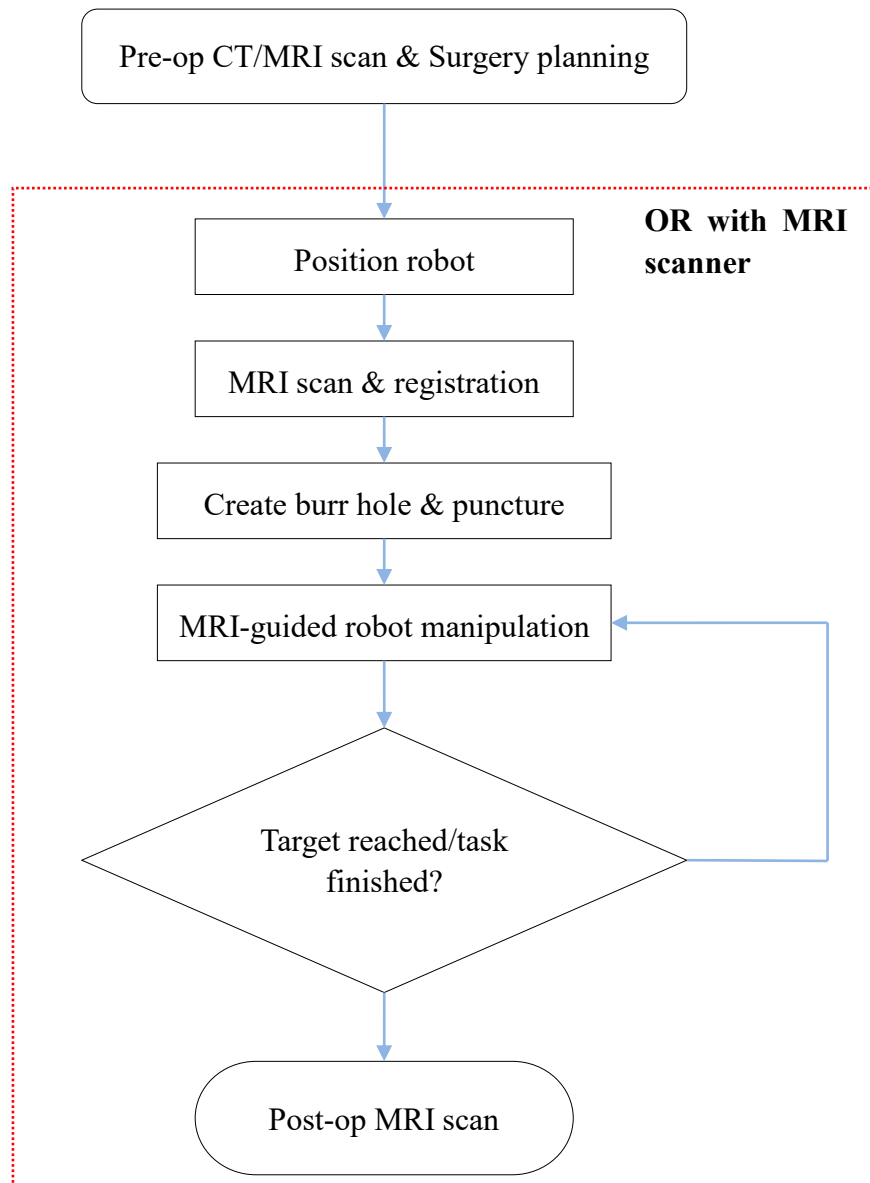


*Figure 1–3 Magnetic resonance imaging (MRI)- guided and robot-assisted stereotactic neurosurgery*

Cubresa Inc. is a Winnipeg-based company dedicated to develop medical devices and intraoperative MRI technologies. The current surgical robot used by Cubresa Inc. is NeuroArm developed by IMRIS Inc., which is a tele-operated robot with two arms designed to work with an intraoperative MRI scanner. However, problems such as the bulky, large footprint, and high needs for extensive training of surgeons limit its applications in the stereotactic neurosurgery.



Thus, in order to improve these problems, a new conceptual design of the MRI-guided robot is proposed in this research to replace the existing NeruoArm robot for better meeting the demands of clinically stereotactic neurosurgical procedures.

## 1.2 Research objectives

The objective of this research is the conceptual design for an MRI-guided robot with the small size and lightweight based on requirements to replace the existing NeuroArm robot. Based on the literature review of conceptual design methods and surgical robot applications, the feasibility of the MRI-guided robot is analyzed. The quality function deployment (QFD) method is utilized to generate design parameters and priorities. As a result, customer requirements are translated into technical specifications for the design to maximize the customer satisfaction. Benchmarking methods are used to compare similar products in the market to identify the target value of design parameters. As a result, the 3D model of an MRI-guided robot is built according to technical metrics. Kinematics analysis and simulation are used to validate the design solution of the robot structure. The simulation of trajectory planning and MR compatibility is conducted for verifying feasibility of the design by considering real clinical procedures and environments.

## 1.3 Thesis contents and structure

This thesis is organized as shown in Figure 1-4. Chapter 1 introduces the research background, motivation, objectives and brief thesis outline. Chapter 2 introduces the development and study of surgical robots, surgical robot systems for stereotactic neurosurgery and applications in the MRI environment. In addition, a review of the conceptual design method is conducted. In Chapter 3, QFD and benchmarking design methods are applied to the conceptual design of the MRI-guided robot, including the identification of customer requirements and design specifications, concept generations for the MRI-guided robot, and the selection of key structures and components. Chapter 4 introduces the kinematic analysis of the proposed MRI-guided robot including forward kinematic modelling and inverse kinematic

modelling, and proposes a trajectory planning approach to achieve obstacle avoidance and vibration suppression based on the safety of the surgery. MATLAB simulation is used to verify accuracy of the kinematic modelling and trajectory planning. In Chapter 5, simulations of the MRI-guided robot compatibility (both the workspace compatibility and MRI environment compatibility) are validated based on the consideration of actual surgical procedures and MRI environments. Chapter 6 concludes the thesis and identifies contributions of the research. Future work is also discussed.

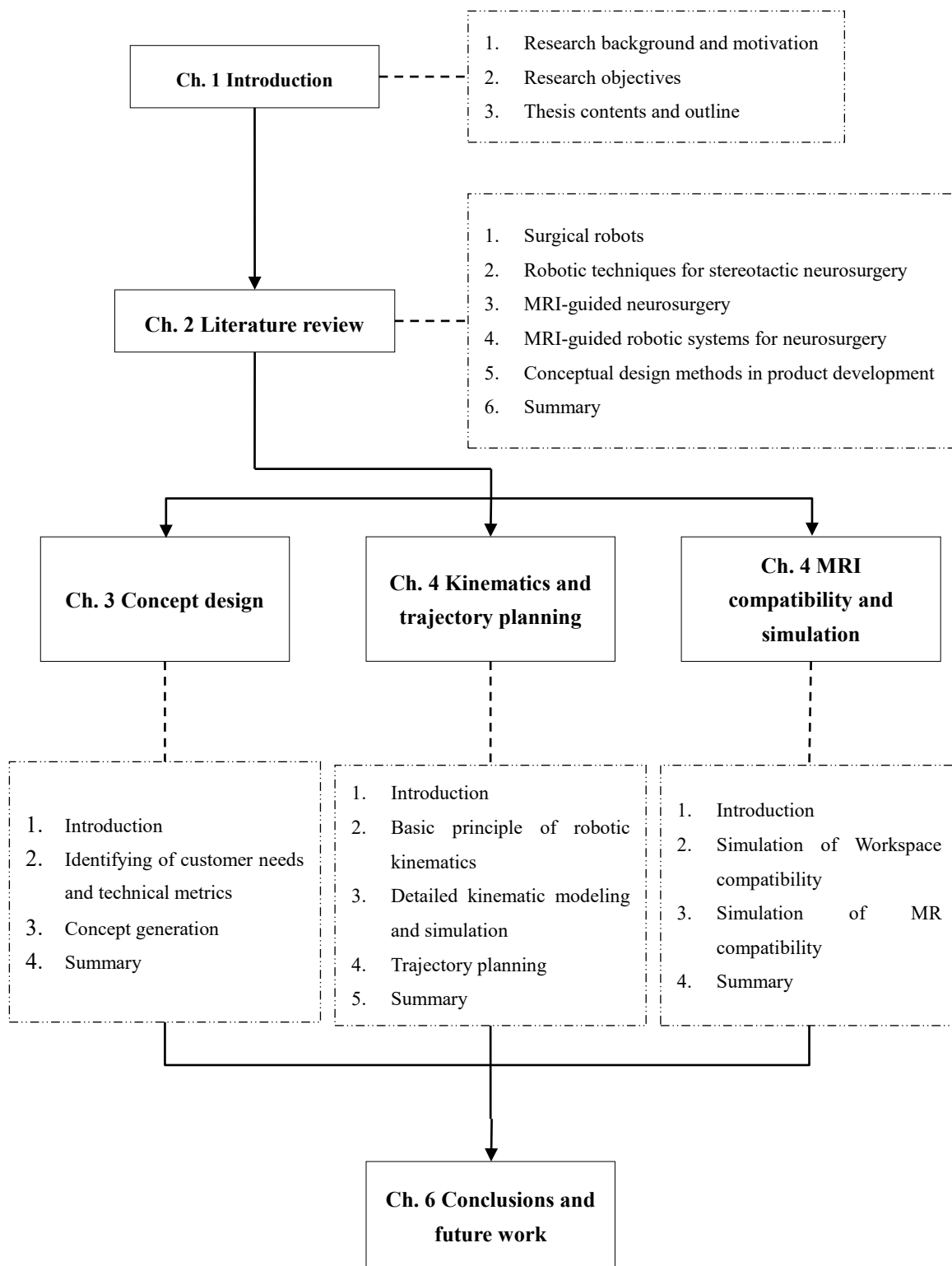


*Figure 1–4 Thesis outline*

# Chapter 2. Literature review

## 2.1. Surgical robots

Different from industrial robots, surgical robots are widely applied in the minimally invasive, high speed and accurate surgery, such as clinical applications of neurological, orthopedics, laparoscopy, and percutaneous operations [7]. With the aid of surgical robots, the clinical surgery has been improved significantly in the remote surgery, minimally invasive surgery, and automated surgery. Comparing with traditional surgical procedures, precision, flexibility and stability of surgical procedures are greatly improved due to the introduction of robotic systems in operating theaters. On the other hand, it also makes the clinical treatment more effective and security, as well as decreasing post-operative morbidity. In addition, with advances in medical imaging technologies (e.g., Xray, CT, and MRI) and technological innovations (e.g., mechanical, material, and control theories), the robotic-assisted therapy has become more acceptable by most surgeons/patients, and have been studied in various research fields. Challacombe and Stoianovici [8] discussed medical robotic techniques including kinematics, mechanical mechanisms and ergonomics, and robotic interventions in the prostate surgery. Gomes [9] reviewed key milestones in the field of surgical robotics, as well as drivers and application limitations for the commercialization of surgical robot products. However, the development and research of surgical robots for the brain stereotactic neurosurgery are still in the early stage.

## 2.2. Robotic techniques for the stereotactic neurosurgery

Due to the high accuracy required for positioning and manipulating surgeries in the brain and the need of comparatively fixed landmarks of the cranial anatomy, robots have been introduced to the neurosurgery instead of conventional stereotactic frame devices. Surgeons are able to perform surgical operations on a microscopic level with higher precision because of the introduction of robot-assisted systems in the operating room. Neurosurgery is a surgical specialty that relies on the medical imaging-guided technology [10]. Traditionally, surgeons

perform preoperative imaging scans and surgical path planning for patients. The stereotactic frame device is then required to be attached to the patient's skull and remains in place during the surgery [11]. Robotic systems can replace stereotactic frames to improve reliability, accuracy, and ease-of-use in neurosurgery [12]. A number of robotic systems based on imaging-guided procedures have been developed over the past few decades. However, a problem in the image-guided neurosurgery is the brain displacement/shift during surgery, which alters the spatial relationship between the preoperative image information and patient's anatomy. This problem can be solved by performing the procedure within the environment of an imaging system that can continuously monitor and acquire real-time intra-brain anatomical structure measurements. This requires robotic manipulators that are compatible with the imaging modality.

### 2.2.1. Conventional stereotactic neurosurgery

Stereotactic neurosurgery is one of the most important diagnostic and treatment approaches available as a minimally invasive neurosurgery procedure. It utilizes imaging localization and positioning devices to guide the placement of microelectrodes, puncture needles, biopsy needles, and other microscopic instruments into specific targets within the brain [11]. By recording electrophysiology, taking tissue specimens, generating lesions or removing lesions, the diagnosis and treatment of various disorders of the central nervous system can be performed. Brain tissue is contained within the skull which is an enclosed spheroid-like space. When operating on intracerebral lesions, it is important to get as close to the lesion as possible and to minimize damage occurring to the normal tissue. The stereotactic frame system ensures the precise location of the lesion during neurosurgery [12].

German neurophysiologist Dittmar systematically introduced the construction principle of framed stereotactic devices and applied them in animal experiments [13]. Russian surgeon Zernov developed a polar coordinate framed stereotactic device based on Dittmar's principle, and first used skull surface anatomical marks to locate human intracranial structures [14]. The first commercial stereotaxic instrument was introduced in 1908 by Drs. Clarke and Horsley who are neurosurgeons in the Royal Hospital of London, UK. This device is completed based

on geometric principles of the 3D Cartesian coordinate system [15]. Figure 2-1 shows the most popular stereotactic frames used by hospitals currently. However, with the application of surgical robots in the field of neurosurgery, the stereotactic frame technology has been replaced by robotic-assisted systems for increasing positioning accuracy, simplifying workflow, and improving surgical outcomes.

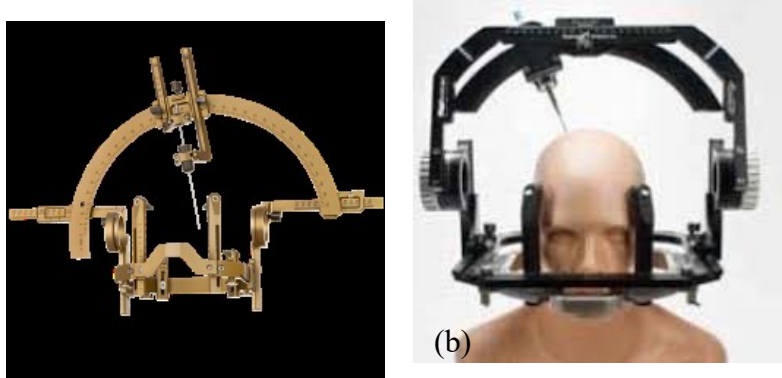


*Figure 2–1 Traditional stereotactic frames: (a) Leksell® Frame; (b) STarFix Frame [11]*

### 2.2.2. Robot-assisted systems for neurosurgery

In the stereotactic neurosurgical procedure, robots are mainly used for precisely positioning brain lesions in space, assisting doctors in clamping and fixing surgical instruments [16]. Initial surgical robotic systems were mostly based on industrial robotic platforms. In 1985, the first neurosurgical robot was introduced by the company of Unimate in America for the brain biopsy through CT-guided precise positioning of the probe by modifying the existing industrial robot PUMA260 [17]. Currently, neurosurgical robots are designed as stand-alone systems, with main functional modules including the system software, mechanical hardware and user interface. The system software development includes surgical planning, the spatial alignment and positioning control. The mechanical hardware part involves the design, machining and fabrication of the robot body and positioning device. The human-computer interaction, on the other hand, mainly considers the interaction between the robot and surgeon based on surgical requirements. From perspective of the user interface, neurosurgical robots

are mainly categorized into three main design configurations, namely, supervisory control system, tele-surgical system, and shared control system (as shown in Figure 2-2).

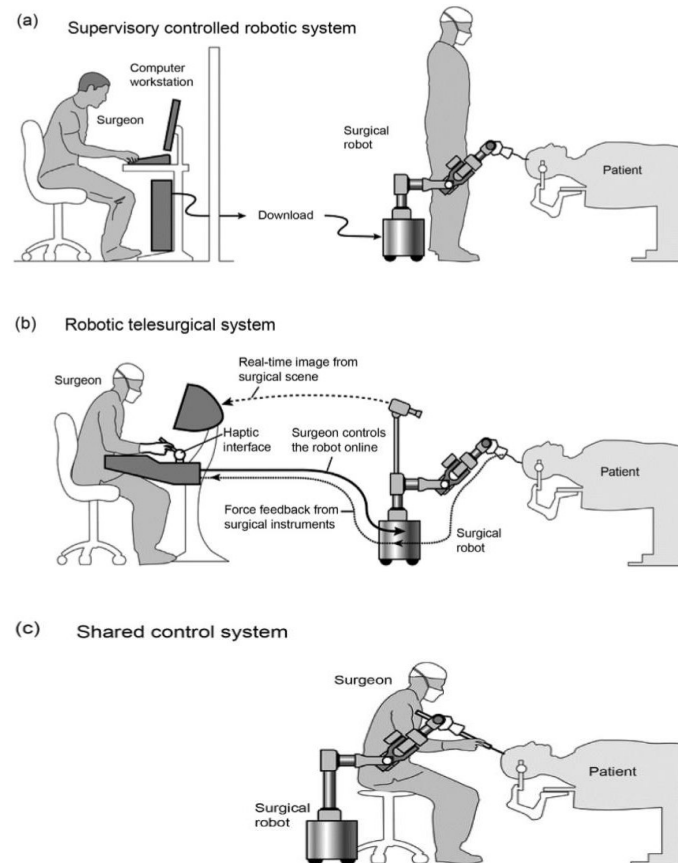


*Figure 2–2 Three robotic systems proposed in [18]; (a) Robots will be operated automatically based on pre-determined/specified actions by surgeons; (b) Surgeons control and manipulate robots remotely and in real-time; (c) robotic end-effectors are manually controlled by surgeons.*

With the improvement of robotic technologies, a variety of robotic systems have been implemented in neurosurgical procedures. While some robotic systems are still in the experimental stage, some have already been commercialized (as shown in Figure 2-3). The most successful robotic surgical system currently available is the da Vinci (Intuitive Surgical, CA, Sunnyvale) [19]. It is a remote-controlled surgical robot based on an endoscopic platform and was originally designed for the cardiac surgery. Now it is widely used for various clinical

procedures such as the general surgery, urology, obstetrics and gynecology. In neurosurgical procedures it is limited to certain skull surgery procedures. NeuroMate (Integrated Surgical Systems, Inc., Davis, CA, USA) [20] is an image-guided and computer-controlled surgical robot system designed specifically for neurosurgery. This robotic system can perform precise image-based surgical planning and execute multiple trajectory paths. It consists of a robotic arm assembly with 5 DoFs and a kinematic positioning software system. It is currently used for processes such as the stereotactic biopsies and functional neurosurgery. PathFinder (Prosurgics, Inc., Cupertino, CA, USA) [21] is another robotic system to guide surgical instruments for needle biopsies with the submillimeter precision, and the placement of drills or burr holes. ROSA is a popular robotic system marketed by Medtech (Montpellier, France), which has been approved by Food and Drug Administration (FDA) and gaining acceptance for stereotactic neurosurgical procedures, including the brain tumor biopsies and electrode placement, and incorporates endoscopic platforms and laser technology for minimally invasive procedures [22]. Although these robotic-assisted systems have been validated for the excellent localization accuracy as well as interventions that simplify the stereotactic neurosurgical process, the lack of real-time image guidance, however, results in the intraoperative brain displacement remaining unresolved thus potentially limiting the application of robots in the stereotactic neurosurgery.



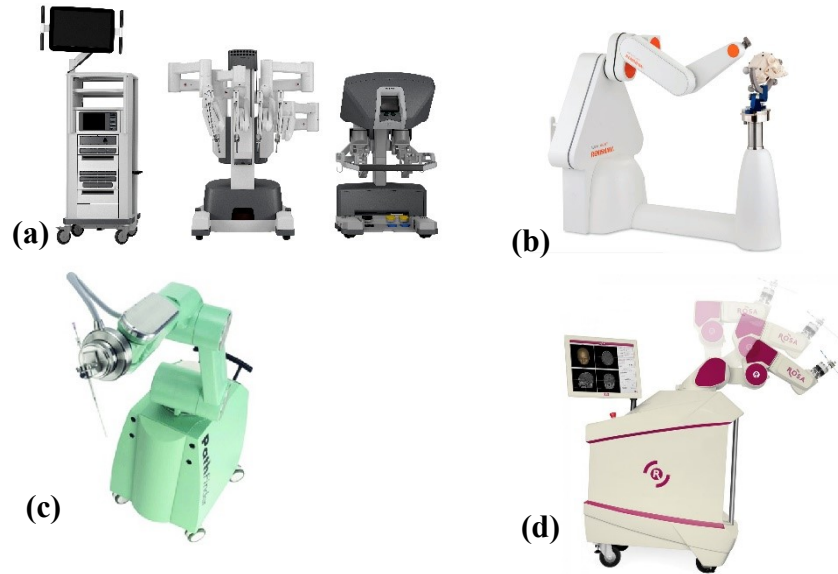


*Figure 2–3 Commercially available robotic systems for stereotactic neurosurgery; (a) da Vinci (Instuitive Surgical, CA, Sunnyvale); (b) NeuroMate (Integrated Surgical Systems, Inc., Davis, CA, USA); (c) PathFinder (Prosurgics, Inc., Cupertino, CA, USA); (d) Rosa (Medtech, Castelnau Le Lez, France)*

### 2.3. MRI-Guided Neurosurgery

Medical imaging is from X-rays, electromagnetic fields, ultrasound and other energy applied to the human body to display the medical information such as the tissue structure and morphology through one-dimensional or multi-dimensional images. Comparing with other medical imaging approaches, Magnetic Resonance Imaging (MRI) is the preferred imaging modality for neurosurgery due to its superior soft tissue resolution and excellent image contrast, as well as no radiation hazards [23]. Magnetic resonance is a physical process in which atomic nuclei with non-zero magnetic moments undergo Zeeman splitting and resonance through the action of an external magnetic field to absorb radio frequency radiation of a specific frequency. MR can draw a relatively complete image of the internal structure of the human body by detecting the distribution information of the water. The robot should be capable of being manipulated even during the imaging process for real-time monitoring of the target position. However, the robotic manipulator cannot produce any negative effects on the imaging, i.e., it

must be unaffected on the imaging process. Therefore, the MRI environment as well as the technology need to be considered. The MRI technology mainly includes MRI scanner, MRI safety and compatibility, MRI compatible materials, and MRI compatible actuators and sensors [24].

### 2.3.1. MRI scanner

Magnetic resonance is a physical phenomenon, which is widely used in physics, chemistry, biology and other fields as an analytical method. It was not used for medical clinical testing until 1973, in a major advancement in medical imaging after CT images. Basic principles of the MR scanner are as follows: 1) the human body is placed in a special magnetic field, and the hydrogen nuclei in the human body is excited by radio frequency pulses to cause the hydrogen nuclei to resonate and absorb energy. 2) After the radio frequency pulse is stopped, the hydrogen nucleus emits an electric signal at a certain regular frequency, and releases the absorbed energy, which is received by a receiver outside the body. 3) The image is obtained by analyzing through computers [23]. Figures 2-4 show the composition and working process of an MRI scanner.

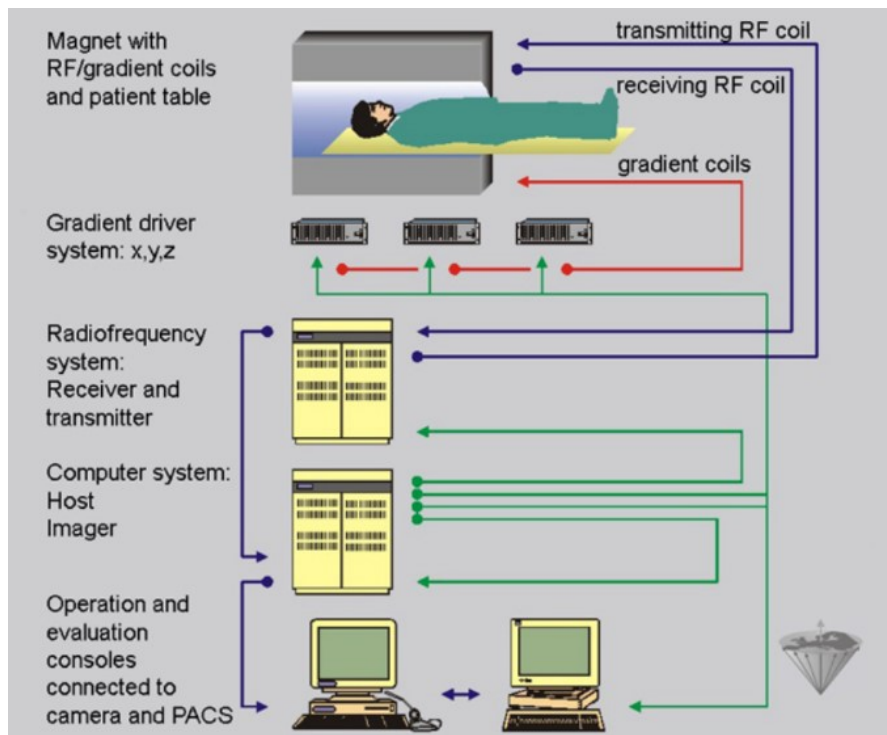





Figure 2–4 MRI scanner components and working principle [24]

Different from the existing clinical imaging technology, MRI can provide more anatomical information, such as cross-sectional, sagittal, coronal plane and various oblique tomographic images. In addition, because of without image artifacts, no requirement for injection of contrast agents, and no ionizing radiation, it is regarded as the most effective clinical diagnosis approach for detecting intracerebral hematomas, brain tumors, cerebral ischemia and other common brain diseases. However, it also has limitations, for example, patients who have pacemakers or with metal foreign cannot be allowed to examine by MRI.

### 2.3.2. MRI Terminology

The equipment used in the MRI environment is susceptible to factors such as strong magnetic fields, fast-switching magnetic field gradients, and radio frequency pulses [24]. Therefore, it is a very challenging task to develop and apply this kind of devices. MRI is a bio-magnetic spin imaging technology which uses the characteristics of the spin motion of the atomic nucleus in an external magnetic field to generate a signal after being excited by a radio frequency pulse. The stronger the magnetic field, the stronger spin motion as well as the MRI signal, which results in a high quality of images. Currently, the magnetic field strength of the MRI scanner, which is widely used in the clinical medicine, is 3.0T (Tesla). In the past 20 years with the improvement of signal-to-noise ratio technologies, the magnetic field strength of MR scanners has gradually increased. Recently, it has been reported that the 7.0T MRI scanner is used in clinical trials, even above 10T MRI device has begun to be studied and tested [25]. As a result, a strong force is applied to ferromagnetic equipment or surgical tools because of the strong magnetic field, which is hazardous for patients, medical staff, and operating equipment, particularly in the stereotactic neurosurgical procedure. The American Society for Testing and Materials (ASTM) classified devices for the MRI environment as the MR safe, MR Conditional and MR Unsafe (ASTM F2503) [26], as summarized in Table 2-1. Hence, in order to ensure the safety and image quality of the MRI-guided equipment, limited materials, actuators, and sensors are used in MRI scanners.

*Table 2-1 Terminology for medical devices in the MR environment according to ASTM*  
*Classification*

Term	Icon	Description
MR safe		Medical devices that will not result in hazard from exposure to any MRI environment
MR conditional		Medical devices that are secure in a MR environment under specified conditions (static magnetic field, converted gradient magnetic field, and RF field conditions).
MR unsafe		Medical devices that present an unacceptable risk to patients, clinicians, or others in the MR environment.

### 2.3.3. MRI compatible materials

Ferromagnetic materials are widely used in robots and electromechanical systems because of their best mechanical properties, such as hardness, strength, and cutting performance. However, when ferromagnetic materials are placed close to the MRI scanner, they are easily attracted by the strong magnetic force to cause safety hazards. In addition, some non-ferromagnetic materials will generate eddy currents inside due to their electrical conductivity, which will cause the materials to generate heat and affect the image quality [24]. Plastics, ceramics, glass fibers, carbon fibers and some composites are non-ferromagnetic and non-conductive, which are ideal MRI-compatible materials. However, the disadvantage of these materials is that their mechanical properties are limited, there will be a negative impact on the operability and accuracy of robot due to a lack of the sufficient mechanical strength. On the other hand, some ferrous metals and non-ferrous metals can be used in the MRI environment, such as aluminum, copper, and 300 series stainless steel [26].

### 2.3.4. MRI compatible actuators and sensors

The use of MRI-compatible actuators is required for robotic systems in MRI environments. Conventional electromagnetic actuators, such as stepper motors, cannot be used since they are not compatible with the MRI environment. Therefore, alternatives that meet the requirements of MRI-compatible applications have been investigated. The most common MRI-compatible

method is the manual actuation which is most often used in MRI-guided robotic-assisted prostate related procedures [27][28].

The hydraulic actuator is another actuation solution that is compatible with the MRI environment. Hydraulic actuators can transmit force through flexible hoses to enable the long-distance operation. Kim et al [29] used this actuation solution to design a six-degree-of-freedom robotic mechanism for the minimally invasive liver surgery, which is used in association with an open MRI scanner. Moser et al [30] studied the use of hydraulically operated master-slave robotic systems for MRI applications in terms of the dynamic performance of the system. However, main problems of this actuator approach are the fluid leakage and gas bubbles from the compressed system. Pneumatic actuators provide a potential alternative for being compatible with MRI environments, which can overcome the shortcomings of hydraulic systems. Comparing with hydraulic actuators, pneumatic actuators offer benefits of cleaner and faster operations that are currently used in commercial robotic assistant systems Inn oMotion (Innonedic GmbH, Herxherm) [31]. Another mainstream actuation approach is the piezoelectric/ultrasonic motor for MRI guidance procedures, its principle is based on the phenomenon of piezoelectricity, i.e. the high-frequency voltage under the effect of piezoelectric ceramics generates ultrasonic vibrations and resulting motion. Since piezoelectric motors generate non-electromagnetic fields, they are theoretically able to meet application requirements for the MRI environmental compatibility. Wang et al [32] tested the application of piezoelectric/ultrasonic motors in an MRI environment and proposed factors affecting the MRI compatibility of ultrasonic motors as well as approaches to improve the compatibility. Commercially available ultrasonic motors have advantages such as the high torque, small size and compactness, which makes them the preferred solution for driving MRI-guided robotic systems. The remote-control drive can be achieved using drive shafts, belts, chain drives and cable drives.

The safety and precise control of any mechatronic devices or robots require a closed-loop control consisting of position or force feedback sensors. Koseki et al [33] built a laser micron system using a charge-coupled device where the position repeatability of the MR-compatible operating mechanism was tested in an MRI environment. Takashashi et al [34] developed a 6-

axes sensor using a fiber optic device to address requirements of the MRI environment compatibility. In addition, Gassert et al [35] proposed a similar sensor for MR-compatible devices.

## 2.4. MRI-guided robotic systems for neurosurgery

Over the past decades, a number of MRI-compatible robotic systems have been developed and applied to interventions in various clinical procedures. These efforts have demonstrated the feasibility as well as challenges involved in developing such robotic systems. These robotic systems utilize different structures with different kinematics, materials and actuators depending on the clinical needs and objective applications. This section aims to present a comprehensive literature review of MRI-compatible robotic systems for brain neurosurgery and stereotactic applications. Table 2-2 summarizes MRI-guided robotic systems with key features and limitations according to different neurosurgical applications, including the brain ablation, electrode implantation, and brain biopsy.

*Table 2-2 Summary of the state-of-the-art MRI-guided robotic systems for neurosurgery*

Project name	Phase	Features	Limitations
NeuroArm (IMRIS®, Minnesota, USA) Sutherland et al. [36]	FDA approved, commercial	Teleoperation & microsurgery; 2 robotic arms; 7 + 1 DOF (1 DOF automatic needle insertion); Piezoelectric motor; MRI compatible materials.	Large footprint; Kinematic redundancy; N/A for positioning;
Pneumatic MRI-compatible needle driver (Vanderbilt University, USA) Comber et al. [37]	Clinical trial	Transforamenal Ablation Concept; Fit 3.0T closed-bore MRI scanner; Only 2 DOF; Pneumatic motor; 3D printing for fabrication	Low precision; Lack of flexibility; Noisy
WPI robot (Worcester Polytechnic Institute, USA) Li et al. [38]	Research prototype	Needle-based neural interventions; Mounted at MRI table; 6 + 1 DOF (1 DOF automatic needle insertion); Piezoelectric motor; MRI compatible materials	Motor heating in MRI bore; Inconvenient maintenance; Safety concerns with sterilization; Non-portable
MR-safe bilateral stereotactic robot (The	Research prototype	Bilateral stereotactic neurosurgery; skull-mounted; 8	Single Application (only DBS procedure); Limited

University of Hong Kong, Hong Kong) Guo et al. [39]		DOF & 2 end effectors; Hydraulic motor; MR safe materials	bandwidth results in network delays; Surgical ergonomics
MRI-compatible needle insertion manipulator (University of Tokyo, Japan) Masamune et al. [40]	Research prototype	Needle placement; Fit 0.5T MRI scanner; 6 DOF; Piezoelectric motor; MRI safe materials	Low precision; Required dedicated MRI scanner; Low payload; Limited MRI environment.
Open MRI compatible robot (Beihang University, China) Hong et al. [41]	Research prototype	Brain biopsy; 0.3T intraoperative MRI scanner; 5 DOF; Piezoelectric motor; MRI compatible materials	No feedback sensor; Limited MRI environment; Lack of flexibility; Surgical ergonomics

## 2.5. Conceptual design methods in product development

### 2.5.1. Quality function deployment (QFD)

The basic criteria of design are directly related to meet customer needs. QFD is a common method used in product design to satisfy customer needs [42]. QFD is a systematic approach to transfer customer needs into product specifications [43]. In other words, the voice of the customer is translated into the voice of engineers. Toyota adopted the QFD method resulting in a significant reduction in product development time and cost [44]. In the design of the braking system, Dimsey and Mazur [45] improved the performance of the brake system by using the QFD method. Major components such as the master cylinder and caliper were analyzed based on the relationship matrix of quality characteristic priorities to reduce the cost. Bevilacqua et al [46] and Bhattacharya et al [47] applied the QFD method in the procurement and management of products to reduce costs and increase efficiency.

In recent years, QFD has been gradually applied to the medical field. Al-Bashir et al [48] improved the maintenance management system (MMS) for medical equipment using the QFD method to achieve customer satisfaction and improve the safety and reliability of medical equipment. Shi et al [49] proposed a method for prioritizing customer needs to integrate QFD and Kano models. The method was applied in the design of a medical service robot. In addition,

some additional studies of the medical robot design using the QFD method are given in Table 2-3.

*Table 2-3 Literature of QFD in the medical robot design*

Year	Author	Methods	Application field
2010	Huang et al [50]	QFD	Hand rehabilitation robotic system
2013	Luna-Avilés et al [51]	QFD, Analytic Hierarchy Process (AHP)	Improvement of robot-assisted system for Non-resectable Liver Tumors
2014	Han et al [52]	QFD	Vitreoretinal surgical robot design
2016	Mocan et al [53]	QFD, AHP, TRIZ	Development of a robotic driven handheld laparoscopic instrument for non-invasive intraoperative detection of small endoluminal digestive tumors
2016	Zhu et al [54]	Axiomatic Design (AD), QFD	Lower limb rehabilitation robot design
2019	Wang et al [55]	Fuzzy-QFD; Fuzzy-AHP.	Hand training device design and implementation

As shown in the above studies, QFD can be used in a variety of applications to improve product development. According to Table 2-3, although the QFD method has been applied to the development and optimization of medical robots, it has not yet been applied to the design of stereotactic neurosurgical robotic products.

### 2.5.2. House of quality (HoQ)

House of Quality (HoQ) is a central tool in QFD that allows users to ensure that their requirements can be translated into engineering characteristics [43]. By building HoQ, it is possible to visualize key information such as the conflict between requirements and engineering characteristics, market competition, and the importance of requirements using a matrix format. Customer requirements are used as input of the matrix to decide product specifications. The structure of a HoQ is shown in Figure 2-5.



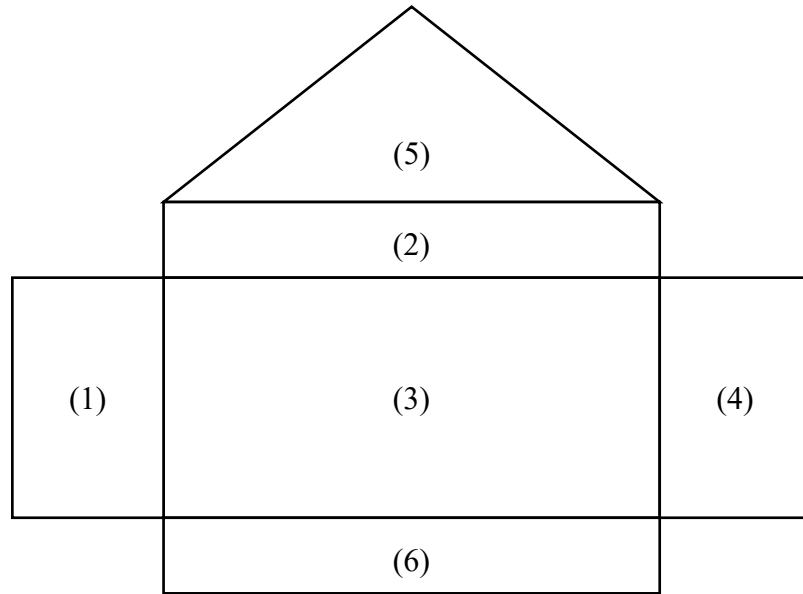


*Figure 2–5 Structure of HoQ*

(1) Left wall - Customer Requirements and Importance

Customer requirements (CRs) can be decided by different ways such as user interviews, literature reviews, questionnaires, etc. The results are called Voice of Customer (VoC). After collecting the VoC, CRs are classified by performance, reliability (including usability, reliability, and maintainability), economy (including design cost, manufacturing cost, and usage cost), and appearance, applied in HoQ. The importance of CRs are determined according to criteria and assigned values. A higher value indicates a higher level of importance.

(2) Ceiling – Technical Requirements

From the technical perspective, the design requirements for the product (engineering measures) are proposed to clarify the quality characteristics of the product which should be available.

(3) Room – Inter-relational Matrix

It forms a matrix of correlations between consumer requirements and technical requirements.

(4) Right Wall - Market Competitiveness Assessment

From meeting customer requirements perspective, the competitive ability of this product is evaluated to compare other similar products in the market.

(5) Roof – Technical Requirements Correlation Matrix

It lists possible conflicts of technical requirements. The engineering characteristics may be either mutually supporting or contradictory.

(6) Basement – Design targets

It indicates technical priorities to be implemented based on relationships of customer requirements and engineering characteristics.

Although HoQ is able to address the conflict between CRs and technical specifications, the detailed design specifications (e.g., size, weight, critical components, etc.) are determined using other tools.

### 2.5.3. Integrating QFD and Benchmarking methods

Benchmarking is a useful tool to improve design solutions by identifying and applying the best demonstrated practice of products in the market. In the design stage, it can be used for searching existing products' best scheme of design to obtain optimized product details [56]. Designers can improve their design solution by tailoring and incorporating these best practices into their own design, not by imitating, but by innovating. Therefore, by comparing different products' performances in the market, the best product details from benchmarking products can be determined. Therefore, the benchmarking method can improve the design solution.

Therefore, solutions of the product design to meet customer satisfaction can be improved by integrating QFD and Benchmarking methods. Shen et al [57] improved performance of the product design by using benchmarking in QFD in decision-making. Kumar et al [58] applied QFD and benchmarking methods to improve the product and process design. As a result, the best design solutions can be formed. Also, they proposed a framework of using QFD and benchmarking methods to redesign and modify existing processes to reduce product cost and increase the product efficiency.

In this thesis, integrating QFD and Benchmarking methods is utilized for the MRI-guided robot design. QFD method is used to identify and map technical specifications based on CRs.

The benchmarking method is employed in the detail design of the MRI-guided robot by selecting similar components of surgical robots in terms of functions.

## 2.6. Summary

Surgical robots can improve neurosurgical outcomes due to advantages such as high precision, stability, and dexterity. A number of neurosurgical robots and techniques have been reviewed in this chapter. In image-guided neurosurgical procedures, the robot can use MRI data to guide a surgical tool or instrument in the treatment site within patient's skull. Various real-time image-guided MRI-compatible robots have been developed to address the problem of "brain displacement/shift" during neurosurgical procedures. Because of specific limitations associated with the MRI environment, developing such a robot is a challenging task. In order to solve these problems, researchers have developed MRI-compatible materials, actuators, and sensors based on MRI technologies to reduce the negative impact of the robot on the MRI environment. QFD is an effective design method to meet customer needs, and Benchmarking is an efficient approach for the concept generation. Many successful products have been developed by using these methods. Building on the reviewed research, this research work proposes a conceptual design of the MRI-guided robot for stereotactic neurosurgical interventions.

# Chapter 3. MRI-guided robot conceptual design based on QFD and Benchmarking methods

## 3.1. Introduction

In this chapter, a conceptual MRI-guided surgical robot for the stereotactic neurosurgery is proposed by using Quality function deployment (QFD) and Benchmarking methods. The aim is to improve the existing surgical robot based on customer requirements (CRs) to reduce the size and weight as well as solving the MRI-compatibility problem. Following parts of this chapter are organized as follows. Firstly, CRs and product specifications (PSs) for the MRI-guided robot are introduced. Next, three benchmarking stereotactic neurosurgical robots are analyzed to guide design of the MRI-guided robot. Finally, some significant components of the robot and main structure are proposed.

This chapter is organized as follows. Section 3.2 identifies CRs and technical metrics as well as relationships of them for the MRI-guided robot. Section 3.3 introduces the conceptual generation of the MRI-guided robot by using HoQ and benchmarking methods. The chapter is summarized in Section 3.4.

## 3.2. Identifying of Customer Needs and Technical Metrics

### 3.2.1. Customer requirements

To identify CRs, a survey is conducted to collect data via a series of questions using the customer interview and literature review. Consequently, a number of initial customer requirements, such as the automatic control, compact structure, accuracy and durability, is collected after studying and analyzing customer response as well as references.

In order to better understand CRs, initial CRs are converted into specific requirements. For example, the initial requirement "Automatic control" is converted into (CR.1) Motor drive and

(CR.2) shared control specifically. Thirteen expected needs are obtained after converting customer's initial needs into specific needs, as shown in Table 3-1.

In addition, in order to understand the priority of CRs, after determining specific CRs, a scale of 1 to 5 is used to assign each CR based on the customer survey feedback so that CRs are quantified for different important levels. Where, value 5 represents the most important, value 1 means the least important. Results show that needs of CR.1 Motor drive, CR.3 Small size, CR.7 MRI safe/conditional, and CR.12 Reduce surgical time are customer's most concerned demands.

*Table 3-1 Customer needs and importance rates of MRI-guided robot*

Category	Initial Needs	No.	Specific Needs	Imp. rates
Performance	Automatic control	CR.1	Motor drive	5
		CR.2	Shared control	3
	Compact structure	CR.3	Small size	5
		CR.4	Light weight	4
	Flexibility	CR.5	Flexible motion	5
		CR.6	Be movable	2
Imaging Technology	MRI Technology	CR.7	MRI safe/conditional	5
Safety	Monitoring	CR.8	Real-time feedback	5
	Accuracy	CR.9	Precise positioning	5
Reliability	Easy to maintain	CR.10	Simple structure	2
	Durability	CR.11	Long service time	3
Clinical Outcomes	Improvement of surgical process	CR.12	Reduce surgical time	5
		CR.13	Quiet	3

### 3.2.2. Technical metrics

Table 3-2 shows decided technical metrics (TMs) for the MRI-guided robot design. For example, TM.1 Motor type and TM.2 Payload (N) are translated into an efficiency design indicator associated to CR.1 Motor drive. TM.4 Total size of robot and TM.5 Total mass of robot are associated to CR.3 Small size and CR.4 Lightweight, respectively. For example, decreasing TM.15 total running time and TM.16 noise is the design target to satisfy CR.13. Increasing TM.11 positioning accuracy and TM.7 reachable workspace can improve the surgical safety.

*Table 3-2 Technical Metrics*

CRs (No.)	No.	Technical Metrics	Unit/Type
CR.1	1	Motor type	Piezoelectric/Hydraulic/Pneumatic
	2	Payload	N
CR.2	3	Control mode	Supervisory/Tele-surgical/Shared control
CR.3	4	Total size	mm
CR.4	5	Total mass	kg
CR.5	6	Degree of freedoms	DOF
	7	Reachable workspace	mm <sup>3</sup>
CR.6	8	Mounting method	MRI table/Mobile wheel
CR.7	9	Material properties	MR safe/conditional
CR.8	10	Sensor type	MR safe/conditional
CR.9	11	Positioning accuracy (End-effector)	mm
	12	Motion velocity (End-effector)	m/s
CR.10	13	Modular design	Yes/No
CR.11	14	Product life	Hours
CR.12	15	Total running time	Minutes
CR.13	16	Noise	dB

After technical measures are decided to meet CRs of the MRI-guided robot, such as types of the motor, sensor and materials, robot size and mass, the design priority and target specifications can be detailed such as the product size value, weight value, robot running speed

value, and motor and sensor models. In the next section, HoQ and benchmarking methods are utilized to decide the design priority and detail specifications.

### 3.3. Concept generation of the MRI-guided robot

#### 3.3.1. Relationship matrix of CRs and TMs

QFD shows the relationship between CRs and TMs in Figure 3-1 to determine TMs priorities of the design based on priority or weight of each TMs.

		Correlation Matrix			
		Technical Metrics			
Customer Needs	Imp. Rate	TM <sub>1</sub>	TM <sub>2</sub>	TM <sub>j</sub>	TM <sub>m</sub>
CR <sub>1</sub>	$d_1$	$a_{11}$	$a_{12}$	$a_{1j}$	$a_{1m}$
CR <sub>2</sub>	$d_2$	$a_{21}$	$a_{22}$	$a_{2j}$	$a_{2m}$
CR <sub>i</sub>	$d_i$	$a_{i1}$	$a_{i2}$	$a_{ij}$	$a_{im}$
CR <sub>n</sub>	$d_n$	$a_{n1}$	$a_{n2}$	$a_{nj}$	$a_{nm}$
<b>Absolute weight</b>		$w_1$	$w_2$	$w_j$	$w_m$
<b>Relative</b>		$r_1$	$r_2$	$r_j$	$r_m$

Figure 3–1 Relationships matrix of CRs and TMs

Absolute weights are decided by Equation (3-1).

$$w_j = \sum_{i=1}^n a_{ij} d_i \quad (3-1)$$

Relative weights are as follows.

$$r_j = \frac{w_j}{\sum_{i=1}^m w_j} \quad (3-2)$$

where,  $w_j$  is the absolute weight of each TMs;  $a_{ij}$  is the relationship value between CRs and TMs;  $d_i$  is importance of the  $i_{th}$  customer need; and  $r_j$  is a relative weight of each TMs.

According to Figure 3-1, relations between CRs and TMs for the MRI-guided robot are built in Table 3-3 using CRs with the importance rate and technical metrics in Table 3-1 and Table 3-2, respectively. Relationships of CRs and TMs are defined using weak ( $W=1$ ), moderate ( $M=5$ ), and strong ( $S=9$ ).

Absolute and relative weights for each TMs are obtained using Equations (3-1) and (3-2) as shown in Table 3-3. According to the relation matrix of CRs and TMs, TM.1 motor type is the first priority to be considered in the conceptual design. According to the TMs rank, TM.8 Mounting method and TM.13 Modular design are considered at the last.



Table 3-3 Relations between CRs and TMs

CRs \ TMs																	
	Importance Rate	TM <sub>1</sub> Motor type	TM <sub>2</sub> Payload	TM <sub>3</sub> Control mode	TM <sub>4</sub> Total size	TM <sub>5</sub> Total mass	TM <sub>6</sub> Degrees of freedom	TM <sub>7</sub> Reachable workspace	TM <sub>8</sub> Mounting type	TM <sub>9</sub> Material properties	TM <sub>10</sub> Sensor type	TM <sub>11</sub> Positioning accuracy	TM <sub>12</sub> Motion velocity	TM <sub>13</sub> Modular design	TM <sub>14</sub> Total product life	TM <sub>15</sub> Total running time	TM <sub>16</sub> Noise
CR <sub>1</sub> Motor drive	5	9	5		5	5			5	9		5	9			5	5
CR <sub>2</sub> Shared control	3			9								1					
CR <sub>3</sub> Small size	5	5	5		9	5	1	9	1		1	5	1				
CR <sub>4</sub> Light weight	4	5	5		5	9	1	1		9	1	5	1				
CR <sub>5</sub> Flexible motion	5				5	5	9	9				5	5				
CR <sub>6</sub> Be movable	2							1	9								
CR <sub>7</sub> MRI safe/conditional	5	9								9							
CR <sub>8</sub> Real-time feedback	5										9	5					
CR <sub>9</sub> Precise positioning	5	5	9				5	5			5	9	9				
CR <sub>10</sub> Simple structure	2				5		5							9			
CR <sub>11</sub> Long service time	3	1													9		
CR <sub>12</sub> Reduce surgical time	5															9	
CR <sub>13</sub> Quiet	3	5															9
Absolute weight		277	167	52	179	156	144	213	35	242	133	231	219	35	52	115	81
Relative score		12	7	2	8	7	6	9	1	10	6	10	9	1	2	5	3
Rank		1	7	13	6	8	9	5	16	2	10	3	4	16	13	11	12

### 3.3.2. Benchmarking competitors and design target of TMs

In order to decide detail structure specifications for the MRI-guided robot, three robots with similar functions and applications in the market are selected for benchmarking as shown in Figure 3-2. They are Cirq<sup>®</sup> Robot [59], ROSA<sup>®</sup> Robot [22], and NeuroArm<sup>®</sup> Robot [36]. All of these three robots have been approved by Food and Drug Administration (FDA), and are currently used in various clinics, particularly in the stereotactic neurosurgery. However, Cirq<sup>®</sup> Robot and ROSA<sup>®</sup> Robot cannot be used in MRI environments because of MR unsafe materials, which cannot meet CR.7 MR safe/conditional. NeuroArm<sup>®</sup> Robot is MR safe that can be used in MRI environments, however, its drawbacks such as the large footprint, high weight, and kinematic redundancy cannot meet customer needs in our case. In order to optimally meet customer needs, these three neurosurgical robots will be analyzed as competitors and benchmark products to generate the concept of the MRI-guided robot in this study.



*Figure 3–2 Three robotic manipulators*

Details of these robots are obtained from their websites, including the size and mass, degrees of freedom, and product life. Others are obtained from publications in [61-65]. TMs of benchmarking products listed in Table 3-4 can basically correspond to all 13 CRs in Table 3-1. Furthermore, targets of design specifications for the MRI-guided robot can be decided based on three benchmark robots as shown in the right column of Table 3-4.

*Table 3-4 Specifications of three robot manipulator benchmarks*

Robot Specification	Product A	Product B	Product C	Target Value
Motor type	/	Servo motor	Piezoelectric motor	Piezoelectric motor
Payload	3kg	5kg	2kg	5kg
Control mode	Shared control	Supervisory control	Tele-surgical control	Shared control
Total size (Max. Arm length)	850mm	1050mm	910mm	<850mm
Total mass	11kg	21kg	18kg	<11kg
Degree of freedoms	6	6	7	6
Mounting method	Mounted on patient's bed	Mounted on mobile base	Mounted on mobile base	Mounted on mobile base
Material properties	MR unsafe	MR unsafe	MR safe	MR safe
Sensor type	Rotary encoder	Rotary encoder	Rotary encoder + Force sensor	Rotary encoder
Positioning accuracy	1.83mm	1.17mm	1.23mm	≤1.2mm
Motion velocity	/	500mm/s	200mm/s	200mm/s
Total product life	30.000	25.000	25.000	30.000
Total running time	/	30 minus	/	30 minus
Noise	< 30 dB	40 dB	30 dB	30dB

CRs of the benchmarks are further evaluated for setting target specifications of the proposed robot as shown in Table 3-5. The assessment is made by engineers who have many years work experience in the MRI product development.

*Table 3-5 Rates of the three benchmarks*

CRs	Rating of the three Benchmarks				
	Evaluation score: 1-lowest; 5-highest				
	1	2	3	4	5
CR <sub>1</sub> Motor drive	A/B				C
CR <sub>2</sub> Shared control	C		B		A
CR <sub>3</sub> Small size	B			C	A
CR <sub>4</sub> Light weight	B			C	A
CR <sub>5</sub> Flexible motion				A/B	C
CR <sub>6</sub> Be movable	A/C				B
CR <sub>7</sub> MRI safe/conditional	A/B				C
CR <sub>8</sub> Real-time feedback				A/B	C
CR <sub>9</sub> Precise positioning	A			C	B
CR <sub>10</sub> Simple structure	C			B	A
CR <sub>11</sub> Long service time				B/C	A
CR <sub>12</sub> Reduce surgical time	B		C		A
CR <sub>13</sub> Quiet				B	A/C

Finally, all the information is integrated into a HoQ as shown in Figure 3-3. From the results, the top three priority technical metrics for the MRI-guided robot design are TM.1 Motor type, TM.9 Material, and TM.11 Positioning accuracy, which should be considered firstly in the design process. In addition, the correlation matrix (see the roof of HoQ) shows that there is a negative impact between TM.1 Motor type and TM.4 Total product size. However, according to the rank of TMs, the TM.1 Motor type is considered in preference to TM.4 Total robot size. Finally, according to results of three benchmarking robots evaluations, our MRI-guided robot's target design specifications can be defined to meet the CRs. This HoQ will be used to guide the MRI-guided robot design.

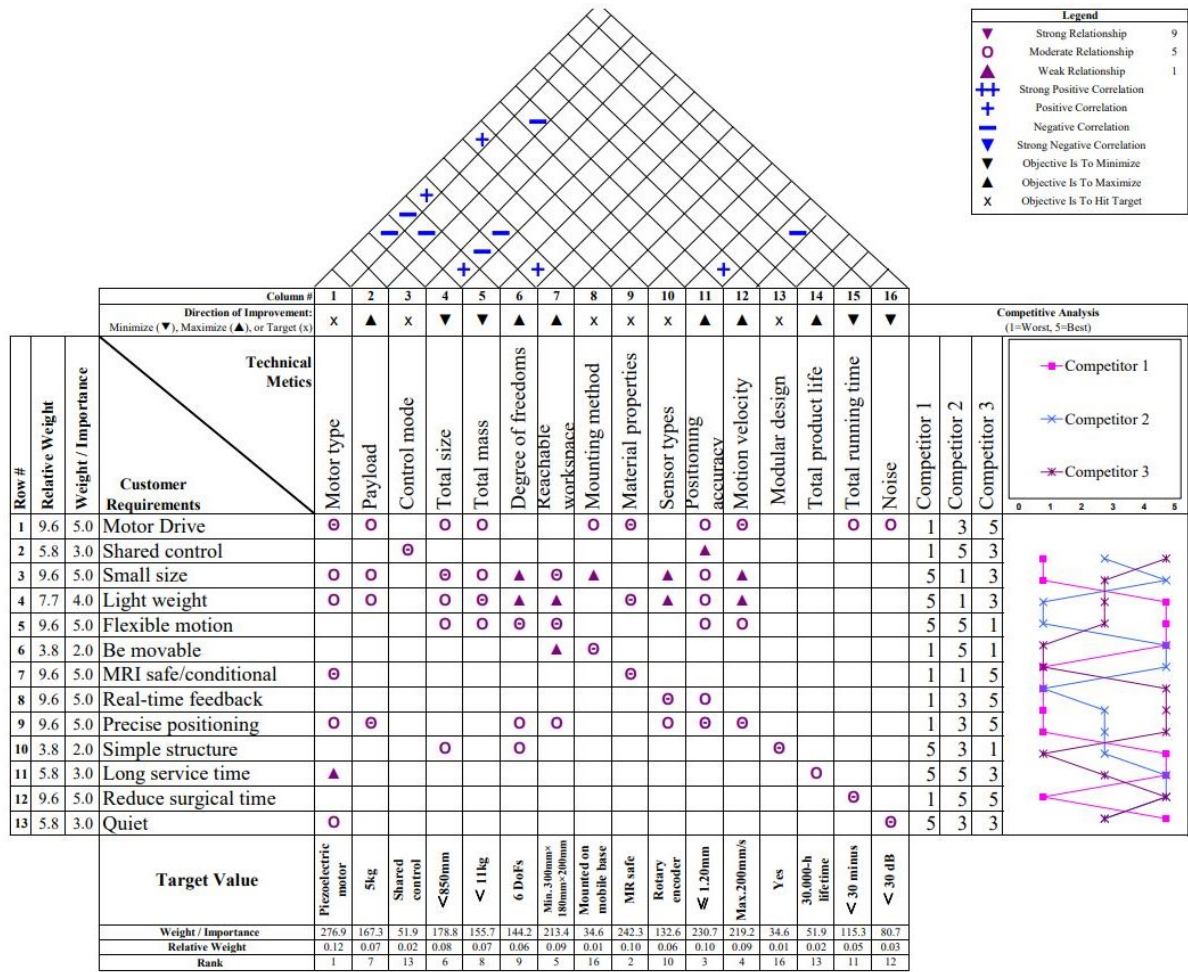


Figure 3–3 HoQ of the MRI-guided robot manipulator

### 3.3.3. Scheme of the robot structure

The main structure of the robot can be formed based on HoQ and benchmarking methods. In the traditional neurosurgical procedures, neurosurgeons need to position the tip of the needle/catheter on the puncture point of patient's head (typically for scalp incision 5mm, skull drilling 2.5mm), and then adjust the angle of the needle/catheter to align the skull hole [38]. Finally, the needle/catheter will be inserted into patient's head to reach the internal lesion area or target. It is required that the neurosurgeon must repeatedly adjust the posture and entry point of the end effector (needle/catheter) to obtain the best surgical path, using operations of the 6 degrees of freedom (DOF) [40].

Additionally, considering inverse kinematics, Pieper Criteria [66] is utilized for

mechanical design of the robot manipulator as follows. (1) Centerlines of three adjacent joints are parallel to each other, (2) centerlines of three adjacent joints intersect at one point. As a result, according to the second measures of Pieper Criteria and structural design of the reference ROSA robot, the proposed 3D model of the robot manipulator is built as shown in Figure 3-4. The proposed MRI-guided robot manipulator consists of a base and 6 linkages, connected by 6 rotational joints. Where axes 4, 5, and 6 are positioning modules, and axes 1, 2, and 3 are orientation modules of the robot. At the end of the robot manipulator, a guide needle/catheter holder is mounted as an end-effector to guide the needle/catheter insertion.

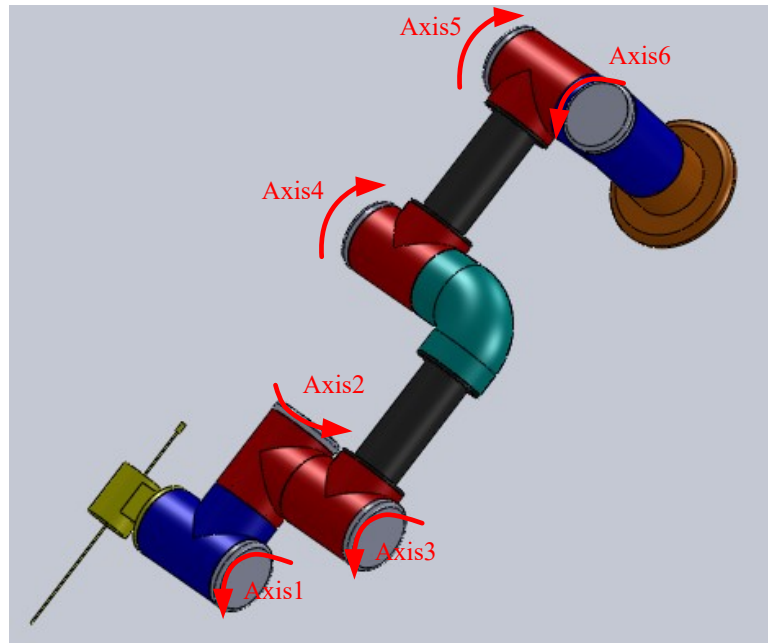


*Figure 3–4 Proposed MRI-guided robot manipulator*

According to the MRI scanner purchased by most hospitals, here, the Siemens MAGENTOM Skyra model MRI scanner is taken as an example. The inner diameter of the MRI scanner is 700mm, and the magnet length is 1800mm. According to requirements of the neurosurgery, as shown in Figure 3-5, the reachable working range of the end-effector of the robot arm should not be less than 700mm × 700mm × 700mm in X-Y-Z directions.

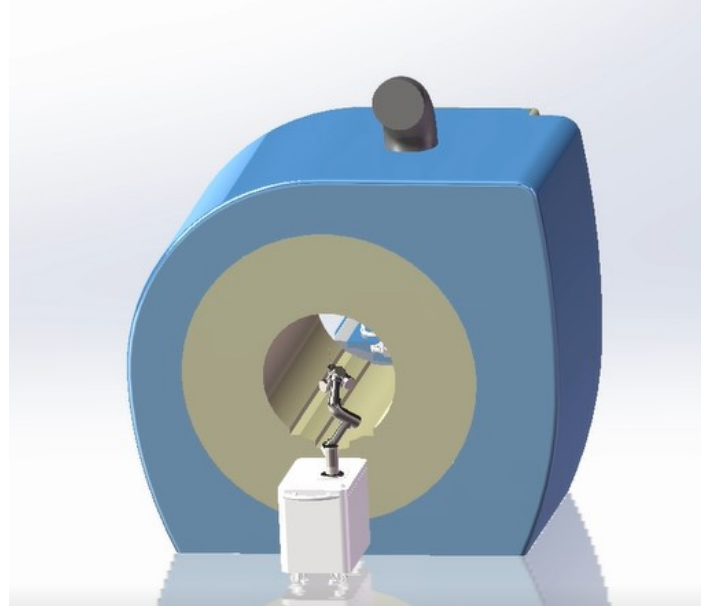


*Figure 3–5 The placement of the robot manipulator in neurosurgical operations*

Figure 3-6 shows that the maximum length of the robot manipulator is 719 mm, which is smaller than other three benchmarking products to meet requirements of the clinical surgery.

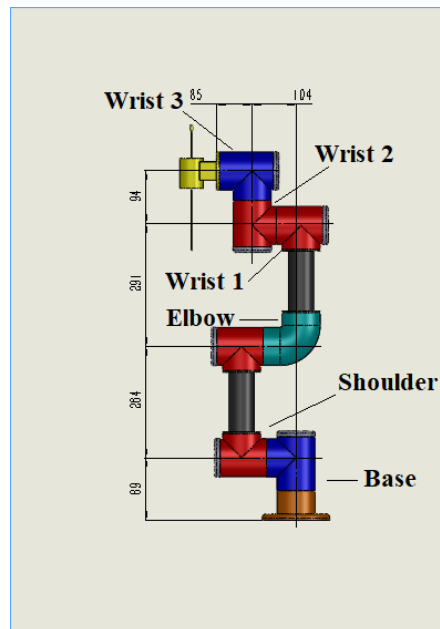


*Figure 3–6 Dimensions of the robot manipulator*

### 3.3.4. Selections of actuators and materials

For the driver compatibility, as the robot works under the strong magnetic field generated by the MRI scanner, materials that are easily magnetized cannot be used, which results in the most common servo motors on industrial robots not being used. The servo motor works in the electromagnetic induction. A certain degree of the magnetic field and radiation will be generated in its circuit, which will interfere with the magnetic field in the MRI scanner to affect the quality of the image. The servo motor can be attracted by the electromagnetic force to produce displacement errors. Furthermore, the material of the traditional servo motor mainly consists of strong magnetic materials.

Three candidates of driving approaches that can be used in the MRI environment safely are pneumatic, piezoelectric, and hydraulic, respectively. Table 3-6 analyzes both advantages and disadvantages of these driving methods.

*Table 3-6 Comparison of different driving schemes*

Driving Approach	Advantages	Disadvantages
Ultrasonic and Piezoelectric Motor	Low speed, high torque, high precision; Good controllability; Low noise; Long lifetime; Small size;	Expensive.
Hydraulic Actuator	Large power; Flexible installation; Force control capability.	Risk of potential fluid leakage; Not suitable for long-distance transmission.
Pneumatic Motor	High power density; Easy to be fabricated with 3D printer; Inexpensive.	System delay; High noise.

According to design specifications of selection requirements of the driving system, the piezoelectric ceramic motor is chosen as the drive unit for each joint of the robot manipulator to satisfy MRI safe/conditional requirements. Once the motor is determined, the next step is to determine joint specifications of the robot according to TM.13 modular design. Considering



that the torque of piezoelectric ceramic motors is less than that of traditional stepping motors, the solution of installing a harmonic reducer is proposed to compensate for the insufficient torque of piezoelectric ceramic motors. Figure 3-7 shows the proposed structure of each joint.

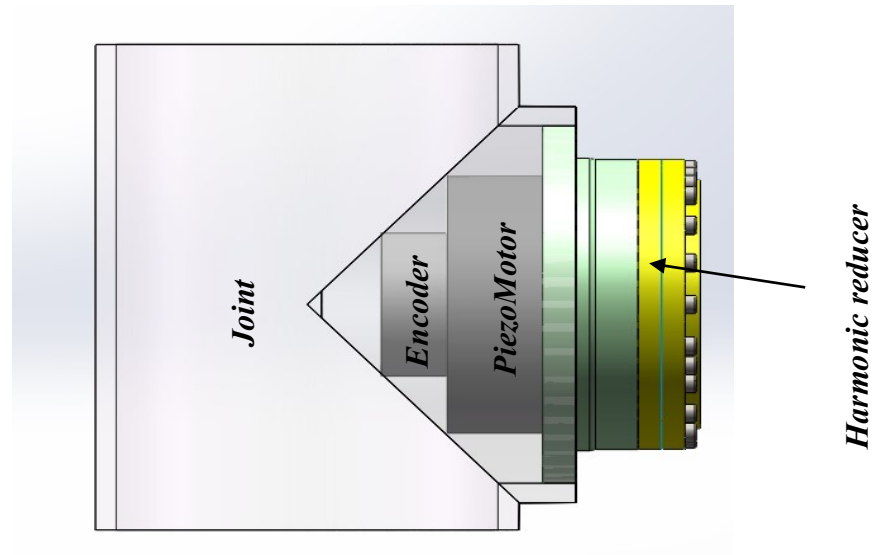


*Figure 3–7 Transmission mechanism: Encoder, motor, harmonic reducer*

Non-magnetic piezoelectric actuators are used to drive the mechanism of each joint. These actuators are available in the market, such as Nanomotion motors (Nanomotion Ltd., Israel), Shinsei motors (Shinsei Corporation, Japan), and PiezoLegs motors (PiezoMotor AB, Sweden), etc. Since the maximum torque of the motor Shinsei motor is 1.0Nm, which is greater than that of other companies, the USED 60-E series Shinsei motor is selected in this study. Furthermore, it provides the encoder with 1000p/r for using to measure the angle speed of each joint to ensure the measurement accuracy and reduce signal transmission time from the motor to personal computer. Figure 3-8 shows the connection method with the Shinsei motor.

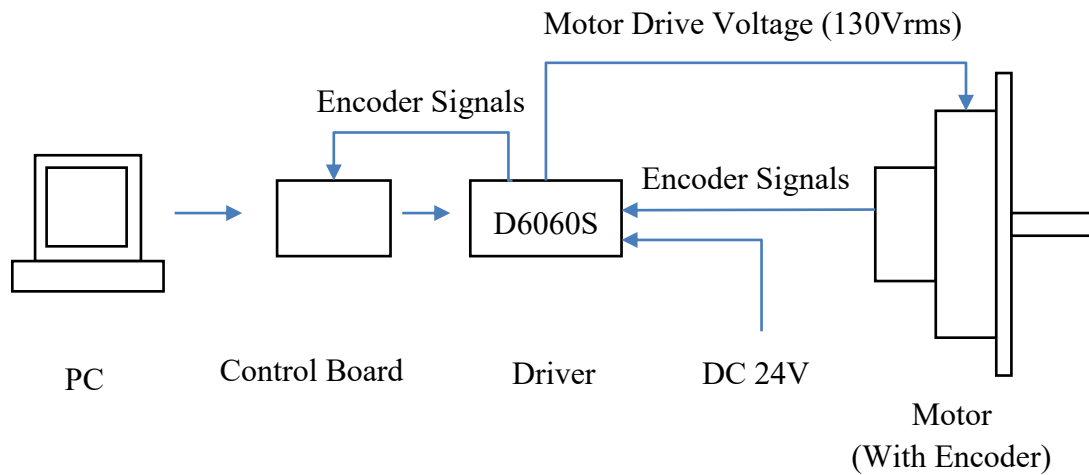


*Figure 3–8 Connection Method with Shinsei Motor Flowchart*

Commonly used speed changes on industrial robots include the gear drive, belt drive, worm gear drive, and harmonic reducer. Due to its small size, lightweight, and other characteristics, harmonic reducers are used in the end joints of robots. In addition, the production can be processed through customized non-magnetic material solutions for the MRI compatibility.

According to the analysis of MRI material compatibility requirements, in order not to reduce impact on imaging effects of the MRI imaging equipment by the selected material, the material of PEEK, POM and 304 stainless steel are chosen for the mechanical structure of the robot manipulator design. By comparing with other MRI-compatible engineering plastics, such as ABB, epoxy, and fluoroplastics, POM and PEEK have been widely used in many fields due to their superior performance, such as medical fields, agricultural fields, and instrumentation industries [67][68]. Specifically, their mechanical characteristics are very similar to iron and steel, that is, they have strong strength and rigidity. In addition, its better tensile strength and bending strength lead to less deformation to ensure the overall rigidity and reliability of the robot manipulator. Figure 3-9 illustrates the definition of the final product.

### 3.3.5. Result and comparison

The proposed model of the MRI-guided robot is generated based on the selected key components and designed parts. The design specifications in HoQ is partially considered in the conceptual development process due to the incapable of concept generations in the QFD method. Table 3-7 shows the comparison with competitors' robots in terms of the most important CRs, namely, the size, weight, and MR safe/conditional. Finally, the appearance of the 3D model is proposed as shown in Fig. 3-9.

*Table 3-7 Comparison with benchmarking robots*

Product	Total size	Total mass	Degree of freedoms	Actuator & materials
Cirq robot	850mm	11kg	6 DOF	MR unsafe
ROSA robot	1050mm	21kg	6 DOF	MR unsafe
NeuroArm robot	910mm	18kg	7 DOF (1 DOF for automatic needle insertion)	MR safe
SCHERI robot (ours)	738mm	9.87kg	6 DOF (Manual insertion of end-effectors (needle/catheter))	MR safe/conditional

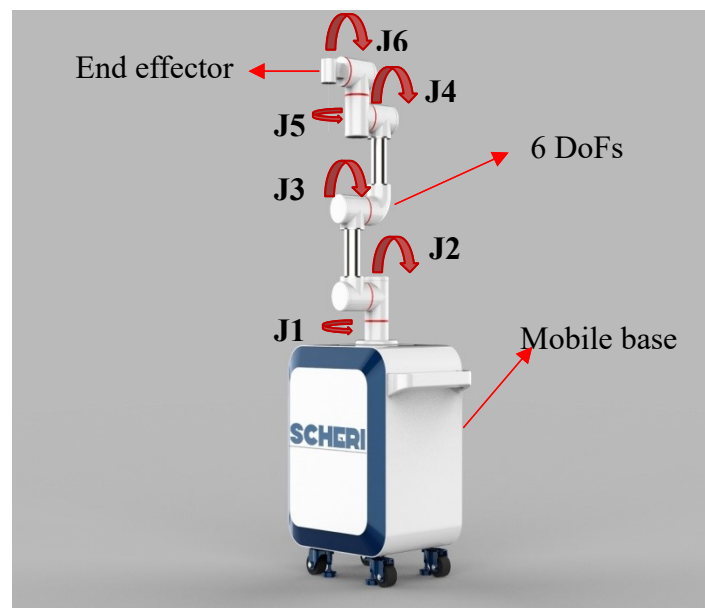


*Figure 3–9 Concept of the MRI-guided robot*

### 3.4. Summary

In this chapter, the QFD method is used to translate customer requirements into technical metrics for the MRI-guided robot design. Three benchmarking surgical robots that are the most commonly applied in neurosurgical operations are referred as benchmarks for the generation of design target values of the MRI-guided robot. All the information is summarized in a HoQ to guide the MRI-guided robot design. According to results of the HoQ, key components and technical metrics, such as the motor type, selection of materials, degree of freedoms, and total size, are determined, and the final robotic structure and 3D model are developed.

# Chapter 4. Kinematics analysis and trajectory planning for MRI-guided robot manipulator

## 4.1. Introduction

The proposed MRI-guided robot is used for guiding the needle/catheter insertion during stereotactic neurosurgical procedures, which requires the high operating safety and accurate positioning. One of the factors impacting the positioning accuracy is the kinematic model of the robot, which describes the robotic geometry in the parametric form. In addition, one of the most important customer requirements is related to the safety of neurosurgical procedures. Since the robot moves around patient's head, it is necessary to determine trajectory planning strategies and control parameters such as displacement, velocity, and acceleration of the robotic end-effector.

This chapter is organized as follows. Section 4.2 is a brief introduction to robot kinematics and D-H parameters. Section 4.3 develops forward and inverse kinematic models for the proposed MRI-guided robot, and uses the simulation to verify the kinematic model. Section 4.4 proposes a trajectory planning strategy for the MRI-guided robot for the stereotactic neurosurgery based on the different spatial trajectory planning algorithms. Section 4.5 is the trajectory planning simulation and result analysis based on the MATLAB software. The chapter is summarized in Section 4.6.

## 4.2. Robotic kinematics

### 4.2.1. Description of position

The position of a point in the 3D space can be described by a  $3 \times 1$  vector. As shown in Figure 4-1, the position of any point P in a coordinate system {O} can be described as follows.

$$P = \begin{bmatrix} P_x \\ P_y \\ P_z \end{bmatrix} \quad (4-1)$$

where  $P_x$ ,  $P_y$ , and  $P_z$  are projections of the position vector of point P on three coordinate axes of  $\{O\}$ , respectively.

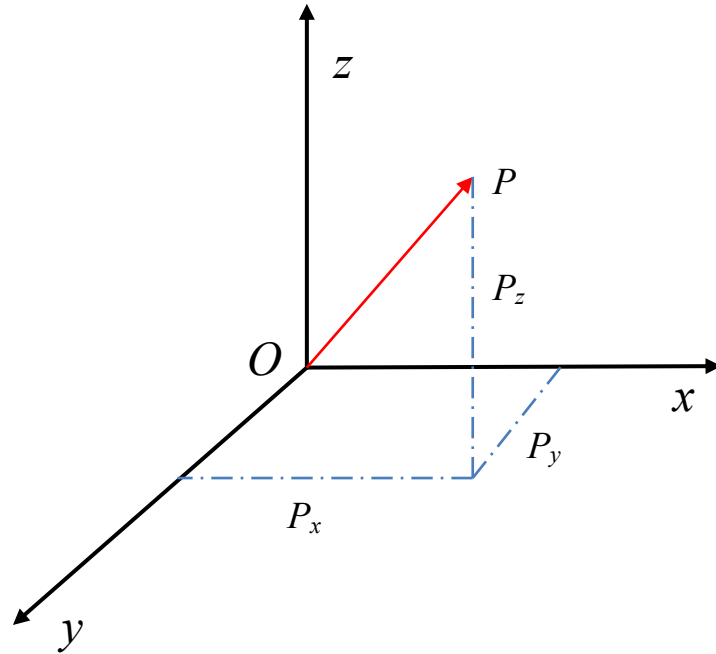


*Figure 4-1 Spatial point coordinates*

#### 4.2.2. Description of pose

As shown in Figure 4-2, a spatially moving coordinate system  $\{O'\}$  is used to represent the posture of a rigid body whose axes are  $X'$ ,  $Y'$ , and  $Z'$ , respectively. The moving coordinate system  $\{O'\}$  has an angular rotation with respect to the world coordinate system  $\{O\}$  in the Figure 4-2.

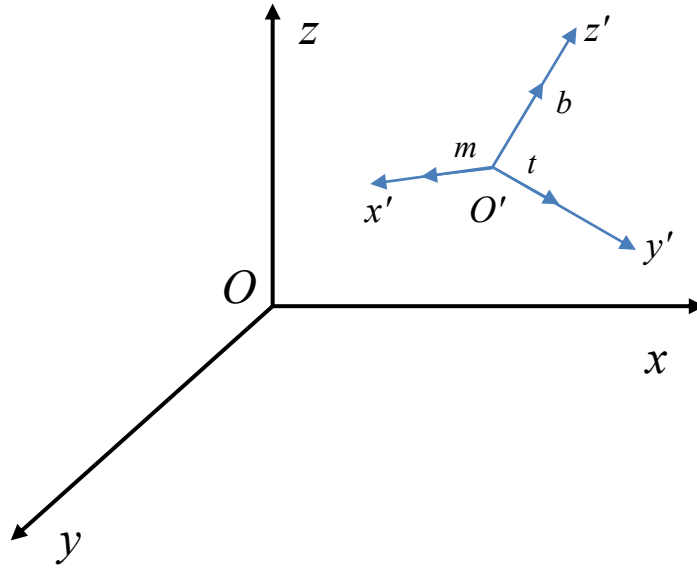


Figure 4-2 Coordinate vector transformations of poses

Where,  $m$ ,  $t$ , and  $b$  are unit vectors along  $X'$ ,  $Y'$ , and  $Z'$  axes, respectively. Figure 4-2 shows that these vectors have this angle in each axis of the world coordinate system  $\{O\}$ , and the pose can be described by cosine angles formed by these vector values in the plane projection line of the coordinate system  $\{O\}$ , respectively. The rotation matrix  $R$  describes the posture of the rigid body with respect to the world coordinate system as follows:

$$R = \begin{bmatrix} \cos(\angle X' X) & \cos(\angle Y' X) & \cos(\angle Z' X) \\ \cos(\angle X' Y) & \cos(\angle Y' Y) & \cos(\angle Z' Y) \\ \cos(\angle X' Z) & \cos(\angle Y' Z) & \cos(\angle Z' Z) \end{bmatrix} \quad (4-2)$$

In the robotic kinematics, the transformation between multiple coordinate systems is often expressed using homogeneous transformation matrix  $T$  shown in Eq. 4-3.

$$T = \begin{bmatrix} R & P \\ 0 & 1 \end{bmatrix} \quad (4-3)$$

Where,  $R$  is the posture of the rigid body and  $P$  is the position of the rigid body.

### 4.2.3. Denavit–Hartenberg (D–H) parameters

According to the conceptual design in Chapter 3, the proposed MRI-guided robot is a 6 DOFs serial manipulator consisting of a base, linkage, joint and end-effector. In order to establish the kinematic relationship between the end-effector and each joint variable, it is necessary to establish local coordinate systems on each of the components that have relative motions each other, and build the posture relationship between these coordinate systems. The D-H method is a general method for establishing local coordinate systems for components of serial robots, as shown in Figure 4-3.

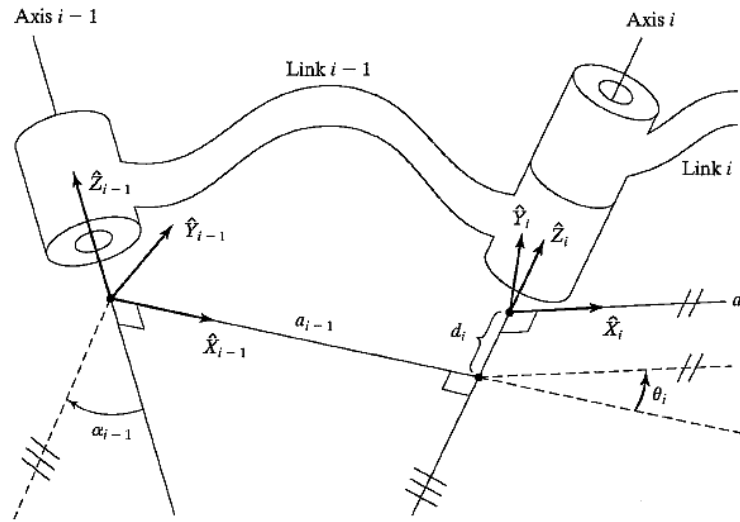


Figure 4–3 Denavit–Hartenberg kinematic parameters

Based on Figure 4-3, there are four transformation parameters to describe coordinates from one link to the next in D-H parameters as follows.

- 1) Joint angle  $\theta_i$ : Angle between  $X_{i-1}$  and  $X_i$  measured for  $Z_{i-1}$ ;
- 2) Twist angle  $\alpha_i$ : Angle between  $Z_{i-1}$  and  $Z_i$  measured for  $X_i$ ;
- 3) Link offset  $d_i$ : Distance from  $X_{i-1}$  to  $X_i$  measured along  $Z_{i-1}$ ;
- 4) Link length  $a_i$ : Distance from  $Z_{i-1}$  to  $Z_i$  measured along  $X_i$ .

The D-H transformation matrix consists of 4 major parts, namely, the rotation matrix (R), position matrix (P), zero matrix (0), and proportional transformation (I). According to Eq. (4-



3), transformation matrix  $T$  can be further expressed as follows.

$$T = \begin{bmatrix} n_x & o_x & a_x & P_x \\ n_y & o_y & a_y & P_y \\ n_z & o_z & a_z & P_z \\ 0 & 0 & 0 & 1 \end{bmatrix} \quad (4-4)$$

where,  $P = [P_x \ P_y \ P_z]^T$  is a position matrix,  $R = \begin{bmatrix} n_x & o_x & a_x \\ n_y & o_y & a_y \\ n_z & o_z & a_z \end{bmatrix}$  is the rotation matrix.

$n = [n_x \ n_y \ n_z]^T$ ,  $o = [o_x \ o_y \ o_z]^T$ ,  $a = [a_x \ a_y \ a_z]^T$ . According to Section 4.2.2, matrix  $n$  is the direction cosine of unit vector  $m$  with respect to world coordinate system  $\{O\}$ ; matrix  $o$  is the direction cosine of unit vector  $t$  with respect to world coordinate system  $\{O\}$ ; matrix  $a$  is the direction cosine of unit vector  $b$  with respect to world coordinate system  $\{O\}$ ; and  $P$  is the position vector of the vector  $OP$  with respect to world coordinate system  $\{O\}$ .

Using the D-H parameter method, the robotic transformation matrix  ${}^{i-1}_iT$  can be expressed as follows.

$${}^{i-1}_iT = \begin{bmatrix} n_x & o_x & a_x & P_x \\ n_y & o_y & a_y & P_y \\ n_z & o_z & a_z & P_z \\ 0 & 0 & 0 & 1 \end{bmatrix} = \begin{bmatrix} \cos\theta_i & -\sin\theta_i \cdot \cos\alpha_i & \sin\theta_i \cdot \sin\alpha_i & a_i \cdot \cos\theta_i \\ \sin\theta_i & \cos\theta_i \cdot \cos\alpha_i & -\cos\theta_i \cdot \sin\alpha_i & a_i \cdot \sin\theta_i \\ 0 & \sin\alpha_i & \cos\alpha_i & d_i \\ 0 & 0 & 0 & 1 \end{bmatrix} \quad (4-5)$$

Therefore, a general transformation between the end effector and robot base can be derived as:

$${}^0_6T = {}^0_1T * {}^1_2T * {}^2_3T * {}^3_4T * {}^4_5T * {}^5_6T \quad (4-6)$$

### 4.3. Detailed kinematic modeling of the MRI-guided robot

The proposed MRI-guided robot is a manipulator with 6 DOF, and the all 6 joints are rotating joints. Figure 4-4 illustrates a 3D model of the MRI-guide robot manipulator in the initial pose.

Each link's coordinate system of the MRI-guided robot is established according to Figure 4-3, as shown in Figure 4-5.

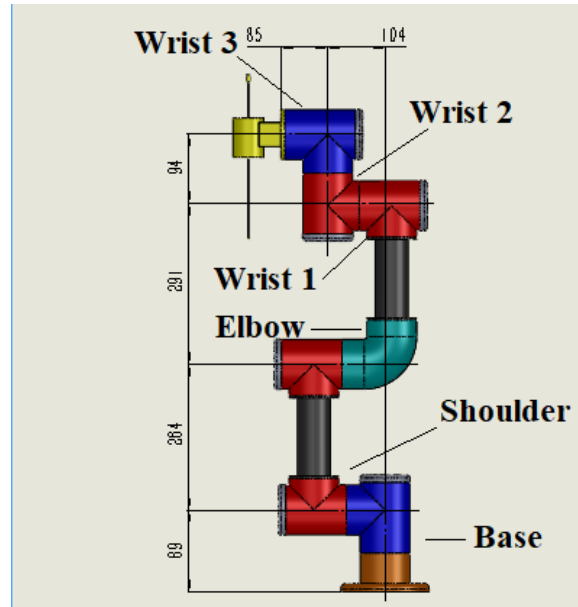


Figure 4–4 3D model and dimensions of proposed MRI-guided robot manipulator

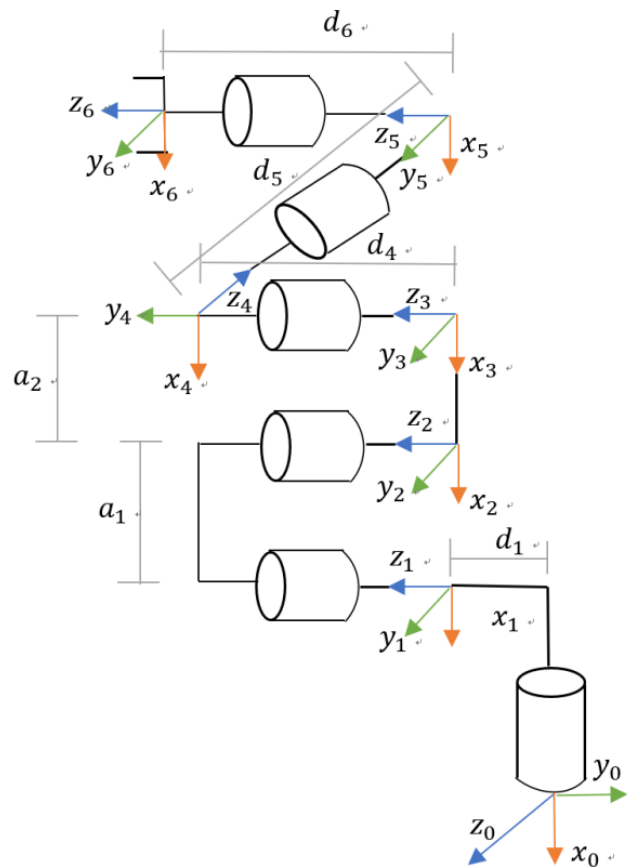


Figure 4–5 MRI-guided robotic manipulator coordinate system for each joint

Finally, the MRI-guided robot D-H parameters can be decided as listed in Table 4-1, where  $i = 1, 2, \dots, 6$  is the number of links. Table 4-2 illustrates constant values of D-H parameters for the MRI-guided robot.

*Table 4-1 D-H Parameter of MRI-guided robot*

$i$	$a_{i-1}(\text{mm})$	$d_i(\text{mm})$	$\alpha_{i-1}(\text{rad})$	$\theta_i(\text{rad})$
1	0	$d_1$	$90^\circ$	$\theta_1$
2	$a_1$	0	$0^\circ$	$\theta_2$
3	$a_2$	0	$0^\circ$	$\theta_3$
4	0	$d_4$	$90^\circ$	$\theta_4$
5	0	$d_5$	$-90^\circ$	$\theta_5$
6	0	$d_6$	$0^\circ$	$\theta_6$

*Table 4-2 Constant values of D-H parameters*

D-H parameter	$d_1$	$a_1$	$a_2$	$d_4$	$d_5$	$d_6$
Values (mm)	69	264	291	104	94	85

#### 4.3.1. Forward kinematic modeling

The MRI-guided robot manipulator relies on the movement of the end effector (needle/catheter) to perform positioning tasks in the neurosurgical procedure. The position and posture of the end effector are determined by each joint angle of the manipulator. The robotic forward kinematic decides the motion transfer relationship between the joint space and task space, i.e., the robot end effector position and posture are decided according to the each linkage length and each joint angle.

According to Eq. (4-5) and D-H parameters in Table 4-1, the  ${}^{i-1}_iT$  matrix of the MRI-guided robotic manipulator for each joint can be described as follows:

$$\begin{aligned}
{}^0_1T &= \begin{bmatrix} \cos\theta_1 & 0 & \sin\theta_1 & 0 \\ \sin\theta_1 & 0 & -\cos\theta_1 & 0 \\ 0 & 1 & 0 & d_1 \\ 0 & 0 & 0 & 1 \end{bmatrix} \\
{}^1_2T &= \begin{bmatrix} \cos\theta_2 & -\sin\theta_2 & 0 & a_2\cos\theta_2 \\ \sin\theta_2 & \cos\theta_2 & 0 & a_2\sin\theta_2 \\ 0 & 0 & 1 & 0 \\ 0 & 0 & 0 & 1 \end{bmatrix} \\
{}^2_3T &= \begin{bmatrix} \cos\theta_3 & -\sin\theta_3 & 0 & a_3\cos\theta_3 \\ \sin\theta_3 & \cos\theta_3 & 0 & a_3\sin\theta_3 \\ 0 & 0 & 1 & 0 \\ 0 & 0 & 0 & 1 \end{bmatrix} \\
{}^3_4T &= \begin{bmatrix} \cos\theta_4 & 0 & \sin\theta_4 & 0 \\ \sin\theta_4 & 0 & -\cos\theta_4 & 0 \\ 0 & 1 & 0 & d_4 \\ 0 & 0 & 0 & 1 \end{bmatrix} \\
{}^4_5T &= \begin{bmatrix} \cos\theta_5 & 0 & -\sin\theta_5 & 0 \\ \sin\theta_5 & 0 & \cos\theta_5 & 0 \\ 0 & -1 & 0 & d_5 \\ 0 & 0 & 0 & 1 \end{bmatrix} \\
{}^5_6T &= \begin{bmatrix} \cos\theta_6 & -\sin\theta_6 & 0 & 0 \\ \sin\theta_6 & \cos\theta_6 & 0 & 0 \\ 0 & 0 & 1 & d_6 \\ 0 & 0 & 0 & 1 \end{bmatrix}
\end{aligned} \tag{4-6}$$

According to Eq. (4-6), the end effector matrix  ${}^0_6T$  can be obtained by substituting the D-H parameters in Table 4-1 into the above matrices as follows:

$${}^0_6T = {}^0_1T * {}^1_2T * {}^2_3T * {}^3_4T * {}^4_5T * {}^5_6T = \begin{bmatrix} n_x & o_x & a_x & P_x \\ n_y & o_y & a_y & P_y \\ n_z & o_z & a_z & P_z \\ 0 & 0 & 0 & 1 \end{bmatrix} \tag{4-7}$$

where,

$$\begin{aligned}
n_x &= -s_6c_1s_{234} + s_1s_5c_6 + c_1c_5c_6c_{234}; \\
n_y &= s_1c_{234}c_5c_6 - s_5c_1c_6 - s_1s_{234}s_6 \\
n_z &= s_{234}c_5c_6 + s_6c_{234}; \\
o_x &= -s_1s_5s_6 - c_1c_{234}c_5c_6 - c_1c_6s_{234}; \\
o_y &= -s_1s_6c_{234}c_5 + s_5s_6c_1 - s_1s_{234}c_6; \\
o_z &= c_{234}c_6 - s_{234}s_6c_5; \\
a_x &= s_1c_5 - s_5c_1c_{234};
\end{aligned} \tag{4-8}$$

$$a_y = -s_1 s_5 c_{234} - c_1 c_5;$$

$$a_z = -s_{234} s_5;$$

$$P_x = d_4 s_1 + d_5 c_1 s_{234} - a_2 c_1 c_2 + d_6 c_5 s_1 + a_3 c_1 c_{23};$$

$$P_y = -d_4 c_1 + d_5 s_1 s_{234} - d_6 s_1 s_5 c_{234} - d_6 c_1 c_5 + a_2 s_1 c_2 + a_3 s_1 c_{23};$$

$$P_z = -d_5 c_{234} + a_2 s_2 - d_6 s_{234} s_5 + a_5 s_{23} + d_6.$$

where,  $s_i = \sin \theta_i$ ,  $c_i = \cos \theta_i$ ,  $s_{23} = \sin(\theta_2 + \theta_3)$ ;  $c_{23} = \cos(\theta_2 + \theta_3)$ ;  $s_{234} = \sin(\theta_2 + \theta_3 + \theta_4)$ ;  $c_{234} = \cos(\theta_2 + \theta_3 + \theta_4)$ . As a result, the position and posture of the end-effector of the manipulator with respect to the base can be obtained if variable  $\theta_i (i = 1, 2, \dots, 6)$  is given based on Eq. (4-7).

#### 4.3.2. Inverse kinematic modeling

Inverse kinematic analysis is the opposite of the forward kinematic analysis. The corresponding variables of each joint can be found based on the given location requirement of the end of the manipulator in the given reference coordinates system. Furthermore, it is also the basis for trajectory planning and motion control. Generally, there are two main approaches to solve the robot inverse kinematics: analytical and numerical approaches. From the previous chapter, it can be known that the proposed MRI-guided robot satisfies the Pieper criterion, which means that there is the closed analytical solution for the robot. In this section, the inverse solution of the robotic kinematics is decided using the analytical approach based on results of the forward kinematics.

Multiplying matrix  ${}^0T$  left by matrix  ${}^0T^{-1}$  and right by matrix  ${}^5T^{-1}$  gives:

$${}^0T^{-1} {}^0T {}^5T^{-1} = \begin{bmatrix} c_1 & s_1 & 0 & 0 \\ 0 & 0 & 1 & 0 \\ s_1 & -c_1 & 0 & -d_1 \\ 0 & 0 & 0 & 1 \end{bmatrix} \begin{bmatrix} n_x & o_x & a_x & P_x \\ n_y & o_y & a_y & P_y \\ n_z & o_z & a_z & P_z \\ 0 & 0 & 0 & 1 \end{bmatrix} \begin{bmatrix} c_6 & s_6 & 0 & 0 \\ -s_6 & c_6 & 0 & 0 \\ 0 & 0 & 1 & -d_6 \\ 0 & 0 & 0 & 1 \end{bmatrix} \quad (4-9)$$

Since elements in the 3rd row and 4th column on the left and right sides of Eq. (4-9) are

equal, which gives:

$$s_1(P_x - d_6 a_x) - c_1(P_y - d_6 a_y) = d_4 \quad (4-10)$$

Performing trigonometric function on Eq. (4-10), which gives:

$$\theta_1 = \arctan\left(\frac{P_y - d_6 a_y}{P_x - d_6 a_x}\right) \pm \arccos\left(\frac{d_4}{r}\right) \quad (4-11)$$

where  $r$  is as follows:

$$r = \sqrt{(P_x - d_6 a_x)^2 + (P_y - d_6 a_y)^2} \quad (4-12)$$

Multiplying matrix  ${}^0T$  left by matrix  ${}^0T^{-1}$  gives:

$${}^0T^{-1} \cdot {}^0T = \begin{bmatrix} c_1 & s_1 & 0 & 0 \\ 0 & 0 & 1 & 0 \\ s_1 & -c_1 & 0 & -d_1 \\ 0 & 0 & 0 & 1 \end{bmatrix} \begin{bmatrix} n_x & o_x & a_x & P_x \\ n_y & o_y & a_y & P_y \\ n_z & o_z & a_z & P_z \\ 0 & 0 & 0 & 1 \end{bmatrix} \quad (4-13)$$

Since elements in the 3rd row and 4th column on either side of Eq. (4-13) are equal, which gives:

$$s_1 P_x - c_1 P_y = d_6 c_5 + d_4 \quad (4-14)$$

Simplifying Eq. (4-14) gives:

$$\theta_5 = \pm \arccos\left(\frac{s_1 P_x - c_1 P_y - d_4}{d_6}\right) \quad (4-15)$$

Since elements in the 3rd row and 1st column on the left and right sides of Eq. (4-13) and elements in the 3rd row and 2nd column are equal, which gives:

$$s_1 n_x - c_1 n_y = -s_6 s_5 \quad (4-16)$$

$$-s_1 o_x + c_1 o_y = c_6 s_5 \quad (4-17)$$

Combining Eq. (4-16) and Eq. (4-17) gives:

$$\theta_6 = \pm \arccos\left(\frac{-s_1 o_x + c_1 o_y}{s_1 n_x - c_1 n_y}\right) \quad (4-18)$$

Since elements in the 1st row and 3rd column on left and right sides of Equation (4-9) and elements in the 2nd row and 3rd column are equal, which gives:

$$-(c_1 a_x + s_1 a_y) = s_5 c_{234} \quad (4-19)$$

$$a_z = -s_5 s_{234} \quad (4-20)$$

Combining Equations (4-19) and (4-20) gives:

$$\theta_{234} = \arccos\left(\frac{a_z}{c_1 a_x + s_1 a_y}\right) \quad (4-21)$$

Since elements in the 1st row and 4th column on left and right sides of Equation (4-13) and elements in the 2nd row and 4th column are equal, which gives:

$$-d_6(c_1 a_x + s_1 a_y) + c_1 P_x + s_1 P_y = a_2 c_2 + a_3 c_{23} + d_5 s_{234} \quad (4-22)$$

$$-d_6 a_z + P_z - d_1 = a_2 s_2 + a_3 s_{23} - d_5 c_{234} \quad (4-23)$$

Combining Equations (4-22) and (4-23), and eliminating variable  $\theta_{23}$  (i.e.  $\theta_2 + \theta_3$ ) give:

$$(m_1 - a_2 c_2)^2 + (m_2 - a_2 s_2)^2 = a_3^2 \quad (4-24)$$

where,  $m_1$  and  $m_2$  are indicated as follows:

$$m_1 = -d_6(c_1 a_x + s_1 a_y) + c_1 P_x + s_1 P_y - d_5 s_{234} \quad (4-25)$$

$$m_2 = -d_6 a_z + P_z + d_5 c_{234} - d_1 \quad (4-26)$$

Then, variable  $\theta_2$  can be obtained as follows:

$$\theta_2 = \arccos\left(\frac{m_1^2 + m_2^2 + a_2^2 - a_3^2}{\sqrt{(2 \times a_2 \times m_1)^2 + (2 \times a_2 \times m_2)^2}}\right) + \arctan\left(\frac{m_2}{m_1}\right) \quad (4-27)$$

Combining Equations (4-22) and (4-23) gives:

$$\theta_{23} = \arctan\left(\frac{-d_6 a_z + P_z - d_1 + d_5 c_{234} + a_3 s_2}{-d_6(c_1 a_x + s_1 a_y) + c_1 P_y + s_1 P_x - d_5 s_{234} + a_3 s_2}\right) \quad (4-28)$$

Then, the variables  $\theta_4$  and  $\theta_3$  can be obtained:

$$\theta_4 = \theta_{234} - \theta_{23} \quad (4-29)$$

$$\theta_3 = \theta_{23} - \theta_2 \quad (4-30)$$

Finally, six joint variables of the MRI-guided manipulator from  $\theta_1$  to  $\theta_6$  can be decided. Since joint variables  $\theta_1$ ,  $\theta_5$ , and  $\theta_6$  have two solutions, the proposed MRI-guided robot manipulator has a total of eight sets of inverse solutions.

### 4.3.3. Kinematics verification and results

In this section, both forward kinematics and inverse kinematics are validated using the MATLAB 2019b and robot toolbox. Firstly, the robot manipulator is viewed as a linkage consisting of a series of joints in the simulation. The robot function in MATLAB is used to connect individual links and joints for the robot manipulator. The plot function is then used to create a 3D model of the robot, as shown in Figure 4-6.

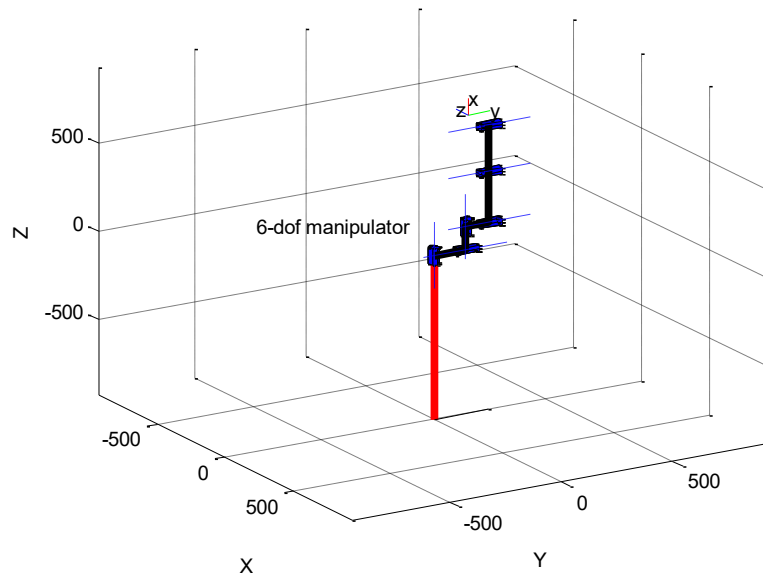


*Figure 4–6 3D model of the robot manipulator based on MATLAB*

Forward kinematics is the angle of each joint of the robot known to determine the position and posture of the end-effector. According to Figure 4-6, the initial value of each joint variable is  $[0, 0, 0, 0, 0, 0]$ . Matrix  $T$  can be obtained by using the `fkine()` function in the MATLAB Robotics Toolbox, and invoking the Link function:

$$T = \begin{bmatrix} 1 & 0 & 0 & -1055.0000 \\ 0 & 0 & 1 & 24.6700 \\ 0 & -1 & 0 & -188.9300 \\ 0 & 0 & 0 & 1 \end{bmatrix} \quad (4-31)$$

Similarly, by substituting the initial joint angle values into Equation (4-7), the initial posture matrix  ${}^0T$  of the end-effector can be decided as follows.



$${}^0_6T = \begin{bmatrix} 1 & 0 & 0 & -1055 \\ 0 & 0 & 1 & 25 \\ 0 & -1 & 0 & -189 \\ 0 & 0 & 0 & 1 \end{bmatrix} \quad (4-32)$$

As a result, it proves that the forward kinematics model is correct since Equations (4-31) and (4-32) are equal.

In order to validate the developed inverse kinematics model for the MRI-guided robot manipulator, the `ikine()` function is utilized in MATLAB Robotics Toolbox. All possible inverse solutions are solved by the inverse kinematics using the posture matrix calculated from random joint angles in the kinematic positive solution. If the inverse solution has a relevant angle value, the correctness of the inverse kinematics can be verified. Here, the joint angle value is  $[90, -90, 45, -90, 45, 45]$ . Matrix  ${}^0_6T$  can be decided by the forward kinematics as follows.

$${}^0_6T = \begin{bmatrix} 0.50 & -0.50 & 0.71 & 167.45 \\ 0.15 & 0.85 & 0.50 & 302.94 \\ -0.85 & -0.15 & 0.50 & 599.64 \\ 0 & 0 & 0 & 1 \end{bmatrix} \quad (4-33)$$

Then, all the inverse solutions  $\theta_i$  can be obtained using Equation (4-33), as shown in Table 4-3.

From Table 4-3, it shows that joint angle values in the first group are equal to the given angle values. From the inverse kinematic analysis, it is known that the proposed robot manipulator has eight sets of inverse solutions. Since two sets of inverse solutions are equal in all inverse solutions of the simulation, six sets of inverse solutions are finally obtained. Therefore, it also proves that the inverse kinematics model is correct.

*Table 4-3 Inverse solutions for robotic manipulator*

	$\theta_1$	$\theta_2$	$\theta_3$	$\theta_4$	$\theta_5$	$\theta_6$
1	90	-90	45	-90	45	45
2	90	-45	-45	-45	45	45
3	90	-60	0	108	-45	-135
4	-55	-120	0	30	150	170
5	-55	-115	165	-170	-150	30
6	-55	-100	-165	-155	-150	-30

#### 4.4. Trajectory planning of MRI-guided robot

Based on the clinical safety and operation stability, different strategies of trajectory planning are proposed for preventing collisions between the robot and patient head as well as reducing vibrations during the movement, considering the environment in the operating room and the stereotactic neurosurgical procedures. First of all, due to the fact that the robot usually vibrates because of the acceleration and deceleration during the positioning process on interventional operations, which results in a low positioning accuracy. In addition, the stereotactic neurosurgery is performed on the patient head, which possibly results in potential risks when the robot end effector (i.e., needle/catheter) is getting close to the patient head and skin. Therefore, the intervention and movement of the robot need to be extreme delicate and precise to ensure that there is no injury to the patient when the robot end effector arrives at the desired posture. As a result, trajectory planning strategies need to be pre-considered when programming the robot. In this section, a sectioned trajectory planning approach is introduced for simulation of the robot movement during surgery.

#### 4.4.1. Trajectory planning for the stereotactic neurosurgery

Since the stereotactic neurosurgery is aimed at targeting and treating diseases affecting deep structures of the brain, such as the deep brain stimulation through stereotactic micro-electrode placement and brain tumor ablation through thermal ablators, the procedure relies on the high safety and positioning accuracy [41]. As shown in Figure 4-7, the first step of the workflow is to scan the patient using an MRI scanner to obtain a 3D medical image of the targeting in the deep brain. Secondly, the skin entry point, the target point and surgical planning path are identified through the surgical planning software (as shown in Figure 4-8), while the neurosurgeon will be given the desired position and pose of the robotic end-effector (i.e., needle/catheter) insertion. Finally, the robot will move and position automatically after solving the inverse kinematics problem.

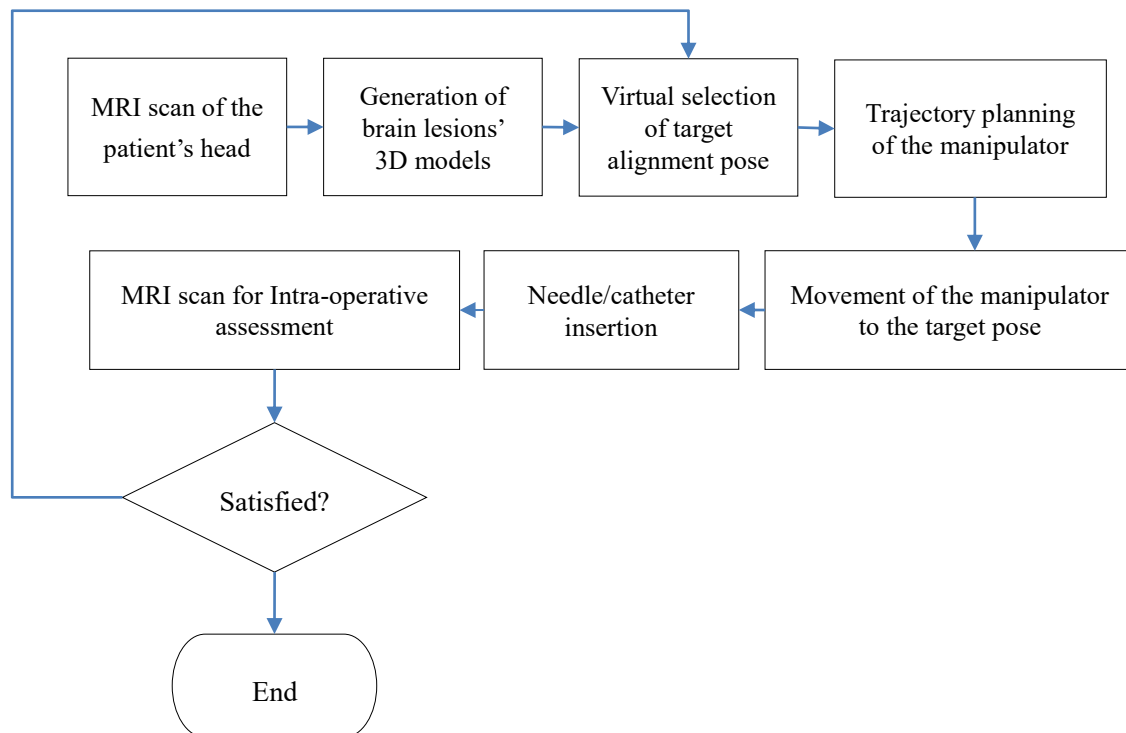


*Figure 4–7 Workflow of the stereotactic neurosurgery for trajectory planning*

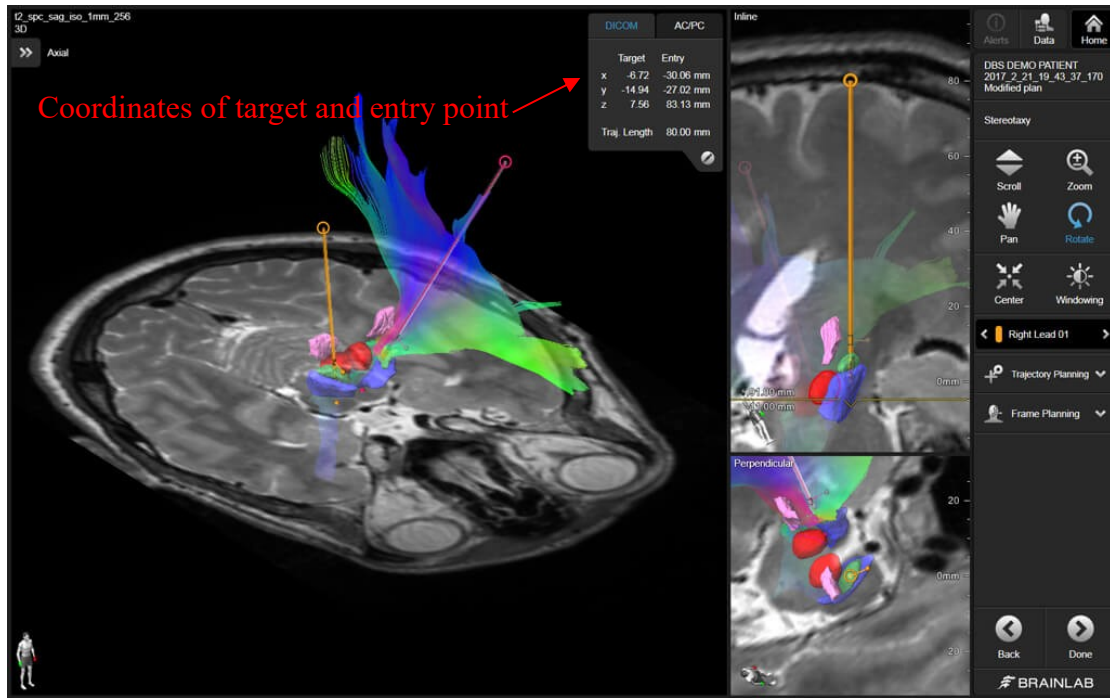


Figure 4–8 Surgical path planning using 3D image software [69]

In this research, the proposed MRI-guided robot is a shared control system according to results of the analysis of customer requirements, i.e., the surgeon will manually insert and move the needle/catheter after the robot end-effector is automatically positioned. Once the surgical task is completed, the patient will be sent back into the MRI scanner for scanning again and the surgeon will decide when the desired outcome has been achieved.

Generally, the path is described geometrically as the motion, i.e., expressed as a trajectory of points in the joint space or operating space for the robot. On the other hand, the trajectory is represented as a time series specified on that path, e.g., the velocity or acceleration of each point. There are two kinds of the trajectory planning strategy, which are joint space trajectory planning and task space trajectory planning, respectively. When trajectory planning is performed in a joint space, the robot path is unpredictable, and the fast travel from start point A to end point B based on the time optimization or shortest path. When trajectory planning is performed in the task space, the robot path is usually given, such as a straight line or a circular arc, and its end-effectors follow a specified path in a slow motion. Table 4-4 presents a comparison of different trajectory planning strategies.

*Table 4-4 Comparison of planning based on different spatial trajectories*

	Task Space	Joint Space
Pros	a) Trajectory is predictable; b) Be Better handling of obstacles and collisions.	a) Faster execution; b) Easy to calculate;
Cons	a) Slower execution; b) Calculation is cumbersome.	a) Intermediate points not guaranteed to respect joint limits and collisions; b) The trajectory is unpredictable.

Therefore, according to above advantages of different trajectory planning strategies, free and restricted areas are proposed for robotic positioning in stereotactic neurosurgical procedures, respectively. Where, the robot can move fast and freely without constrains, which is defined as a free area, and the robot end effector slowly approaches the surgical area (i.e. patient head) along a straight line, which is defined as the restricted area, which is shown in Figure 4-9. The restricted area is the space around the patient head. Since the Radiofrequency (RF) coil and Head Fixed Device (HFD) are in the imaging area of the MRI, this imaging area is considered the restricted area. In this area, the robot will be programmed so that it slowly approaches the surgical area (i.e., the entry point) along a linear path. The free area is located outside the restricted area and its manipulator movement is not restricted.

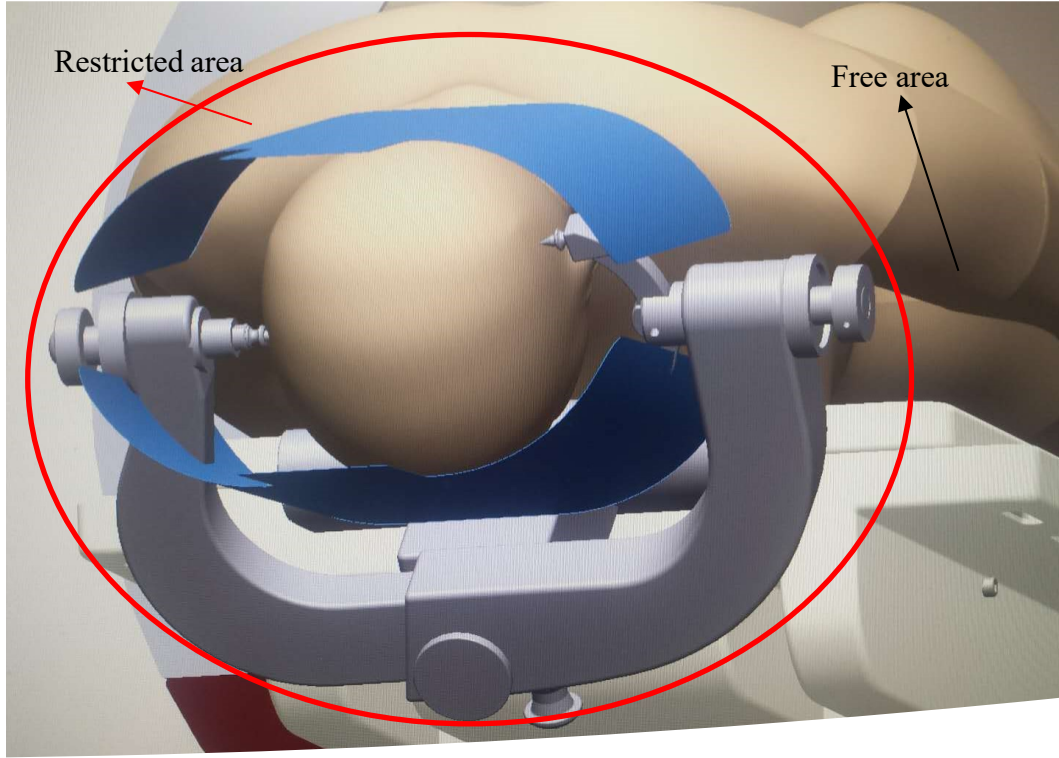


*Figure 4-9 Defining the free area and restricted area*

#### 4.4.2. Trajectory planning in the joint space

In the free area, the joint space trajectory planning is utilized. Joint space trajectory planning decides the position, velocity, and acceleration over time under satisfying some constraints. Smooth and continuous joint variable functions can be obtained directly using some polynomial interpolation algorithms (e.g., three polynomial functions, five polynomial functions). According to literature [70], the five polynomial functions algorithm is able to give constraints on the acceleration of the manipulator and to eliminate acceleration discontinuities, which results in a smoother motion of the manipulator. Therefore, the five polynomial functions algorithm is utilized for joint space trajectory planning in the unrestricted zone.

Generally, there are six parameters that need to be determined in the five polynomial functions, namely, angular displacement  $\theta$ , angular velocity  $\dot{\theta}$ , and angular acceleration  $\ddot{\theta}$  for both end and beginning points, where, angular displacement  $\theta$  is a function of the joint variable over time, and its first-order and second-order derivatives over time are angular velocity  $\dot{\theta}$  and

angular acceleration  $\ddot{\theta}$ , respectively. The general formulas of them are as follows.

$$\theta(t) = a_0 + a_1t + a_2t^2 + a_3t^3 + a_4t^4 + a_5t^5 \quad (4-34)$$

$$\dot{\theta}(t) = a_1 + 2a_2t + 3a_3t^2 + 4a_4t^3 + 5a_5t^4 \quad (4-35)$$

$$\ddot{\theta}(t) = 2a_2 + 6a_3t + 12a_4t^2 + 20a_5t^3 \quad (4-36)$$

Assuming that  $t_0$  ( $t_0 = 0$ ) and  $t_f$  indicate the initial time and finish time. In order to achieve a smooth motion of the joint, the trajectory function should satisfy constraints shown in Table 4-5.

*Table 4-5 Constraints for six parameters*

	$\theta(t)$	$\dot{\theta}(t)$	$\ddot{\theta}(t)$
$t_0$	$\theta_0$	0	0
$t_f$	$\theta_f$	0	0

According to above constraints, the functional expression of six parameters can be obtained as follows.

$$\theta(0) = \theta_0 = a_0 \quad (4-37)$$

$$\theta(t_f) = \theta_f = a_0 + a_1t_f + a_2t_f^2 + a_3t_f^3 + a_4t_f^4 + a_5t_f^5 \quad (4-38)$$

$$\dot{\theta}(0) = 0 = a_1 \quad (4-39)$$

$$\dot{\theta}(t_f) = 0 = a_1 + 2a_2t_f + 3a_3t_f^2 + 4a_4t_f^3 + 5a_5t_f^4 \quad (4-40)$$

$$\ddot{\theta}(0) = 0 = 2a_2 \quad (4-41)$$

$$\ddot{\theta}(t_f) = 0 = 2a_2 + 6a_3t_f + 12a_4t_f^2 + 20a_5t_f^3 \quad (4-42)$$

Finally, coefficients ( $a_0, a_2, a_3, a_4, a_5$ ) of the five polynomial functions can be decided based on above equations as follows.

$$a_0 = \theta_0$$

$$a_1 = 0$$

$$a_2 = 0$$

$$\begin{aligned}
a_3 &= \frac{10(\theta_f - \theta_0)}{t_f^3} \\
a_4 &= \frac{-15(\theta_f - \theta_0)}{t_f^4} \\
a_5 &= \frac{6(\theta_f - \theta_0)}{t_f^5}
\end{aligned} \tag{4-43}$$

#### 4.4.3. Trajectory planning in the task space

Space trajectory planning is the generation of a time sequence of values for the joint variables as the manipulator moves from the initial to target positions. Particularly, its motion is nonlinear and difficult to predict for the end effector motion. In terms of the task space trajectory planning, however, the path of the motion trajectory is often more sophisticated and sometimes a specific trajectory path is requested, e.g., the requested motion path is a straight line or a circular arc shape. The difference between two types of trajectory planning is that each joint angle can be obtained directly in joint space trajectory planning, whereas task space trajectory planning generates the end-effector poses, which requires repeated solutions of the inverse kinematics to obtain each joint angle.

It is known from Section 4.4.1, the robot end-effector will move slowly following a straight line to approach the entry point on the patient head. It is assumed that the robot end-effector moves along a straight line from point  $P_1(x_1 \ y_1 \ z_1)$  to point  $P_2(x_2 \ y_2 \ z_2)$ . Notably,  $P_1$  represents the position of the end point based on joint space trajectory planning.  $P_2$  represents the position of entry point on the patient head. Distance  $d_{12}$  from  $P_1$  to  $P_2$  is:

$$d_{12} = \sqrt{(x_2 - x_1)^2 + (y_2 - y_1)^2 + (z_2 - z_1)^2} \tag{4-44}$$

For vectors  $i, j, k$  that represent points  $P_1$  and  $P_2$  in a 3D space, namely,  $P_1 = x_1i + y_1j + z_1k$ ,  $P_2 = x_2i + y_2j + z_2k$ , Vector  $P_{12}$  is as follows.

$$P_{21} = P_2 - P_1 = (x_2 - x_1)i + (y_2 - y_1)j + (z_2 - z_1)k \tag{4-45}$$

Its unit direction vector is:

$$n_{21} = \frac{P_{21}}{d_{12}} \tag{4-46}$$



Assuming that the motion velocity along the straight line from point  $P_1$  to point  $P_2$  is  $v$ , the total time of motion is  $T$ , and the position vector for the robot end effector at time  $t$  is  $P_t = x_t i + y_t j + z_t k$ , there is:

$$P_t = P_1 + n_{21} vt, \quad t \in [0, T] \quad (4-44)$$

where,  $[x_t \ y_t \ z_t]$  is the position of the robot end-effector at time  $t$ . The above description is a linear trajectory planning algorithm for robot in the task space.

#### 4.4.4. Simulation and results

In order to verify feasibility of the proposed trajectory planning strategy for the MRI-guided robot-assisted stereotactic neurosurgical procedure, simulations are conducted using MATLAB. The simulation results are shown from Figures 4-10 to 4-13. Figure 4-10 shows a path trajectory of the robot end effector from the initial point to end point, where the initial point refers to the posture of the end-effector at the initial robot configuration, and the end point is defined the entry point of the needle/catheter insertion (as shown in Figure 4-8). According to results of simulation in Figures 4-11 and 4-12, trajectories of the angular displacement, angular velocity, and angular acceleration for each joint are continuous and have no sudden change, which assures the smooth movement of the MRI-guided robot from the initial point to end point. Furthermore, from Figure 4-13, it can be seen that the maximum velocity and acceleration of the robot end effector are less than 3mm/s and 2.5mm/s<sup>2</sup>, which are small enough for the manipulator to perform a relatively smooth and steady trajectory.

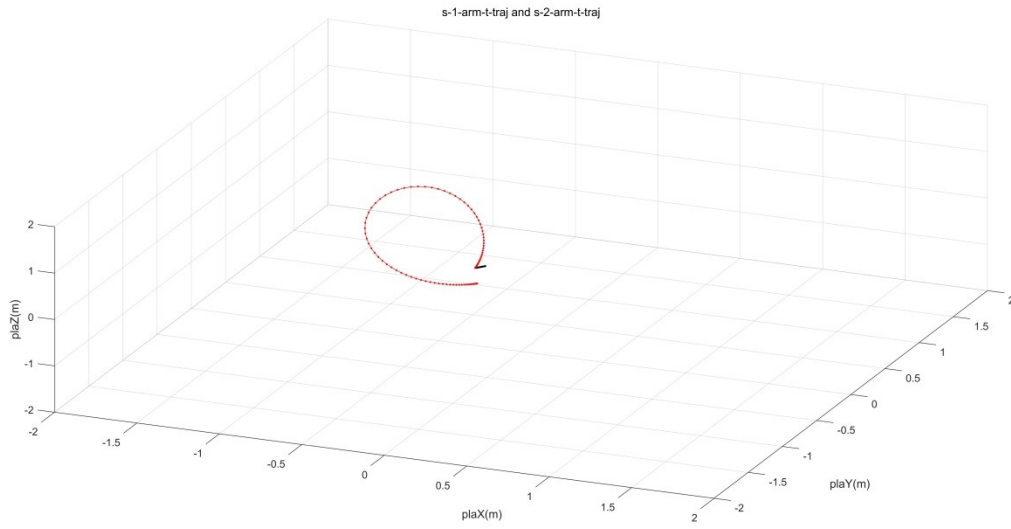


Figure 4–10 Trajectory path of the robot manipulator

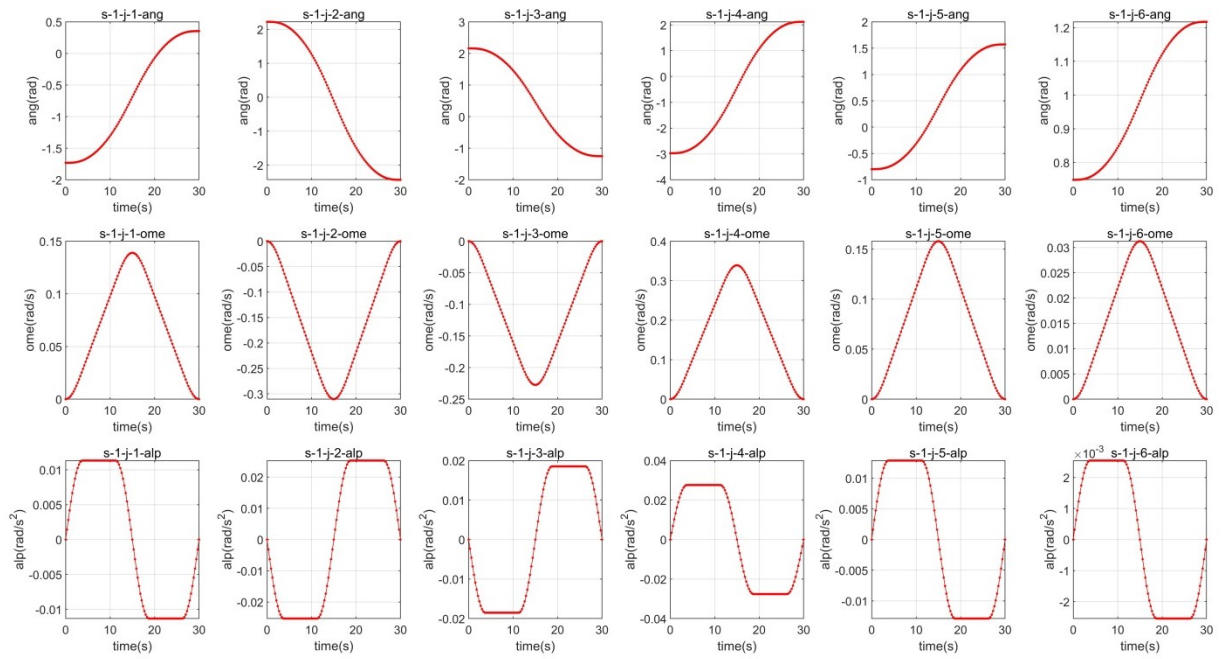


Figure 4–11 Trajectory simulation of displacement, velocity, and acceleration of each joint in joint space

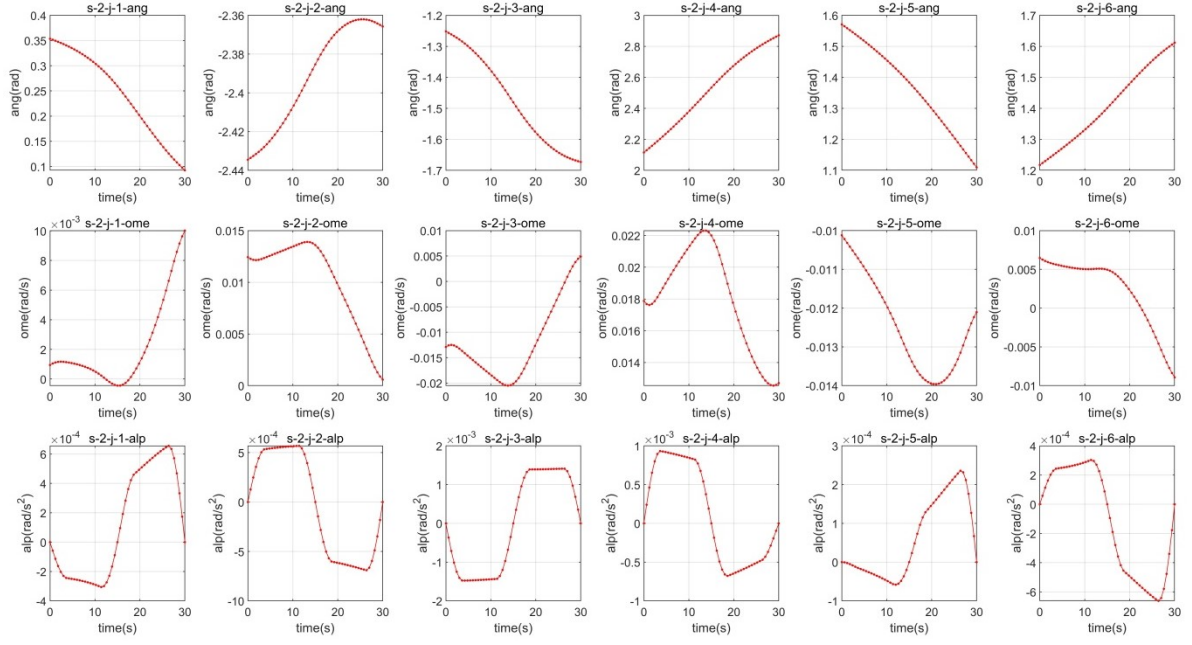


Figure 4-12 Trajectory simulation of displacement, velocity, and acceleration of each joint in task space

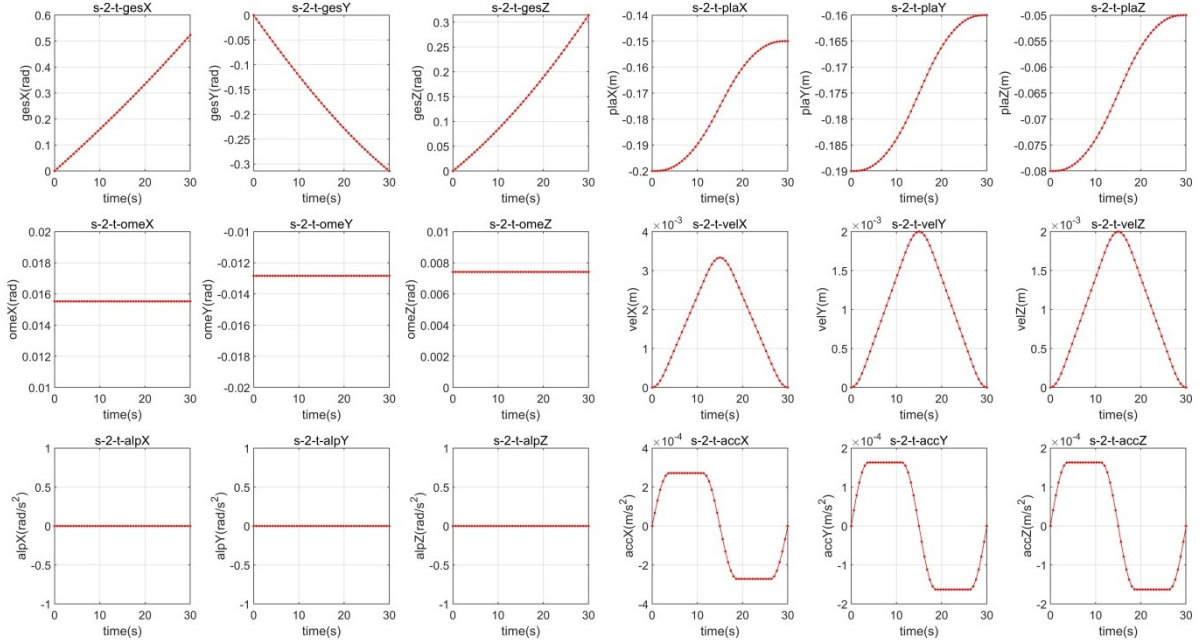


Figure 4-13 Results of trajectory simulation for end effector in task space

## 4.5. Summary

In this chapter, the proposed forward and inverse kinematic models of the MRI-guided robot are built and validated by simulations using MATLAB. In addition, based on the safety concerns of performing the stereotactic neurosurgery, trajectory planning strategies are proposed to avoid contact between the robot end-effector and patient head. Free and restricted areas are defined as the working space of the manipulator. Trajectories in each area are planned individually and simulated by MATLAB. Results show that the manipulator motion produces smooth and well-performing trajectories, and in the restricted area, the end-effector of the manipulator slowly follows a linear trajectory with the desired direction to ensure the safety of the surgery.

# Chapter 5. MRI compatibility analysis and simulation

## 5.1. Introduction

Compatibility of the MRI-guided robot is required in workspace of the clinical procedure. The workspace compatibility is that the maximum arm size of the robot satisfies surgical requirements. Specifically, the working area of the robot end effector should cover the patient head completely without blind spots in clinical applications. MR compatibility is one of the essential requirements for any devices or tools used under the MRI environment, including: (1) The equipment implanted in the MRI environment cannot impact the normal operation of the MRI scanner; (2) The implanted equipment itself will not be affected by the special MRI environment; (3) The patient safety must be ensured absolutely when implanting other equipment into the MRI environment. This is due to the fact that there are three special fields existed in an MRI environment including: (a) the high uniform static magnetic field, (b) excitation radio frequency (RF) field, and (c) fast varying gradient magnetic field. However, when the robot is implanted in the MRI environment, it will inevitably affect each other with the magnetic field, resulting in a decrease of the image quality. Thus, it is necessary to assess compatibility of the MRI-guided robot from perspectives of the real surgical procedure and MRI environment.

This chapter is organized as follows. Section 5.2 analyzes and simulates the workspace compatibility for the MRI-guided robot using MATLAB. Section 5.3 defines materials for fabrication of the MRI-guided robot and weight, the MR compatibility in the real MRI environment is simulated using the ANSYS Maxwell software. The chapter is summarized in Section 5.4.

## 5.2. Workspace compatibility for the MRI-guided robot

### 5.2.1. MRI-guided robot workspace analysis

Workspace of the MRI-guided robot refers to all locations that an original coordinate system of the end-effector (needle/catheter) can reach in the space, which is one of the important design parameters to evaluate performance of the robot. The size and shape of the reachable work area are very critical for the existing task dead angle that the end-effector of a robot can be reached during the work process. This parameter is also one of the significant factors that affect users to choose the product. Figure 5-1 illustrates the detail information of the placement of the MRI-guided robot based on actual surgical operations. Once the MRI-guided robot has been placed, the distance between the robot base and patient head is roughly 300 mm in the X-axis direction as shown in Figure 5-1. As maximum dimensions of an adult male head are  $199\text{mm} \times 161\text{mm} \times 209\text{mm}$ , the reachable size of the MRI-guided robot on XZ plane must be more than 509mm so that the patient head can be covered by the robot end effector.

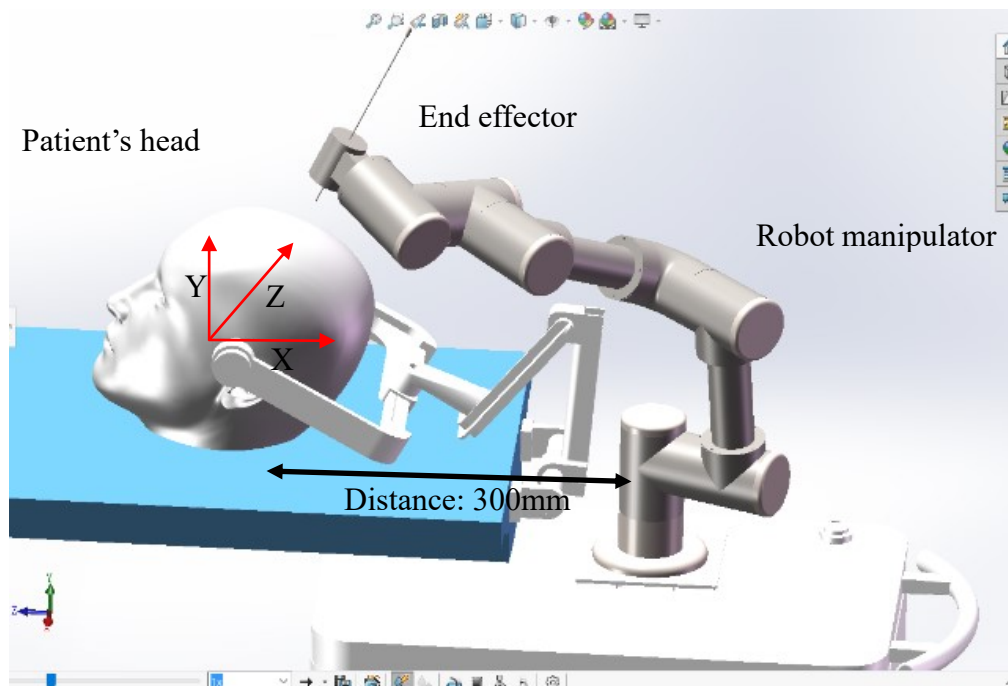


Figure 5-1 3D model of the MRI-guided robot placement during operations

In the previous chapter, DH parameters of the robot were decided based on the forward and inverse kinematics analyses as shown in Table 5-1. The MATLAB software is used to calculate and simulate the workspace of the MRI-guided robot.

*Table 5-1 DH parameters of the MRI-guided robot*

Link ( <i>i</i> )	$a_{i-1}$ mm	$d_i$ mm	$\alpha_{i-1}^\circ$	$\theta_i^\circ$	Value
1	0	$d_1$	$90^\circ$	$\theta_1$	$d_1 = 69\text{mm}$
2	$a_1$	0	$0^\circ$	$\theta_2$	$a_1 = 264\text{mm}$
3	$a_2$	0	$0^\circ$	$\theta_3$	$a_2 = 291\text{mm}$
4	0	$d_4$	$90^\circ$	$\theta_4$	$d_4 = 104\text{mm}$
5	0	$d_5$	$-90^\circ$	$\theta_5$	$d_5 = 94\text{mm}$
6	0	$d_6$	$0^\circ$	$\theta_6$	$d_6 = 85\text{mm}$

### 5.2.2. Workspace simulation and results

In this section, a simulation method is utilized to decide workspace of the MRI-guided robot, guided by the probability and statistics theory [71]. If the working domain of the proposed 6-DOF MRI-guided robot is assumed as  $W(P)$ , the mapping relation between its variables of joint space and working domain can be expressed as follows.

$$W(P) = \{P(\theta) : \theta \in Q\} \quad (5-1)$$

where  $\theta = [\theta_1, \theta_2, \theta_3, \theta_4, \theta_5, \theta_6]^T$  represents robotic joint variables,  $Q$  is the joint space variable, also called the constrained space. Due to the fact that the motion range of the robot joints is restricted by its design structure, linkage position, conditions of external installation, etc. in its practical applications, the environment of actual applications should be considered when determining constrained space  $Q$  as follows.

$$Q = \{\theta \mid \theta_n^d \leq \theta_n \leq \theta_n^u, n = 1, 2, \dots, 6\} \quad (5-2)$$

where  $\theta_n^u$  and  $\theta_n^d$  represent upper and lower limits of the joint motion, respectively. If the origin of the robot end effector coordinate system is used as the reference point, the workspace

can be expressed as follows.

$$W(P) = \begin{cases} P_x(\theta_n) \\ P_y(\theta_n) \\ P_z(\theta_n) \end{cases} \quad \theta_n^d \leq \theta_n \leq \theta_n^u, \quad n = 1, 2, \dots, 6 \quad (5-3)$$

Using the MATLAB software for the forward kinematic based on Eq. 5-3, the location of the robot end-effector can be obtained. The function of random values in MATLAB is used to randomly select an angle value within the angle interval of each joint, and these joint variables will be combined (there are infinitely many combinations). The process is illustrated by taking one of the joint variables  $\theta_1$  as example as follows. Firstly,  $N$  random points are generated in the interval  $[0, 1]$ . According to the motion range of  $\theta_1$ ,  $\theta_1^d \leq \theta_1 \leq \theta_1^u$ ,  $(\theta_1)_i = \theta_1^d + (\theta_1^u - \theta_1^d)\text{Rand}$ , where,  $i$  represents the  $i$ -th random value in  $N$  times. Similarly, other joint variables of the robot are also assigned the same random value. In the simulation, the random posture  $N$  of the robot was set as 10000, and variables of  $\theta_i$  for each joint were set as follows.

$$\begin{aligned} \theta_1: & -180^\circ \text{ to } 180^\circ, \quad \theta_2: -60^\circ \text{ to } 60^\circ, \quad \theta_3: -45^\circ \text{ to } 45^\circ, \quad \theta_4: -45^\circ \text{ to } 45^\circ, \quad \theta_5: -90^\circ \text{ to } 90^\circ, \\ \theta_6: & -180^\circ \text{ to } 180^\circ. \end{aligned}$$

As a result, Figure 5-2 shows the reachable workspace of the 6 DOF MRI-guided robot manipulator. Figure 5-2 (a) illustrates the 3D projection of the manipulator workspace. Figures 5-3 (b), (c), and (d) are the projection of manipulator workspace on XY, YZ, and XZ planes respectively. From these results, the manipulator end effector can reach a maximum reachable distance of 979 mm on the XZ plane, which is larger than 509 mm. Furthermore, projections on XY and YZ planes show that the reachable workspace can cover the patient head completely. Thus, it proves that the design size can satisfy the clinical operation requirement.



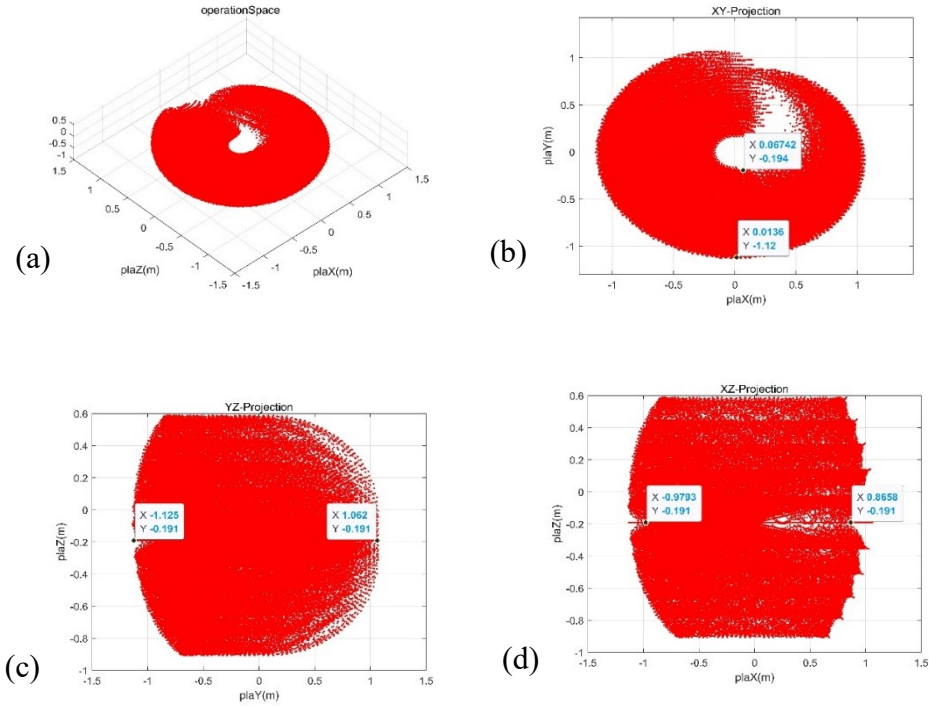


*Figure 5–2 Workspace simulation of the 6-DOF MRI-guided robot; (a) 3D reachable workspace; (b) XY plane reachable workspace; (c) YZ plane reachable workspace; (d) XZ plane reachable workspace*

### 5.3. MRI compatibility

#### 5.3.1. MRI compatibility analysis under the MRI environment

Magnetic resonance imaging (MRI) is a medical imaging technology with a great impact on metal materials. According to the ASTM F2052 Standard [72], materials used in the MRI environment include MR unsafe, MR safe and MR conditional. For the MRI-guided robot, metal materials are inevitably used because of their good mechanical properties and matured machining technology. Although metal materials are the MR safe, they still have a certain negative impact on the MRI environment. Due to the fact that the MRI system is complicated with three main fields including (a) the strong uniform static magnetic field generated by a magnet (typically 1.5T and 3.0T in the medical application), (b) the gradient magnetic field

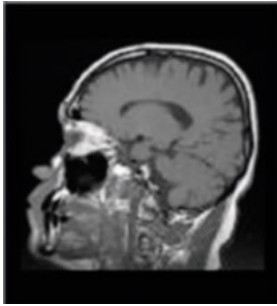
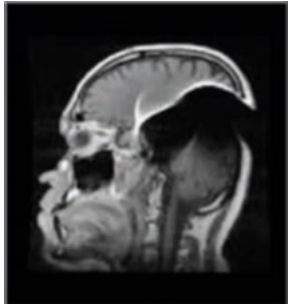
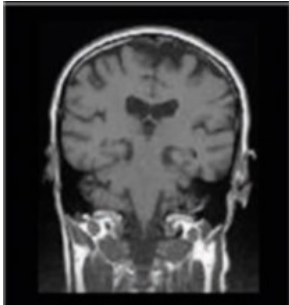
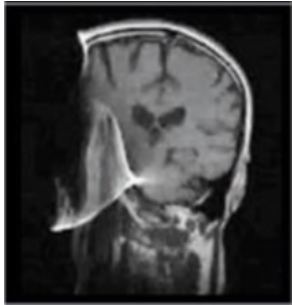
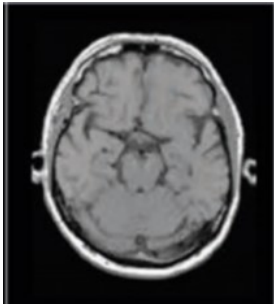
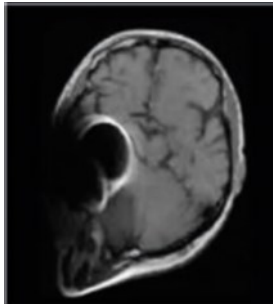
with time varying spatial, and (c) a radiofrequency (RF) field. Any field disturbance or interference will have a negative impact on the final MR image, which makes the diagnosis impossible. According to the ASMT standard, some hazards for medical devices in the MR environment are as follows.

a) Magnetically Induced Displacement Force: Both static magnetic field and spatial gradient static magnetic field generate force on metallic materials. This magnetically induced displacement force may result in unnecessary movement of medical devices, which may cause tissue damage.

b) Magnetically Induced Torque: The static magnetic field of the MR system generates torque on the metallic material. Also, this magnetically induced torque may cause unnecessary movement of medical devices, which may result in tissue damage.

c) Heating: The radio frequency (RF) and varying gradient field (dB/dt) of the MR system will cause heating of metallic materials, which may lead to damage to human tissues or accelerate equipment aging.

d) MR Image Artifacts: The presence of metal implants or other medical devices can cause susceptibility artifacts in acquired MR images. If the range of artifacts is too large, it will affect the clinical diagnosis results. There are many factors that cause MR artifacts, among which metal implantation under the MRI environment is one of the most significant reasons. Figure 5-3 compares MR images in cases of the metal implantation and non-metal implantation.

Pulse sequence/ Plane	Spin-echo; Without metallic material	Spin-echo; With metallic material
Sagittal		
Coronal		
Axial		

*Figure 5–3 MR images in three orthogonal planes (sagittal, coronal, and axial) in a 1.5 Tesla scanner without the metal implant (first column) and with the metal implant (second column) for spin-echo [73].*

Therefore, considering the specific MRI environment, metallic materials selected should be specially assessed. According to the relative permeability and magnetization characteristics, the metallic materials used to make devices include three types: diamagnetic materials, paramagnetic materials, and ferromagnetic materials. Since ferromagnetic materials are strongly interfered by magnets, they are generally not considered for making implantable devices. The paramagnetic metal materials will be magnetized when implanted in a magnetic field environment. Its magnetization is related to the magnetic susceptibility of the material

and the strength of the applied magnetic field, which can be decided by following equation.

$$M = \chi_m H \quad (5-5)$$

where  $M$  is the magnetization,  $\chi_m$  is the magnetic susceptibility of materials, and  $H$  is the strength of magnetic field.  $H$  is defined as:

$$H = \frac{1}{\mu_0} B - M \quad (5-6)$$

where  $\mu_0$  is the vacuum magnetic permeability,  $B$  is the magnetic induction intensity. The expression of  $B$  is as follows.

$$B = \mu_0(H + M) = \mu_0(1 + \chi_m)H = \mu_0\mu_r H \quad (5-7)$$

where  $\mu_r$  is the relative magnetic permeability,  $\mu_0\mu_r$  is defined as the magnetic permeability of the material. Therefore, according to above equations, if the material permeability is given, the intensity of the magnetic field generated around the magnetized material can be decided.

The magnetized metal will affect the uniformity of the magnetic field [26]. MRI has very high requirements on the uniformity of the main magnetic field because of follow reasons [23] [72]:

- (1) Highly uniform magnetic field strength can improve the image signal-to-noise ratio (SNR), where SNR is one of significant indicators to assess the quality of MR imaging.
- (2) Uniform magnetic field strength is a prerequisite for ensuring the accuracy of MR signal spatial positioning.
- (3) Uniform magnetic field strength can reduce artifacts (especially susceptibility artifacts),
- (4) The highly uniform magnetic field is conducive to large-field scanning.
- (5) Only a highly uniform magnetic field can make full use of the fat saturation technology for fat suppression scanning.

Therefore, simulation of the MRI compatibility involves material properties and uniform static magnetic field in the MRI environment

### 5.3.2. RI compatibility simulation and results

The electromagnetic simulation software ANSYS Maxwell is used to build the MRI environment based on the ASTM F2052 standard test method for magnetically induced displacement force and evaluation of MRI image artifacts [74]. Strengths of the magnetic field are defined as 1.5T and 3.0T, respectively, based on the real clinical imaging procedure.

The first step creates a static magnetic field to define strengths of the magnetic field. The direction of the static magnetic field is assumed from left to right in the MRI environment (e.g. 3T) as shown in Figure 5-4. Notably, the unit of the magnetic field is not T but A/m in this software, where  $1\text{T}=8\text{e}5\text{ A/m}$ .

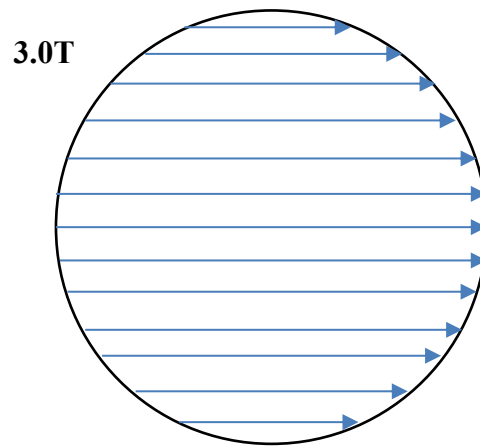


*Figure 5–4 Magnetic field distribution in the MRI environment*

The second step imports a simplified 3D model of the MRI-guided robot without considering screws, threaded holes, chamfers, and tool needles/catheters, etc. into the static magnetic field created by the ANSYS Maxwell software, and sets materials for each part of the robot. According to Chapter 3, PEEK, POM, and 304 stainless steel are selected to make the MRI-guided robot. PEEK and POM are engineering plastics with non-magnetic, and 304 stainless steel is austenitic alloy with paramagnetic. Table 5-2 lists its main chemical composition. Table 5-3 shows the physical properties of the three selected materials.

*Table 5-2 List of chemical compositions for 304 stainless steel*

Chemical composition	C	Mn	P	S	Si	Cr	Ni
Content percentage (%)	0.08	2.00	0.045	0.03	1.0	20.0	11.0

*Table 5-3 Physical properties of three different types of materials*

Material	Elastic Modulus	Yield Strength	Density	magnetic permeability
304 SS	193 MPa	205 MPa	7.93 g/cm <sup>3</sup>	1.1 H/m
PEEK	/	95 MPa	1.29 g/cm <sup>3</sup>	0.83 H/m
POM	/	35 MPa	1.42 g/cm <sup>3</sup>	0.79 H/m

The main structure of the MRI-guided robot includes the joint, link, end effector, and base as shown in Figure 5-5. Materials of each part are as follows.

Robot joint: PEEK; Robot link: 304 SS; Robot end effector: 304 SS;

Robot base: 304 SS; Others: POM;

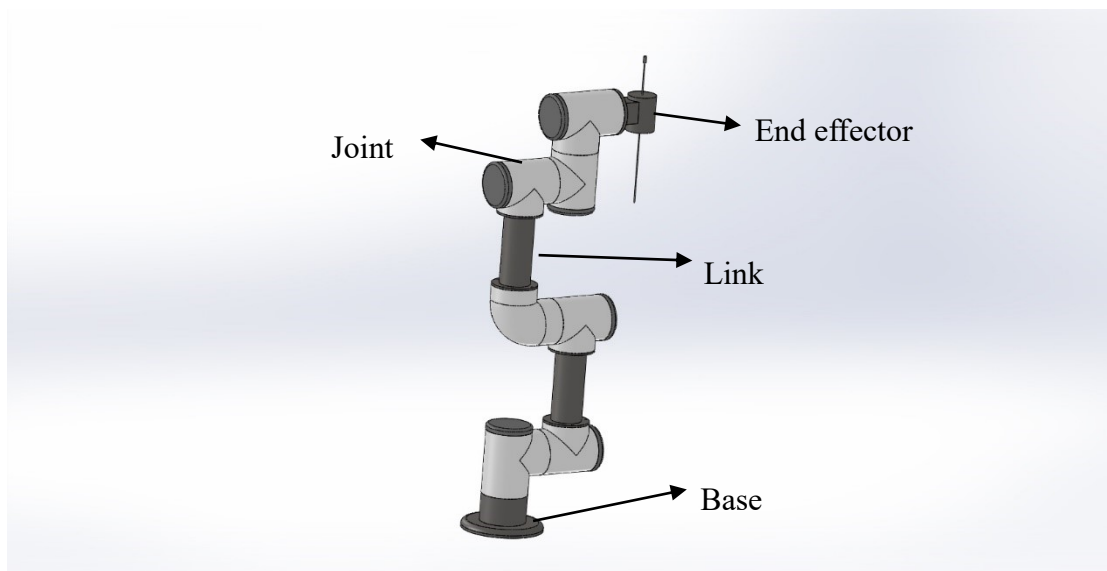


*Figure 5–5 Brief structure of the MRI-guided robot*

The third step sets the magnetic field boundary as shown in Figure 5-6, and adds the magnetic field force solver.

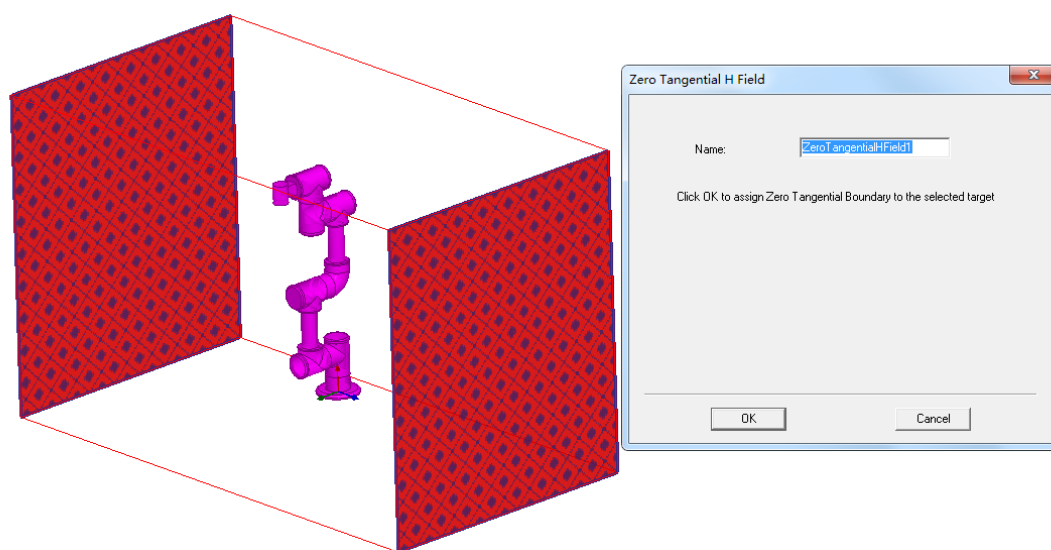


Figure 5-6 Magnetic field boundary in software

In terms of the magnetically induced displacement force, the ANSYS Maxwell software provides a magnetic field force calculation function as shown in Figure 5-7.

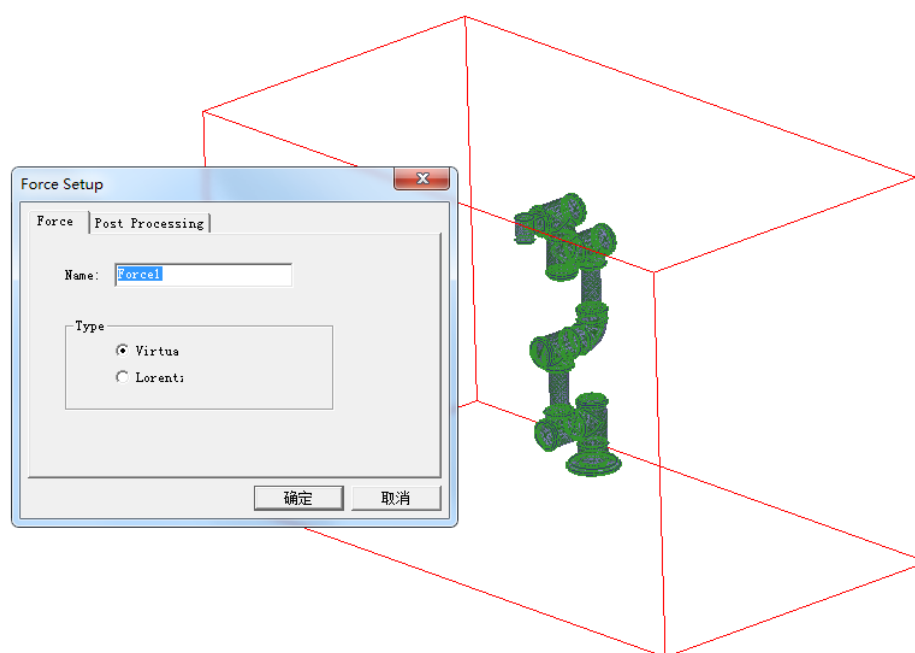
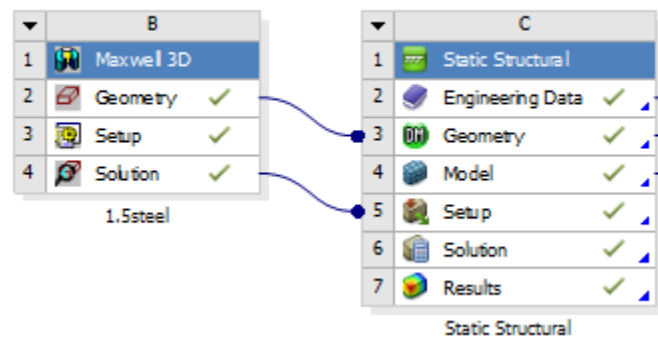


Figure 5-7 Magnetic field force calculation

Next, through the functional mutual conversion between Maxwell and Workbench in ANSYS, results of the magnetic force can be transferred into the structural simulation as shown in Figure 5-8. The step analyzes the strain and stress of the proposed MRI-guided robot under the force caused by the magnetic field through the finite element analysis. Since the MRI-guided robot is used to position and guide the insertion of the needle/catheter during the actual operation, its maximum external force does not exceed 2N which can be ignored.



*Figure 5–8 The magnetic force from Maxwell to Static Structural analysis*

Finally, the bottom of the robotic arm is set as a fixed constraint and meshed as shown in Figure 5-9.



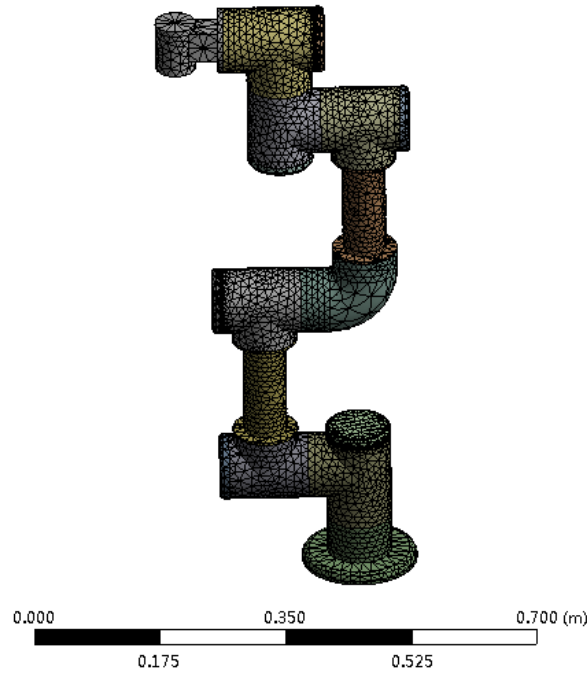


*Figure 5-9 Mesh of MRI robot in ANSYS Workbench*

Results of the simulation for evaluation of MR image artifacts are shown in Figures 5-10 and 5-11. The color background in the figures represents the strength of the MRI static magnetic field  $B_0$ , that is, 1.5T and 3.0T. The scale bar on the left represents the color corresponding to different magnetic field strengths. From Figures 5-10 and 5-11, it is clear that the color around the robot linkage differs from the background color. It is due to the fact that the paramagnetic material 304 stainless steel is magnetized in a strong magnetic field and generates a static magnetic field that differs from that of the MRI environment. When the MRI scanner is working, two magnetic fields of different strengths must interact each other resulting in the image distortion. The results show that the new magnetic fields generated around the robot are 1.506 T and 3.012 T, respectively. According to the ASTM F2119 Standard, the static magnetic field  $B_0$  in the MRI environment must not be changed by more than 10% of its strength for the implanted device, which is considered to be usable in the MRI environment. From the results, however, the magnetic fields changed around the proposed MRI-guided robot are no more than 10% in 1.5T and 3.0T MRI environments. Therefore, the proposed MRI-guided robot can be used safely in the MRI environment.

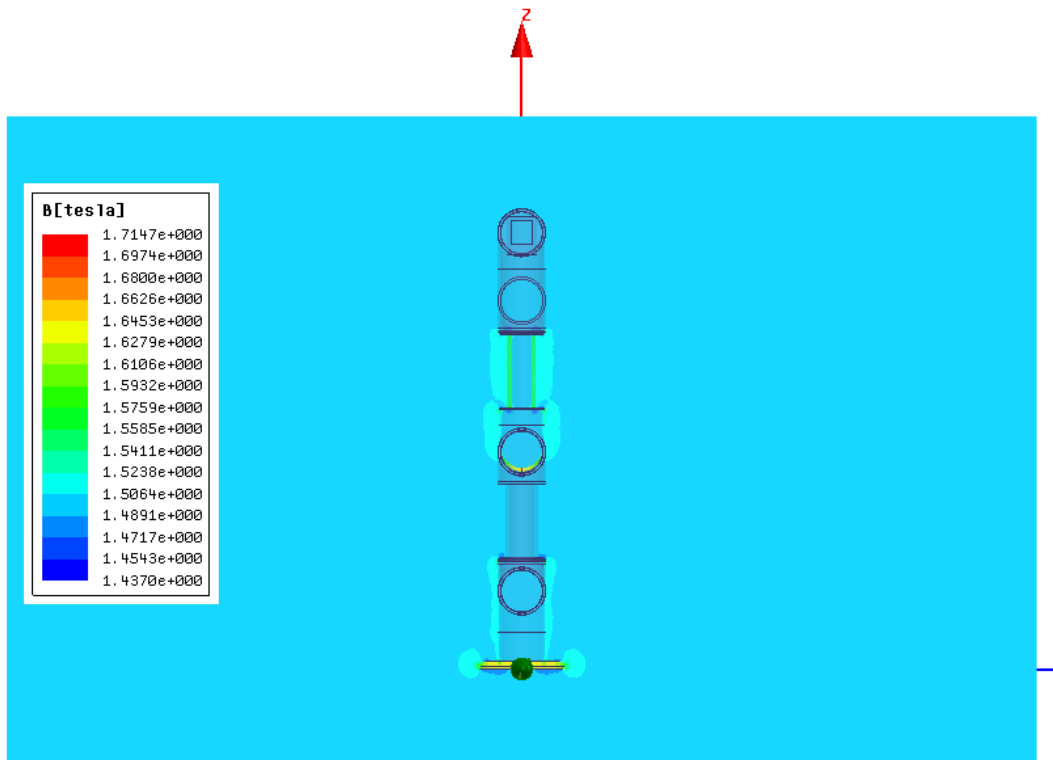


Figure 5–10 MR image artifacts evaluation in 1.5T MRI environment

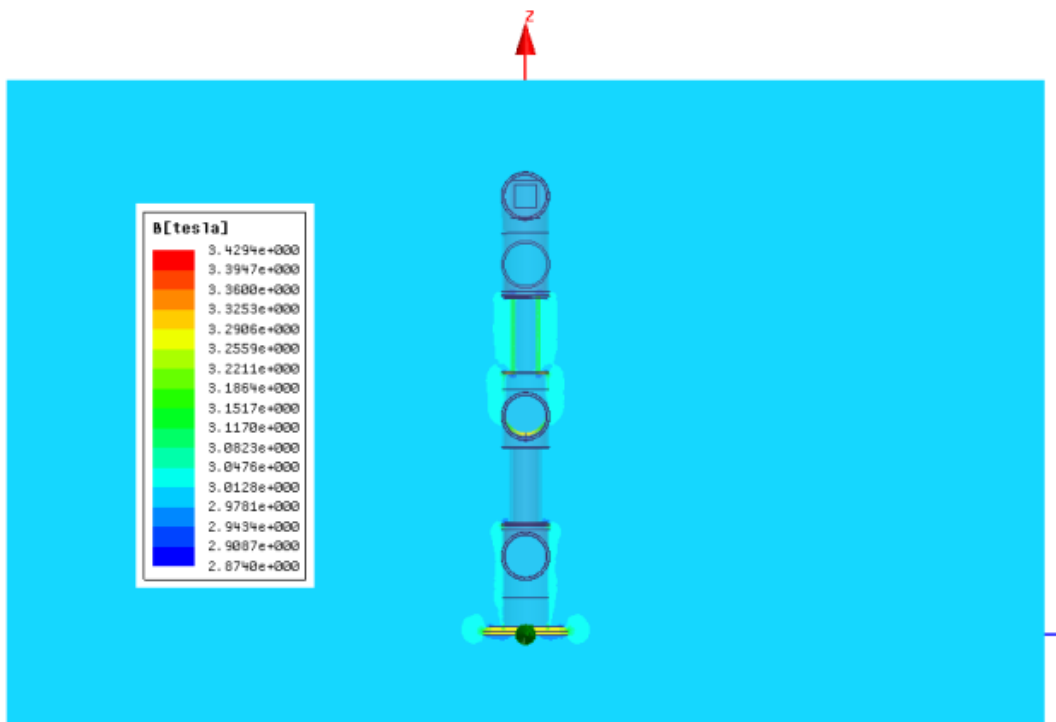


Figure 5–11 MR image artifacts evaluation in 3.0T MRI environment

The strain and stress analysis results of the MRI-guided robot subjected to the magnetic field forces at different magnetic field strengths are shown in Figures 5-12 to 5-15.

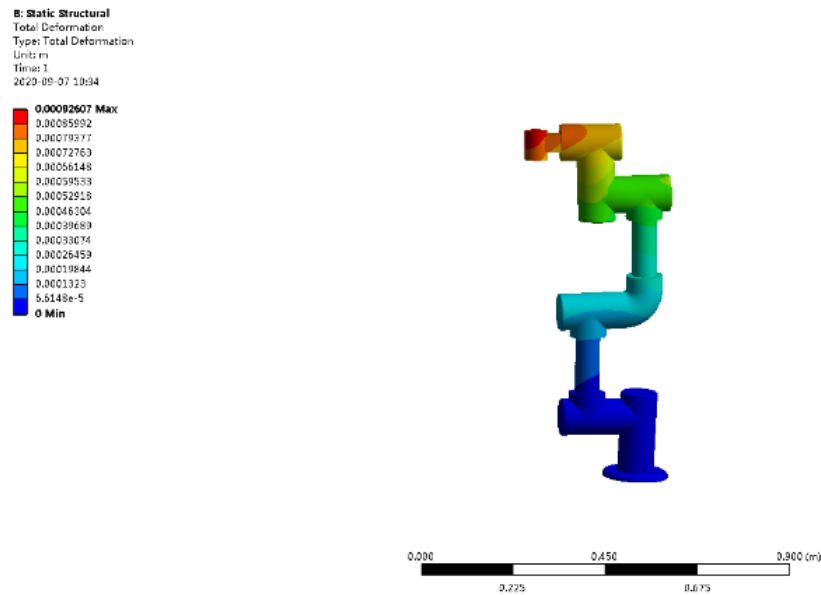


Figure 5–12 Strain of the MRI-guided robot in 1.5T magnetic force

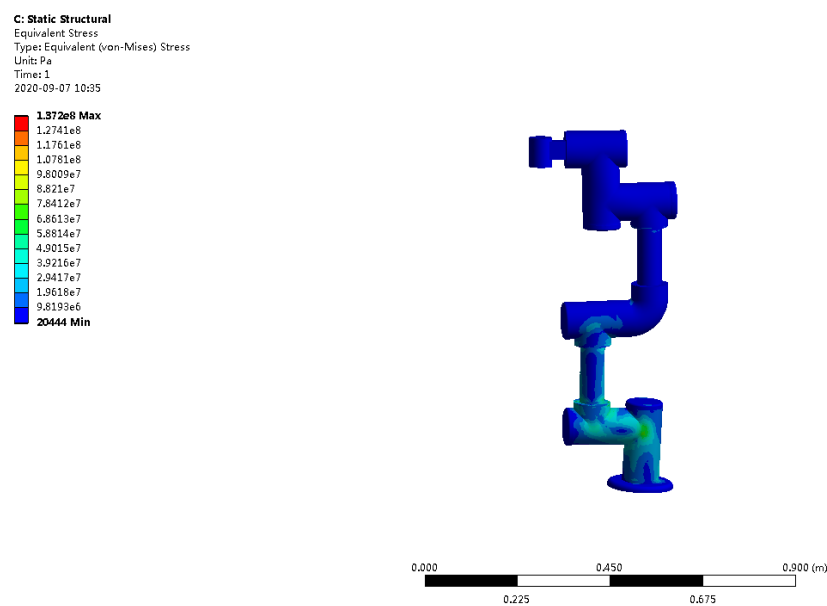
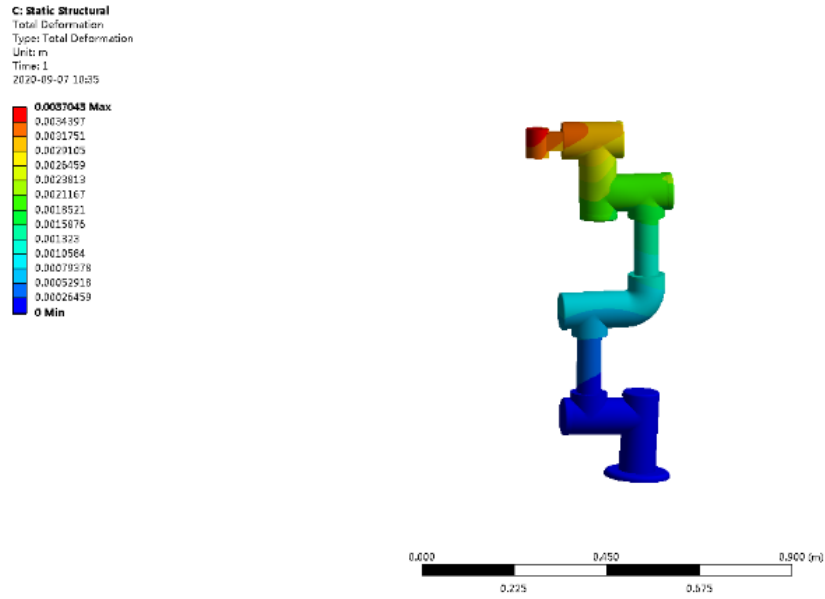
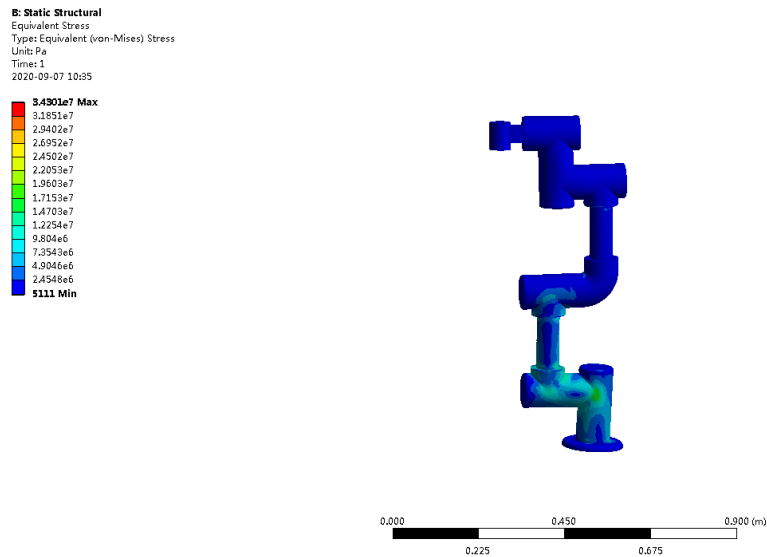


Figure 5–13 Stress of the MRI-guided robot in 1.5T magnetic force



*Figure 5–14 Strain of the MRI-guided robot in 3.0T magnetic force*



*Figure 5–15 Stress of the MRI-guided robot in 3.0T magnetic force*

As a result, from Figures 5-13 and 5-15, the maximum stresses of the MRI-guided robot under 1.5T and 3.0T magnetic forces are 15 MPa and 34 MPa, respectively, and the stress is mainly distributed around the base area of the MRI robot. The total deformations under 1.5T and 3.0T magnetic forces are 0.9mm and 3.7mm, respectively. From Figures 5-12 and 5-14, the deformation is mainly distributed at the end effector of the MRI-guided robot. Results of the MRI compatibility assessment for the proposed robot are summarized in Table 5-4.

*Table 5-4 MR compatibility evaluation for the MRI-guided robot*

MR compatibility evaluation	Evaluation method	Acceptance criteria ( According to ASTM Test Standard)	Result of simulation	Whether meet the implantation standard (Yes/No)
MR Image Artifacts	Simulation by ANSYS Maxwell	The artifact area should be less than 10% of the implanted device area	Artifact area is less than 10% of MRI-guided robotic area	Yes
Magnetically Induced Displacement Force	Simulation by ANSYS Workbench	The maximum stress of the implanted device in the magnetic field should be less than the yield strength of its manufacturing material	Maximum stress under magnetic force: 34 MPa  Yield strength of PEEK: 95 MPa	Yes

However, the deformation of the robot end effector is 3.4 mm under the force of a 3.0T magnetic field. The robot working in this environment will accelerate the material failure to reduce the service life of robot. Therefore, it is recommended to apply the proposed robot with a 1.5T MRI scanner for the stereotactic neurosurgery.

#### 5.4. Summary

In this chapter, both workspace compatibility and MRI compatibility of the proposed MRI-guided robot were analyzed and simulated. Results show that the robot can satisfy the clinical requirement for the real surgical operation. Furthermore, the total mass of the robot is obtained by determining the selection of materials for the robot shell. Finally, through the magnetic simulation and FEA, it proves that the proposed MRI-guided robot can meet the need of the MRI compatibility. However, the deformation and stress of the robot increases with increasing intensity of the static magnetic field. In order to increase the robotic service life, it is recommended that the robot works with 1.5T MRI scanner.

# Chapter 6. Conclusions and future work

## 6.1. Research summary

The objective of this study was the conceptual design of an MRI-guided robot to replace the existing stereotaxic frame-positioning instrument in neurosurgical procedures. Based on customer requirements for MRI-guided and robotic-assisted systems in the stereotactic neurosurgery, QFD and Benchmark methods were used for the concept generation of the proposed robot. Design parameters of the MRI-guided robot were prioritized to meet customer needs through the relationship matrix analysis between customer requirements and technical metrics in the conceptual design phase.

From results of the relationship matrix, the motor, material, and positioning accuracy are the top three technical specifications that need to be prioritized in the design process to meet customer requirements. In order to obtain the design solution of the MRI-guided robot, three benchmarking robot products were selected to make decisions on design parameters and optimal components for the stereotactic neurosurgery. Finally, a 3D model of 6 DOF robot manipulator with the mobile base was built. The robot manipulator will be actuated by the piezoelectric motor which is made by Shinsei ®, Japan. Results show that the proposed MRI-guided robot can meet initial customer requirements in terms of the small size and light weight compared to other three benchmarking products.

Another important design feature of this robot is that the end-effector has an additional degree of freedom: the needle insertion, which is independent of the other degrees of freedom. The needle insertion is operated by the surgeon. Although, technically, the robot can perform the insertion, the current plan reserves this task to the surgeon owing to safety, ethical and legal considerations. It is assumed that incisions have already been made in the brain for the needle to go through and remove a sample of the tissue to test for tumor cells. This assumes that the needle will primarily insert through soft tissues only.

Considering the safety of neurosurgery, a trajectory planning strategy was proposed to ensure the smooth and continuous motion of the robot during the operation. Since the robot

end-effector is a needle-guided surgical tool insertion, it requires the end-effector with the capability to slowly approach the entry point of the patient head in a straight line to eliminate needle-skin puncture injuries.

Therefore, based on the robotic forward and inverse kinematics models, the trajectory planning strategy was defined as joint space trajectory planning in the free zone and task space trajectory planning in the safe zone. In the task space trajectory planning, the robot end-effector will slowly approach the entry point of the patient head along a straight path. Results of the simulation show that the displacement, velocity, and acceleration of each joint of the robot are continuous and there is no sudden changes. The maximum speed of the end-effector is 3 mm/s in the task space trajectory planning, which can reduce the potential of any harmful and undesired contact with the head skin.

Finally, the MRI compatibility of the proposed MRI-guided robot was analyzed and simulated. From results of the workspace compatibility simulation, it shows that the size of the proposed robot can meet the clinical requirements, i.e., it can cover the patient head without any dead angle for neurosurgeons to complete the surgery. Results of magnetic field compatibility simulations verify that the proposed robot can be used safely in the MRI environment.

## 6.2. Research contributions

Contributions of this research are as follows.

(1) Feasibility and state-of-the-art literature of robot systems for the stereotactic neurosurgery are reviewed based on MRI-guided neurosurgical procedures.

(2) Technical specifications and weights for the MRI-guided robot are determined based on customer requirements in the conceptual design stage.

(3) Based on three benchmarking products for the stereotactic neurosurgery, target values are defined for technical specifications including the size, weight, degrees of freedom, and parameters of critical components. A conceptual 3D model of the MRI-guided robot is proposed.

(4) The robot forward kinematic and inverse kinematic models are built. The accuracy of

kinematics models is verified via simulation.

(5) Based on conditions in the operation theatre, especially for neurosurgery, a sectioned trajectory planning approach is proposed and simulated.

(6) The workspace compatibility and MRI compatibility are simulated and verified.

### 6.3. Future work

MRI-guided robots are an evolving direction of interventions in the stereotactic neurosurgery, which is a key technology to address existing clinical surgical drawbacks, such as reducing surgical risks and improving surgical efficiency. In this thesis, a conceptual MRI-guided robot was proposed based on customer requirements. Through the kinematic analysis and trajectory planning simulation, as well as MRI compatibility simulation, the proposed robot is validated to meet customer requirements in terms of the small size, light weight, and MR safe. Further work will be considered as follows.

(1) In order to complete the MRI-guided robot control system, the dynamic analysis will be conducted. Based on the kinematics and dynamics of the robot, an optimization algorithm can be proposed to improve the positioning accuracy of the robot.

(2) Reliability of the robot needs to be further researched regarding the safety of clinical operations.

(3) From the MRI compatibility analysis in Chapter 5, the MRI environment constrains applications of medical devices, i.e., MR unsafe, MR safe, and MR conditional. To further verify the MRI compatibility, a prototype robot will be fabricated and an experimental platform for the MRI environment will be built.



# References

- [1] Galloway, R. L., & Maciunas, R. J. (1990). Stereotactic neurosurgery. *Critical reviews in biomedical engineering*, 18(3), 181-205.
- [2] Lavallee, S., Troccaz, J., Gaborit, L., Cinquin, P., Benabid, A. L., & Hoffmann, D. (1992, January). Image guided operating robot: a clinical application in stereotactic neurosurgery. In *Proceedings 1992 IEEE International Conference on Robotics and Automation* (pp. 618-619). IEEE Computer Society.
- [3] Faria, C., Erlhagen, W., Rito, M., De Momi, E., Ferrigno, G., & Bicho, E. (2015). Review of robotic technology for stereotactic neurosurgery. *IEEE reviews in biomedical engineering*, 8, 125-137.
- [4] Correa-Arana, K., Vivas-Albán, O. A., & Sabater-Navarro, J. M. (2017). Neurosurgery and brain shift: review of the state of the art and main contributions of robotics. *TecnoLógicas*, 20(40), 125-138.
- [5] Peters, B. S., Armijo, P. R., Krause, C., Choudhury, S. A., & Oleynikov, D. (2018). Review of emerging surgical robotic technology. *Surgical endoscopy*, 32(4), 1636-1655.
- [6] Guo, Z., Leong, M. C. W., Su, H., Kwok, K. W., Chan, D. T. M., & Poon, W. S. (2018). Techniques for stereotactic neurosurgery: beyond the frame, toward the intraoperative magnetic resonance imaging-guided and robot-assisted approaches. *World Neurosurgery*, 116, 77-87.
- [7] Díaz, C. E., Fernández, R., Armada, M., & García, F. (2017). A research review on clinical needs, technical requirements, and normativity in the design of surgical robots. *The International Journal of Medical Robotics and Computer Assisted Surgery*, 13(4), e1801.
- [8] Challacombe, B., & Stoianovici, D. (2008). The basic science of robotic surgery. In *Urologic Robotic Surgery in Clinical Practice* (pp. 21-43). Springer, London.
- [9] Gomes, P. (2011). Surgical robotics: Reviewing the past, analysing the present, imagining the future. *Robotics and Computer-Integrated Manufacturing*, 27(2), 261-266.
- [10] Sheehan, J. P., Niranjana, A., Sheehan, J. M., Jane, J. A., Laws, E. R., Kondziolka, D., ... & Lunsford, L. D. (2005). Stereotactic radiosurgery for pituitary adenomas: an intermediate review of its safety, efficacy, and role in the neurosurgical treatment

- armamentarium. *Journal of neurosurgery*, 102(4), 678-691.
- [11] Rahman, M., Murad, G. J., & Mocco, J. (2009). Early history of the stereotactic apparatus in neurosurgery. *Neurosurgical focus*, 27(3), E12.
- [12] Brandmeir, N. J., Savaliya, S., Rohatgi, P., & Sather, M. (2018). The comparative accuracy of the ROSA stereotactic robot across a wide range of clinical applications and registration techniques. *Journal of robotic surgery*, 12(1), 157-163.
- [13] Shchavinskii, Y. V. (1973). First stereotaxic apparatus created by Russian scientists in the 19th century. *Biomedical engineering*, 7(2), 121-124.
- [14] Picard, C., Olivier, A., & Bertrand, G. (1983). The first human stereotaxic apparatus: the contribution of Aubrey Mussen to the field of stereotaxis. *Journal of neurosurgery*, 59(4), 673-676.
- [15] Galloway, R. L., & Maciunas, R. J. (1990). Stereotactic neurosurgery. *Critical reviews in biomedical engineering*, 18(3), 181-205.
- [16] Lavallee, S., Troccaz, J., Gaborit, L., Cinquin, P., Benabid, A. L., & Hoffmann, D. (1992, January). Image guided operating robot: a clinical application in stereotactic neurosurgery. In *Proceedings 1992 IEEE International Conference on Robotics and Automation* (pp. 618-619). IEEE Computer Society.
- [17] Kwoh, Y. S., Hou, J., Jonckheere, E. A., & Hayati, S. (1988). A robot with improved absolute positioning accuracy for CT guided stereotactic brain surgery. *IEEE Transactions on Biomedical Engineering*, 35(2), 153-160.
- [18] Beasley, R. A. (2012). Medical robots: current systems and research directions. *Journal of Robotics*, 2012.
- [19] Bodner, J., Wykypiel, H., Wetscher, G., & Schmid, T. (2004). First experiences with the da Vinci™ operating robot in thoracic surgery. *European Journal of Cardio-thoracic surgery*, 25(5), 844-851.
- [20] Varma, T. R. K., & Eldridge, P. (2006). Use of the NeuroMate stereotactic robot in a frameless mode for functional neurosurgery. *The International Journal of Medical Robotics and Computer Assisted Surgery*, 2(2), 107-113.
- [21] Finlay, P. A., & Morgan, P. (2003). PathFinder image guided robot for

- neurosurgery. *Industrial Robot: An International Journal*.
- [22] Brandmeir, N. J., Savaliya, S., Rohatgi, P., & Sather, M. (2018). The comparative accuracy of the ROSA stereotactic robot across a wide range of clinical applications and registration techniques. *Journal of robotic surgery*, 12(1), 157-163.
  - [23] Tardif, C. L., Gauthier, C. J., Steele, C. J., Bazin, P. L., Schäfer, A., Schaefer, A., ... & Villringer, A. (2016). Advanced MRI techniques to improve our understanding of experience-induced neuroplasticity. *Neuroimage*, 131, 55-72.
  - [24] Pagani, E., Bizzi, A., Di Salle, F., De Stefano, N., & Filippi, M. (2008). Basic concepts of advanced MRI techniques. *Neurological Sciences*, 29(3), 290.
  - [25] Mehrabian, H., Detsky, J., Soliman, H., Sahgal, A., & Stanis, G. J. (2019). Advanced magnetic resonance imaging techniques in management of brain metastases. *Frontiers in Oncology*, 9, 440.
  - [26] Shellock, F. G., Woods, T. O., & Crues III, J. V. (2009). MR labeling information for implants and devices: explanation of terminology.
  - [27] Song, S. E., Hata, N., Iordachita, I., Fichtinger, G., Tempany, C., & Tokuda, J. (2013). A workspace-orientated needle-guiding robot for 3T MRI-guided transperineal prostate intervention: evaluation of in-bore workspace and MRI compatibility. *The International Journal of Medical Robotics and Computer Assisted Surgery*, 9(1), 67-74.
  - [28] Tokuda, J., Song, S. E., Fischer, G. S., Iordachita, I. I., Seifabadi, R., Cho, N. B., ... & Hata, N. (2012). Preclinical evaluation of an MRI-compatible pneumatic robot for angulated needle placement in transperineal prostate interventions. *International journal of computer assisted radiology and surgery*, 7(6), 949-957.
  - [29] Kim, D., Kobayashi, E., Dohi, T., & Sakuma, I. (2002, September). A new, compact MR-compatible surgical manipulator for minimally invasive liver surgery. In *International Conference on Medical Image Computing and Computer-Assisted Intervention* (pp. 99-106). Springer, Berlin, Heidelberg.
  - [30] Moser, R., Gassert, R., Burdet, E., Sacher, L., Woodtli, H. R., Erni, J., ... & An, M. R. (2003). Compatible Robot Technology. In *Proceedings of the 2003 IEEE, International Conference on Robotics and Automation*.

- [31] Yamamoto, A., Ichiyanagi, K., Higuchi, T., Imamizu, H., Gassert, R., Ingold, M., ... & Bleuler, H. (2005, April). Evaluation of MR-compatibility of electrostatic linear motor. In *Proceedings of the 2005 IEEE International Conference on Robotics and Automation* (pp. 3658-3663). IEEE.
- [32] Wang, W., Shi, Y., Yuan, X., Goldenberg, A., & Shokrollahi, P. (2013, December). Compatibility of US motors for development of MRI-guided surgical robot. In *2013 6th International Conference on Biomedical Engineering and Informatics* (pp. 388-392). IEEE.
- [33] Koseki, Y., Kikinis, R., Jolesz, F. A., & Chinzei, K. (2004, September). Precise evaluation of positioning repeatability of MR-compatible manipulator inside MRI. In *International Conference on Medical Image Computing and Computer-Assisted Intervention* (pp. 192-199). Springer, Berlin, Heidelberg.
- [34] Takahashi, N., Tada, M., Ueda, J., Matsumoto, Y., & Ogasawara, T. (2003, October). An optical 6-axis force sensor for brain function analysis using fMRI. In *SENSORS, 2003 IEEE* (Vol. 1, pp. 253-258). IEEE.
- [35] Gassert, R., Moser, R., Burdet, E., & Bleuler, H. (2006). MRI/fMRI-compatible robotic system with force feedback for interaction with human motion. *IEEE/ASME transactions on mechatronics*, 11(2), 216-224.
- [36] Sutherland, G. R., McBeth, P. B., & Louw, D. F. (2003, June). NeuroArm: an MR compatible robot for microsurgery. In *International congress series* (Vol. 1256, pp. 504-508). Elsevier.
- [37] Comber, D. B., Slightam, J. E., Gervasi, V. R., Neimat, J. S., & Barth, E. J. (2016). Design, additive manufacture, and control of a pneumatic MR-compatible needle driver. *IEEE Transactions on Robotics*, 32(1), 138-149.
- [38] Li, G., Su, H., Cole, G. A., Shang, W., Harrington, K., Camilo, A., ... & Fischer, G. S. (2014). Robotic system for MRI-guided stereotactic neurosurgery. *IEEE transactions on biomedical engineering*, 62(4), 1077-1088.
- [39] Guo, Z., Dong, Z., Lee, K. H., Cheung, C. L., Fu, H. C., Ho, J. D., ... & Kwok, K. W. (2018). Compact design of a hydraulic driving robot for intraoperative MRI-guided

- bilateral stereotactic neurosurgery. *IEEE Robotics and Automation Letters*, 3(3), 2515-2522.
- [40] Masamune, K., Kobayashi, E., Masutani, Y., Suzuki, M., Dohi, T., Iseki, H., & Takakura, K. (1995). Development of an MRI-compatible needle insertion manipulator for stereotactic neurosurgery. *Journal of Image Guided Surgery*, 1(4), 242-248.
- [41] Hong, Z., Yun, C., Zhao, L., & Wang, Y. (2008, May). Design and optimization analysis of open-MRI compatible robot for neurosurgery. In *2008 2nd International Conference on Bioinformatics and Biomedical Engineering* (pp. 1773-1776). IEEE.
- [42] Govers, C. P. (1996). What and how about quality function deployment (QFD). *International journal of production economics*, 46, 575-585.
- [43] Chan, L. K., & Wu, M. L. (2002). Quality function deployment: A literature review. *European journal of operational research*, 143(3), 463-497.
- [44] Lai, X., Xie, M., & Tan, T. C. (2004, October). Optimizing product design using the Kano model and QFD. In *2004 IEEE International Engineering Management Conference (IEEE Cat. No. 04CH37574)* (Vol. 3, pp. 1085-1089). IEEE.
- [45] Dimsey, J., & Mazur, G. (2002, December). QFD to Direct Value Engineering in the Design of a Brake System. In *The 14th Symposium on QFD*.
- [46] Bevilacqua, M., Ciarapica, F. E., & Giacchetta, G. (2006). A fuzzy-QFD approach to supplier selection. *Journal of Purchasing and Supply Management*, 12(1), 14-27.
- [47] Bhattacharya, A., Geraghty, J., & Young, P. (2010). Supplier selection paradigm: An integrated hierarchical QFD methodology under multiple-criteria environment. *Applied Soft Computing*, 10(4), 1013-1027.
- [48] Al-Bashir, A., Al-Rawashdeh, M., Al-Hadithi, R., Al-Ghandoor, A., & Barghash, M. (2012). Building medical devices maintenance system through quality function deployment. *JJMIE*, 6(1).
- [49] SHI, Y. W., & HAN, S. (2017). Modeling design research of medical service robot based on QFD and Kano model. *Journal of Machine Design*, (12), 22.
- [50] Huang, Y. Y., & Low, K. H. (2010, August). Comprehensive planning of robotic therapy and assessment of task-oriented functions via improved QFD applicable to hand

- rehabilitation. In *2010 IEEE International Conference on Automation Science and Engineering* (pp. 252-257). IEEE.
- [51] Luna-Avilés, A., Hernández-Gómez, L. H., Beltrán-Fernández, J. A., Urriolagoitia-Calderón, G., Gómez-Michel, D., Martínez-Espinoza, D. M., ... & Urriolagoitia-Sosa, G. (2013). Using quality function deployment methodology to translate qualitative to quantitative requirements in the design a of a knee re-trainer. In *Characterization and Development of Biosystems and Biomaterials* (pp. 99-107). Springer, Berlin, Heidelberg.
- [52] Han, X., & Yang, Y. (2014, June). Customer requirements for a vitreoretinal robot. In *2014 International Conference on Management Science and Management Innovation (MSMI 2014)*. Atlantis Press.
- [53] Mocan, B., Bintintan, V. V., Brad, S., Ciuce, C., Mocan, M., & Murar, M. (2016). Development of a Robotic Driven Handheld Laparoscopic Instrument for Non-invasive Intraoperative Detection of Small Endoluminal Digestive Tumors. In *New Trends in Medical and Service Robots* (pp. 197-210). Springer, Cham.
- [54] Aibin, Z., Shengli, H., Ziyue, L., & Yangyang, L. (2016, August). Lower limb rehabilitation robot design with dual customized design: Customized gait and customized exoskeleton. In *2016 13th International Conference on Ubiquitous Robots and Ambient Intelligence (URAI)* (pp. 572-575). IEEE.
- [55] Wang, D., Yu, H., Wu, J., Meng, Q., & Lin, Q. (2019). Integrating fuzzy based QFD and AHP for the design and implementation of a hand training device. *Journal of Intelligent & Fuzzy Systems*, 36(4), 3317-3331.
- [56] Motwani, J. G., Sower, V. E., Kumar, A., Antony, J., & Dhakar, T. S. (2006). Integrating quality function deployment and benchmarking to achieve greater profitability. *Benchmarking: An International Journal*.
- [57] Shen, X. X., Tan, K. C., & Xie, M. (2000). Benchmarking in QFD for quality improvement. *Benchmarking: An International Journal*.
- [58] Motwani, J. G., Sower, V. E., Kumar, A., Antony, J., & Dhakar, T. S. (2006). Integrating quality function deployment and benchmarking to achieve greater profitability. *Benchmarking: An International Journal*.

- [59] Khalsa, S. S. S., & Park, P. (2020). Commentary: Cirq® Robotic Assistance for Minimally Invasive C1-C2 Posterior Instrumentation: Report on Feasibility and Safety. *Operative Neurosurgery*, 19(6), E592-E593.
- [60] Maddahi, Y., Zareinia, K., Gan, L. S., Lama, S., Sutherland, G. R., & Sepehri, N. (2015, May). Positional and force characteristics of neuroarm robotic manipulators: a pilot study. In *Proceedings of the international conference of control, dynamic systems and robotics*.
- [61] Sutherland, G. R., McBeth, P. B., & Louw, D. F. (2003, June). NeuroArm: an MR compatible robot for microsurgery. In *International congress series* (Vol. 1256, pp. 504-508). Elsevier.
- [62] Maddahi, Y., Zareinia, K., Gan, L. S., Lama, S., Sutherland, G. R., & Sepehri, N. (2015, May). Positional and force characteristics of neuroarm robotic manipulators: a pilot study. In *Proceedings of the international conference of control, dynamic systems and robotics*.
- [63] Sutherland, G. R., Louw, D. F., McBeth, P. B., Fielding, T., & Gregoris, D. J. (2011). *U.S. Patent No. 8,005,571*. Washington, DC: U.S. Patent and Trademark Office.
- [64] Lefranc, M., & Peltier, J. (2016). Evaluation of the ROSA™ Spine robot for minimally invasive surgical procedures. *Expert review of medical devices*, 13(10), 899-906.
- [65] Brandmeir, N. J., Savaliya, S., Rohatgi, P., & Sather, M. (2018). The comparative accuracy of the ROSA stereotactic robot across a wide range of clinical applications and registration techniques. *Journal of robotic surgery*, 12(1), 157-163.
- [66] Cleary, K., & Brooks, T. (1993, May). Kinematic analysis of a novel 6-DOF parallel manipulator. In *[1993] Proceedings IEEE International Conference on Robotics and Automation* (pp. 708-713). IEEE.
- [67] Galldiks, N., Law, I., Pope, W. B., Arbizu, J., & Langen, K. J. (2017). The use of amino acid PET and conventional MRI for monitoring of brain tumor therapy. *NeuroImage: Clinical*, 13, 386-394.
- [68] Chan, K. G., Fielding, T., & Anvari, M. (2016). An image-guided automated robot for MRI breast biopsy. *The International Journal of Medical Robotics and Computer Assisted Surgery*, 12(3), 461-477.
- [69] Vilsmeier, S. (2005). *U.S. Patent No. 6,859,660*. Washington, DC: U.S. Patent and

Trademark Office.

- [70] Zhang, Y., Lu, M., & Du, H. (2017, October). Kinematics analysis and trajectory planning for a breast intervention robot under MRI environment. In *2017 IEEE International Conference on Cyborg and Bionic Systems (CBS)* (pp. 237-242). IEEE.
- [71] Rastegar, J., & Fardanesh, B. (1990). Manipulation workspace analysis using the Monte Carlo method. *Mechanism and Machine Theory*, 25(2), 233-239.
- [72] ASTM International. (2015). ASTM F2052-15: Standard Test Method for Measurement of Magnetically Induced Displacement Force on Medical Devices in the Magnetic Resonance Environment. *West Conshohocken, Pa: ASTM International*.
- [73] Nyenhuis, J. A., Park, S. M., Kamondetdacha, R., Amjad, A., Shellock, F. G., & Rezai, A. R. (2005). MRI and implanted medical devices: basic interactions with an emphasis on heating. *IEEE Transactions on device and materials reliability*, 5(3), 467-480.
- [74] American Society for Testing and Materials International. (2006). Designation: ASTM F2052-06e1, standard test method for measurement of magnetically induced displacement force on medical devices in the magnetic resonance environment.